

Doctoral Thesis

Shibaura Institute of Technology

**Simple and Reliable Fabrication Process of Dielectric
Elastomer Sensors and Actuators for Soft Robotics**

2022/September

Ardi Wiranata

Simple and Reliable Fabrication Process of Dielectric Elastomer Sensors and Actuators for Soft Robotics

Major : Graduate School of Engineering and Science
(Doctor's Program) Functional Control
System

Student Number : NB19501

Name : Ardi Wiranata

Supervisor : Professor Naoki Hosoya

Co-Supervisor : Professor Shingo Maeda,
Professor Shinji Hashimura,
Professor Yasuyuki Ishii,
Professor Sumito Nagasawa,
Professor Itsuro Kajiwara

Contents

List of Figures	iii
List of Tables	xi
Abstract	1
Chapter 1 Introduction	3
1.1 Stretchable electrodes in dielectric elastomer actuators and sensors	3
1.2 Problem formulation	6
1.3 Objectives of this research	6
Chapter 2 Review of Stretchable Electrode Fabrication Processes	9
2.1 Pad-printing method for stretchable electrodes in DEAs	9
2.2 Stretchable electrode fabrication based LS methods	12
2.3 Stretchable electrode fabrication based on SCBI	13
2.4 Composite elastomer for stretchable electrodes	14
2.5 Fabrications of CNT-based stretchable electrodes using manual brushing methods	15
2.6 Fabrications of CNT-based stretchable electrodes using an automatic brushing machine	17
2.7 Conclusion	18
Chapter 3 Simple Manual Brushing Methods to Fabricate PDMS Powdered-based DEAs	19
3.1 Introduction	19
3.2 Investigation of elastomer mechanical characteristics	21
3.3 Surface tackiness characteristics of PDMS membranes	24
3.4 Electromechanical properties of CNT powder-based stretchable electrodes	26
3.5 Surface conditions of brushed multiwalled CNTs on elastomer membranes	29
3.6 Fabrication methods of DEAs	33
3.7 Static characteristics of DEAs	33
3.8 Dynamic characteristics of DEAs	35

3.9 Conclusion	37
Chapter 4 Automatic Brushing Method for Stretchable Electrodes and Integration of Powdered-based Stretchable Sensors for Wearable Devices	38
4.1 Introduction	38
4.2 Mechanical characteristics of the elastomers	41
4.3 Stretchable sensor surface conditions	45
4.4 Electromechanical characteristics of stretchable electrodes	48
4.4.1 Electromechanical tensile test equipment for stretchable conductive materials	48
4.4.2 Electromechanical tensile test results and discussion	62
4.5 Stretchable sensor lamination process	70
4.6 Stretchable sensor for wearable devices	73
4.7 Conclusion	77
Chapter 5 Potential fabrication of Ultra-Low-Voltage DEAs	79
5.1 Introduction	79
5.2 Nanosheet fabrication method	81
5.3 Ultra-low voltage DEAs fabrication	82
5.4 Actuation demonstration of ultra-low-voltage DEAs at high- frequency operations	83
5.5 Conclusion	87
Chapter 6 Summary	88
Acknowledgement	90
Reference	92
List of Publications	100

List of Figures

Figure 1.1. Dielectric Elastomer Actuator (DEA) structure in the (a) non-activated state and (b) activated state.	3
Figure 2.1. Mechanism of the pad printing method. (a) Ink updating process, (b) ink lamination on the pattern updater, (c) updating pattern on the silicone pad, and (d) pad printing process on the specimen.	11
Figure 2.2. Basic concept of the Langmuir–Schaefer (LS) technique.	12
Figure 2.3. Supersonic cluster beam implantation (SCBI) technique.	14
Figure 2.4. Brushing method for a stretchable electrode and fabrication method for a single-layer DEA. ^[21] (Adapted from ref. ^[21] with free distribution permission under the CC-BY License.)	16
Figure 2.5. Wooden brush with synthetic nylon hair. ^[20] (Adapted from ref. ^[20] with free distribution permission under the CC-BY License.)	17
Figure 2.6. Equipment setup and brushing process using a brushing machine. (See Movie S1 to view the complete process). (Adapted from ref. ^[20] with free distribution permission under the CC-BY License.)	18
Figure 3.1. Engineering stress–strain curves of the PDMS samples made with various ratios of the base polymer and the curing agent. (Adapted from ref. ^[21] with free distribution permission under the CC-BY License.)	22
Figure 3.2. Cyclic tensile test results from three different specimens. (a) PDMS 10-1, (b) 20-1, and (c) 30-1. (Adapted from ref. ^[21] with free distribution permission under the CC-BY License.)	23
Figure 3.3. Tackiness evaluation of PDMS membranes. (Adapted from ref. ^[21] with free distribution permission under the CC-BY License.)	25

Figure 3.4. Maximum tackiness of the PDMS membranes. (Adapted from ref. ^[21] with free distribution permission under the CC-BY License.)	26
Figure 3.5. Electromechanical measurement of a stretchable electrode. (Adapted from ref. ^[21] with free distribution permission under the CC-BY License.)	27
Figure 3.6. Change in the resistance value during tensile tests of the stretchable electrodes. (Adapted from ref. ^[21] with free distribution permission under the CC-BY License.)	27
Figure 3.7. Demonstration of a stretchable electrode when subjected to an electric current under uniaxial strain. (Adapted from ref. ^[21] with free distribution permission under the CC-BY License.)	28
Figure 3.8. Surface morphology of brush painted MWCNT on the elastomer membrane. Brushed MWCNT on PDMS with a mixing ratio of (a) 10-1, (b) 20-1, and (c) 30-1. (d and g) SEM images of the brushed MWCNT on PDMS 10-1. (e and h) SEM images of the brushed MWCNT on PDMS 20-1. (f and i) SEM images of the brushed MWCNT on PDMS 30-1. (Adapted from ref. ^[21] with free distribution permission under the CC-BY License.)	30
Figure 3.9. SEM images from brushed MWCNT on the PDMS membrane after 20-cyclic tensile tests for (a and d) PDMS 10-1, (b and e) PDMS 20-1, and (c and f) PDMS 30-1. (Adapted from ref. ^[21] with free distribution permission under the CC-BY License.)	31
Figure 3.10. Complete fabrication process of single layer DEAs. (Adapted from ref. ^[21] with free distribution permission under the CC-BY License.)	32

- Figure 3.11.** Area strain as a function of the electric field at various PDMS mixing ratio with the prestretching of (a) 10%, (b) 20%, and (c) 30%. (d) Photos of the actuators constructed from PDMS 30-1 and 30% prestretching. (Adapted from ref. ^[21] with free distribution permission under the CC-BY License.) 34
- Figure 3.12.** Dynamic performance of powdered-based DEAs. (a) PDMS 10-1 with 30% prestretching, (b) PDMS 20-1 with 30% prestretching, and (c) PDMS 30-1 with 30% prestretching. (d) Summary of the peak actuation of PDMS 10-1, PDMS 20-1, and PDMS 30-1 with 30% prestretching. (Adapted from ref. ^[21] with free distribution permission under the CC-BY License.) 36
- Figure 4.1.** DIY-fabrication concept of a stretchable strain sensor and a wearable device prototype. (a) Brushing the CNT powder using a brushing machine, (b) manually shaping the stretchable sensor, and (c) laminating the stretchable strain sensor using a thin Ecoflex membrane. (d) Plug-and-play concept for ease of sensor mounting and maintenance, (e) sensor embedment on a cotton glove and integration system using an economical microcontroller (Arduino), and (f) demonstration of the strain sensor to detect human hand movement. (Adapted from ref. ^[20] with free distribution permission under the CC-BY License.) 41
- Figure 4.2.** Mechanical characteristics (engineering stress-strain) of the elastomer. (Adapted from ref. ^[20] with free distribution permission under the CC-BY License.) 42
- Figure 4.3.** Molding shape for the loop tack test of the elastomer. (Adapted from ref. ^[20] with free distribution permission under the CC-BY License.) 44

Figure 4.4. Tackiness of the elastomer surface. (Adapted from ref. [20] with free distribution permission under the CC-BY License.)	45
Figure 4.5. Shaping process of the stretchable strain sensor. (Adapted from ref. [20] with free distribution permission under the CC-BY License.)	46
Figure 4.6. FE-SEM images show the surface morphology of (a–a2) PDMS-PEIE/MWCNT-1, (b–b2) PDMS-PEIE/MWCNT-2, and (c–c2) PDMS-PEIE/MWCNT-3 at different magnifications (micrometer to nanometer size). (Adapted from ref. [20] with free distribution permission under the CC-BY License.)	47
Figure 4.7. Electromechanical tensile test equipment. (a) Controller and data acquisition part, and (b) testing part. (Adapted from ref. [117] with free distribution permission under the CC-BY License.)	52
Figure 4.8. Material gripper for the electromechanical tensile test equipment. (Adapted from ref. [117] with free distribution permission under the CC-BY License.)	53
Figure 4.9. GUI of the tensile test equipment. (Adapted from ref. [117] with free distribution permission under the CC-BY License.)	53
Figure 4.10. Home screen of the electromechanical device GUI control. (Adapted from ref. [117] with free distribution permission under the CC-BY License.)	60
Figure 4.11. Variable setup for testing equipment. (a) LCR meter tab, (b) loadcell tab, and (c) linear stage control tab. (Adapted from ref. [117] with free distribution permission under the CC-BY License.)	61

Figure 4.12. Run configuration option. (Adapted from ref. ^[117] with free distribution permission under the CC-BY License.)	61
Figure 4.13. Capacitance-type sensor mechanism for the (a) initial condition and (b) deformed condition.	63
Figure 4.14. Resistance-type sensor mechanism for the (a) initial and (b) elongated conditions.	64
Figure 4.15. Electromechanical characteristics of the stretchable strain sensors: (a) PDMS-PEIE/MWCNT-1, (b) PDMS-PEIE/MWCNT-2 and (c) PDMS-PEIE/MWCNT-3. Gauge factors (GFs) of (d) PDMS-PEIE/MWCNT-1, (e) PDMS-PEIE/MWCNT-2, and (f) PDMS-PEIE/MWCNT-3. (Adapted from ref. ^[20] with free distribution permission under the CC-BY License.)	65
Figure 4.16. PDMS-PEIE-2/MWCNT-2 stretchable sensor characteristics at a tensile speed of 7 mm/s. (Adapted from ref. ^[20] with free distribution permission under the CC-BY License.)	66
Figure 4.17. Sensor characteristics at a higher strain for (a) PDMS-PEIE-2/MWCNT-1, (b) PDMS-PEIE-2/MWCNT-2, and (c) PDMS-PEIE-2/MWCNT-3). (Adapted from ref. ^[20] with free distribution permission under the CC-BY License.)	66
Figure 4.18. PDMS-PEIE/MWCNT-1 tested for 1000 cycle in each test and a tensile speed of (a) 7mm/s, (b) 21 mm/s, and (c) tensile speed of 30mm/s. (Adapted from ref. ^[20] with free distribution permission under the CC-BY License.)	68

Figure 4.19. Sensor assessment for the vibration detection experimental setup. (Adapted from ref. [20] with free distribution permission under the CC-BY License.)	69
Figure 4.20. Response of a PDMS-PEIE/MWCNT-1 stretchable sensor to a vibration at 40 Hz. (Adapted from ref. [20] with free distribution permission under the CC-BY License.)	69
Figure 4.21. Sensor lamination process using a thin Ecoflex membrane. (Adapted from ref. [20] with free distribution permission under the CC-BY License.)	71
Figure 4.22. Final sensor structure after the lamination process. (Adapted from ref. [20] with free distribution permission under the CC-BY License.)	71
Figure 4.23. Stretchable strain sensor (PDMS-PEIE/MWCNT-1) characteristics after the lamination process using an Ecoflex membrane at a tensile test speed of (a) 7 mm/s, (b) 21 mm/s, and (c) 30 mm/s. (Adapted from ref. [20] with free distribution permission under the CC-BY License.)	72
Figure 4.24. Plug-and-play concept of the stretchable strain sensor. (Adapted from ref. [20] with free distribution permission under the CC-BY License.)	73
Figure 4.25. Response patterns of the PDMS-PEIE/MWCNT-1 sensor fixed on the (a) index finger, (b) wrist, (c) 45-degree movement of the elbow, and (d) 90-degree movement of the elbow. (Adapted from ref. [20] with free distribution permission under the CC-BY License.)	74
Figure 4.26. Wearable device arrangement to simulate and mimic human hand movements. (Adapted from ref. [20] with	

free distribution permission under the CC-BY License.)	74
Figure 4.27. Detailed electric circuit for the stretchable strain sensor reader and signal processor. (Adapted from ref. ^[20] with free distribution permission under the CC-BY License.)	76
Figure 4.28. (b and d) Control simulation of a virtual hand using (a and c) a stretchable strain sensor attached to a cotton hand glove. (Adapted from ref. ^[20] with free distribution permission under the CC-BY License.)	76
Figure 5.1. Roll-to-roll (R2R) process for fabricating nanosheets. (a) Schematic of the R2R process, (b) multilayered structure, and (c) actual image of the final product. (Adapted from ref. ^[138] with free distribution permission under the CC-BY License.)	82
Figure 5.2. Nanosheet DEA fabrication process. (a) Detachment process of the nanosheet membrane from the supporting material. (b and d) PVA removal process from the nanosheet membrane. (c) Frame application to the nanosheet PDMS membrane. (e) Application of the conductive nanosheet on the PDMS nanosheet surface. It should be noted that this process is repeated twice to attach the electrodes on both sides of nanosheet PDMS. (f) Low-voltage DEAs. (Adapted from ref. ^[138] with free distribution permission under the CC-BY License).	84
Figure 5.3. Actuation velocity measurements of DEAs in the (a) undeformed and (b) deformed (actuated) states. (Adapted from ref. ^[138] with free distribution permission under the CC-BY License.)	85

Figure 5.4. Velocity responses on the nanosheet DEA surface at a voltage of 50 V and (a) 5 kHz, (b)10 kHz, and (c) 30 kHz. (Adapted from ref. ^[138] with free distribution permission under the CC-BY License.)

86

Figure 5.5. Displacement in the thickness direction (z-axis direction) of nanosheet DEAs at a voltage of 50 V and (a) 5 kHz, (b)10 kHz, and (c) 30 kHz. (Adapted from ref. ^[138] with free distribution permission under the CC-BY License.)

87

List of Table

Table 4.1. Design file name and summary. (Adapted from ref. ^[117] with free distribution permission under the CC-BY License.)	55
Table 4.2. Cost of the materials. (Adapted from ref. ^[117] with free distribution permission under the CC-BY License.)	56
Table 4.3. Connection chart of the loadcell module. (Adapted from ref. ^[117] with free distribution permission under the CC-BY License.)	58

Abstract

Soft robots have received much attention from researchers due to their flexibility. A critical point in their development is the advanced technologies of soft actuators and sensors. There are many examples of soft actuators, including soft pneumatic actuators, gel actuators, stretchable pumps, and dielectric elastomer actuators (DEAs). Of these, DEAs are promising technology for soft actuators because they have a high energy density and fast response.

DEAs consist of a thin elastomer membrane sandwiched between two stretchable electrodes. The electrostatic force upon applying a voltage to the stretchable electrodes squeezes the elastomer membrane in the thickness direction, causing the DEA to expand in the planar directions. To optimize the actuation performance of DEAs, the stretchable electrode must preserve the electrical conductivity while sustaining large deformations and a high durability over thousands of cycles without adding additional stiffness to elastomer membranes. Recently, researchers have reported novel technologies to fabricate stretchable electrodes such as electrode pad printing, Langmuir-Schaefer (LS), and supersonic cluster beam implantation (SCBI). These fabrication methods require complex steps and special equipment to produce stretchable electrodes. Currently, rapid, easy, reliable, and cost-effective methods to fabricate stretchable electrodes remain challenging.

This work presents a simple and reliable fabrication process of stretchable electrodes for dielectric elastomer (DE) sensors and actuators with applications in soft robotics and wearable devices. The initial fabrication process of powdered-based DEAs involved a manual brushing method. Then the compatibility of the brushing method with the elastomer was improved by optimizing the elastomer quality. The next research stage was to automate the brushing process. The aim of this automation was to remove the human influence in the brushing process. The last step was to apply stretchable electrodes in both DEAs and wearable devices.

To assess the quality of the electromechanical properties of the stretchable electrodes, a customized electromechanical tensile test device was developed. The

final test device integrated three standalone devices. Python software was used to integrate the three devices and provide a graphic user interface (GUI) for easy operation. This customized electromechanical tensile test should facilitate advances in soft robotics, especially soft and stretchable sensors. Furthermore, this electromechanical setup should contribute to the development of laboratory facilities and the educational field, especially the understanding of the electromechanical properties of stretchable conductive materials.

Additionally, reducing the driving voltage of DEAs provides an opportunity to use DEAs as wearable devices. A suitable strategy to achieve low voltage DEAs is to reduce the elastomeric membrane thickness to the nanometer range. This additional research aims to reduce the driving voltage by fabricating a nanometer-sized elastomer. This was achieved by integrating the previously reported roll-to-roll method to fabricate stretchable electrodes and the elastomer membrane. This research should contribute to the development of soft robotics, especially stretchable sensors and actuators (DEAs and DEs).

Chapter 1

Introduction

1.1 Stretchable electrodes in dielectric elastomer actuators and sensors

Stretchable electrodes are a breakthrough technology, which has advanced soft robotics. Stretchable electrodes can improve the flexibility of a system since they can preserve their electrical conductivity while sustaining large deformations and a high durability for millions of cycles. One example of a soft actuator that depends on the quality of the stretchable electrodes are Dielectric Elastomer Actuators (DEAs).

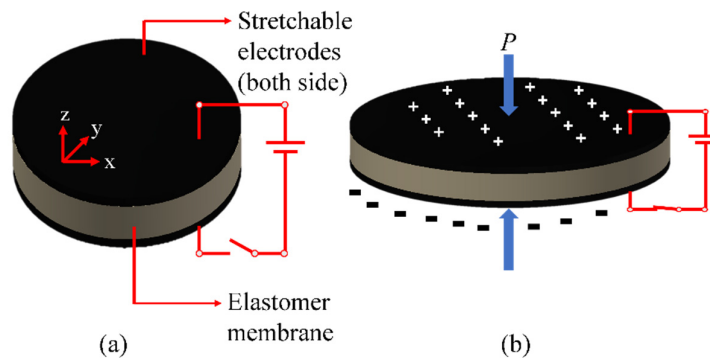


Figure 1.1. Dielectric Elastomer Actuator (DEA) structure in the (a) non-activated state and (b) activated state.

DEAs require electrical energy to produce a mechanical energy. DEAs consist of a soft elastomeric membrane sandwiched between two stretchable electrodes (**Figure 1.1**). When a direct current (DC) electric field is applied to both compliant electrodes, opposite charges accumulate at the electrodes, squeezing the elastomer membrane. Since the elastomer membrane is incompressible, the compression in the z-direction may cause the elastomer to expand in the x-y direction.^[1] The electromechanical response of DEAs depends on the applied external electric field and the electrical properties of the elastomer. These two variables are summarized

by the Maxwell pressure (P) in **Equation 1.1**, where ε_0 is the vacuum permittivity, which is 8.85×10^{-12} F/m, ε_r is the relative dielectric constant, V is the voltage, and z is the membrane thickness of the elastomer.

$$P = \varepsilon_0 \varepsilon_r \left(\frac{V}{z} \right)^2 \quad (1.1)$$

For an actuation strain below 20%, **Equation 1.2** describes the deformation of the dielectric membrane in the z -direction, where S_z is the actuation in the z -direction and Y is the elastic modulus.^[1]

$$S_z = \varepsilon_0 \varepsilon_r \frac{V^2}{Y z^2} \quad (1.2)$$

Beside DEAs, a stretchable electrode is also useful for stretchable strain sensors. The change in the electrical resistance (R) of the flexible strain sensor is affected by the strain (e_l) of the elastomer. The relative change of R to e_l is denoted as the gauge factor (GF), which is also known as the sensitivity of the sensor. When a sensor undergoes a uniaxial tensile test, it should exhibit a geometrical change, which is described in **Equation 1.3**.^[2]

$$l = e_l l_0 + l_0, \quad w = \frac{w_0}{\sqrt{e_l + 1}}, \quad t = \frac{t_0}{\sqrt{e_l + 1}} \quad (1.3)$$

where l is the electrode length, w is the electrode width, t is the electrode thickness, and e_l is the strain in the loading direction. l_0 , w_0 , and t_0 are the initial length, width, and thickness of the electrodes, respectively. Assuming that the cross section of the flexible sensor is uniform, the resistance change can be described by (**Equation 1.4**).^[2]

$$R = \rho \frac{l_0}{w_0 t_0} (e_l + 1)^2 = \frac{\rho}{\rho_0} R_0 (e_l + 1)^2 \quad (1.4)$$

where ρ_0 is the reference resistivity, ρ is the resistivity of the stretchable electrodes, and R_0 is the reference resistance. Finally, the sensitivity of the sensor (GF) can be defined by **Equation 1.5**.^[2]

$$GF = \frac{\Delta R}{R_0 e_1} = \frac{1}{e_1} \left(\frac{\rho}{\rho_0} (e_1 + 1)^2 - 1 \right) \quad (1.5)$$

Many researchers have raced to produce high-quality stretchable electrodes for DEAs and sensors. Both the material selection and the fabrication method are crucial to improve the quality of stretchable electrodes in terms of stretchability and reliability. Many different types of stretchable electrodes have been reported, including carbon-based electrodes,^[3] metal thin-film electrodes,^[3] composite silicone-carbon electrodes,^[2] and ionic gels.^[4] Each electrode has distinctive characteristics when used as a stretchable sensor (dielectric elastomer Sensor DES) and actuator (DEA) mechanism.

Many researchers have also reported different fabrication options for stretchable electrodes such as a lamination technique for stretchable electrodes, mixing and creating electrodes-polymer composites, and direct electrode patterning on the elastomer. Examples of lamination techniques include pad printing,^[5] Langmuir-Schaefer (LS),^[6] and supersonic cluster beam implantation (SCBI).^[7] Among these, pad printing is the simplest to create stretchable electrodes because the user can stamp the electrodes easily using a commercial pad-printing machine. The weakness of pad printing is that it requires a conductive liquid. A long process and treatment are needed to produce a high quality conductive liquid (e.g., mixing of carbon black and an elastomer to form a carbon black-elastomer composite^[5]). Additionally, pad printing requires an expensive and bulky machine.^[5] SCBI^[7] is a highly reliable method. However, it requires a high-pressure chamber, which also needs attention to reproduce the whole system. Furthermore, the inert gas used in SCBI may incur additional cost to fabricate stretchable electrodes. LS is also a simple method.^[6] The electrode fabrication process involves directly transferring an electrode from a water surface to the target surface (e.g., PDMS surface). Since this process involves liquid and solid interactions, a good combination of conductive materials is necessary before transferring to the target surface (e.g., a composite between hydrophobic

poly(alkylthiophene) and hydrophilic multiwalled CNTs (MWCNT)^[6]). A special clean room is needed for the fabrication process to avoid contamination.

Another popular fabrication method is to directly mix the electrodes to realize electrode-polymer composites.^{[2][8]–[11]} The mixing process typically requires a lot of time to create a high-quality stretchable sensor. Recently, three-dimensional (3D) printing has been used to pattern electrodes.^[12] The key challenges in 3D-printing of electrodes are the fabrication of a highly conductive substrate and the printer settings. Substrate preparations and the printer settings may also require special skills.

1.2 Problem formulation

As demonstrated in the previous section, simple, reliable, and economical fabrication methods for DEAs and sensors have yet to be established. In this current research perspective, simple fabrication should consist of fully customized methods that can be processed by an uncertified person. Such simple fabrication methods are closely related to the Do-it-Yourself (DIY) method, which allows users to fully customize their research according to their requirements. To ensure the quality of the stretchable electrodes for DEAs and sensors, fabrication methods should also be reliable in terms of reproducibility and result quality.

1.3 Objectives of this research

This research aims to establish a simple, fast, and reliable fabrication process for DEAs. It can be divided into six phases. The first phase was to develop a manual brushing method to realize powdered-based DEAs. The dielectric membrane in this research was a polydimethylsiloxane (PDMS)-based elastomer (Sylgard 184). To understand the characteristics of the DEAs produced using PDMS and a brushing method, the first was to examine the influence of the mixing ratio of the elastomer base and its curing agent on the mechanical characteristics of Sylgard 184 using a single-pull-to-failure tension test.

The second phase identified a simplified and reliable approach to fabricate DEAs using brushing methods to pattern carbon nanotube (CNT) powder on the elastomer

membrane. This included evaluating the electrical properties of the brushed CNT powder on various samples of PDMS to understand the quality of the stretchable electrodes. Then static and dynamic characteristic tests were conducted to examine the basic performance of DEAs fabricated using brushed CNTs. The relationships between the elastomer stress-softening, stickiness surface characteristic of the elastomers, and the DEA performance (in terms of actuation) were also investigated.

The third phase removed the human influence in the brushing process, improved the consistency of the brushing, and enhanced the brushing process. An automatic brushing machine is a convenient technology to automate the brushing process. This machine also has potential for future mass production.

The fourth phase boosted the elastomer compatibility towards the fabrication of stretchable electrodes using an automatic brushing method. The elastomer compatibility and quality were optimized by adding polyethyleneimine (PEIE) in the previously reported pre-polymer of PDMS 30-1. Adding a small amount of PEIE (approximately 0.11 wt%) increased the stickiness of the elastomer and enhanced the compatibility for the brushing process of the CNT powder.

The fifth phase fabricated a wearable device using this simple brushing method. Since the stretchable electrodes are powdered-based, the device requires a lamination process to prevent the powder from staining any other device. The lamination process was conducted using a thin Ecoflex membrane. The Ecoflex membrane can be used to cover the stretchable electrodes since both the Ecoflex membrane and stretchable electrodes display high stretchability mechanical characteristics. A high stretchability can ease material handling of micrometer layers of the Ecoflex membrane because the membrane does not rip easily during the lamination process. As a proof-of-concept, a prototype of a powder-based stretchable electrode was demonstrated as a wearable device. This wearable device prototype integrated a sensor with a low-cost microcontroller (Arduino) to detect hand movements.

The sixth phase focused on advancing DEA technology. Specifically, research was conducted to increase the safety and reduce the electric circuit cost of DEAs. A strategy was devised to reduce the voltage operations of DEAs below the kV range. The simplest strategy to reduce the voltage operation was to decrease the dielectric

elastomer membrane thickness. This additional research also demonstrated DEAs with a nanometer uniform thickness capable of operating at a low voltage (below 70 V) and a high frequency. The roll-to-roll (R2R) process was used to fabricate a 600-nm-thick stretchable PDMS nanosheet and a 200-nm-thick conductive nanosheet. These nanosheet-DEAs were subsequently tested in high-frequency operations of DC voltage below 70 V and in a frequency range of 1–30 kHz.

Chapter 2

Review of Stretchable Electrode Fabrication Processes

2.1 Pad-printing method for stretchable electrodes in DEAs

The possibility of printing and ink patterning on an unprintable surface (e.g., 3D surfaces) has received much attention from engineers, designers, and researchers. Normal inkjet printing limits the printing to flat surfaces. To pattern ink on a 3D model requires pad printing technology. Pad printing is a process that enables the transfer of a 2D pattern onto a 3D surface of an object. Pad printing was first established in the late eighteenth century.^[13] The first pad printing project was decorative porcelain.^[13] The designer used pad printing to transfer blue ink onto the surface of the porcelain. In the 18th century, the pad used was a soft tampon filled with a gelatin material. This soft tampon enabled the pad to adapt easily to a printing form. Since the pad was a soft tampon, pad printing was also called tampography. This is one of the oldest printing techniques.^[13] The first printing forms were engraved manually by a sculptor. Because the first printing form was made from copper, the engraving process was time consuming. Since then, this process has drastically changed. Modern printing forms can be fabricated using many methods, including 3D printing, laser engraving, and computer numerical control (CNC) milling. Printing ink used in pad printing has also evolved. Modern ink used in pad printing is solvent-based ink. The first true industrial application of pad printing was reported in the 1960s in the Swiss watch-making industry.^[13] Since then, the development of pad printing technology has expanded, and pad printing applications have become widespread. Many engineers have contributed to pad printing technologies. Breakthrough pad printing technologies include the introduction of silicone pads and the use of efficient machinery.

Figure 2.1 shows the basic principle of pad printing methods. Pad printing methods have several critical components: pattern plate (printing form), pad (silicon pad), printing ink, and printing machines. Commercial printing forms have different

names such as cliché and printing plate or pattern plate.^[13] The printing form is basically the carrier of a design pattern that can be transferred to any surface via a silicone pad.

The pad in pad printing methods plays a major role in transferring the pattern from the printing form to the printing substrate (**Figure 2.1d**). The pad must be highly flexible since it must reach any target shape or surface structure. Pads come in different shapes, sizes and hardnesses. The most common commercial pad is made of silicon.

The next important part of pad printing technology is the pad printing inks. Nowadays, pad printing ink is available with diverse compositions, series, and colors. Basically, the ink selection depends on the target surface. In principle, the pad printing ink is similar to screen printing ink, except that pad printing ink is ten times thinner than screen printing ink. The solvent content in the pad printing ink is also higher than that in the screen-printing ink. This ensures a quality transfer of the printing ink.

The last important component in pad printing is the printing machine. Briefly, the printing machine consists of a drive (that controls the movement of the blade scraper to the left and right, as shown in **Figure 2.1**), pad holder, printing form table with an inking system. The printing machine itself differs by the inking system (e.g., open or closed ink system) and the driving mechanism (e.g., electromechanical, hydraulic, or pneumatic). **Figure 2.1** shows a partially closed ink system of a pad printing machine.

The pad printing process begins with the ink scraper moving toward the pattern plate until the plate is fully covered with ink (**Figure 2.1a**). Then the blade scraper moves backward toward the ink well to scrape the excess ink on the pattern plate (**Figure 2.1b**). Then the silicone pad moves downward to the pattern plate (**Figure 2.1c**). This process updates the ink on the silicone pad. Next, the silicone pad moves upward. Finally, the silicone pad transfers the 2D pattern onto the target surface (**Figure 2.1d**).

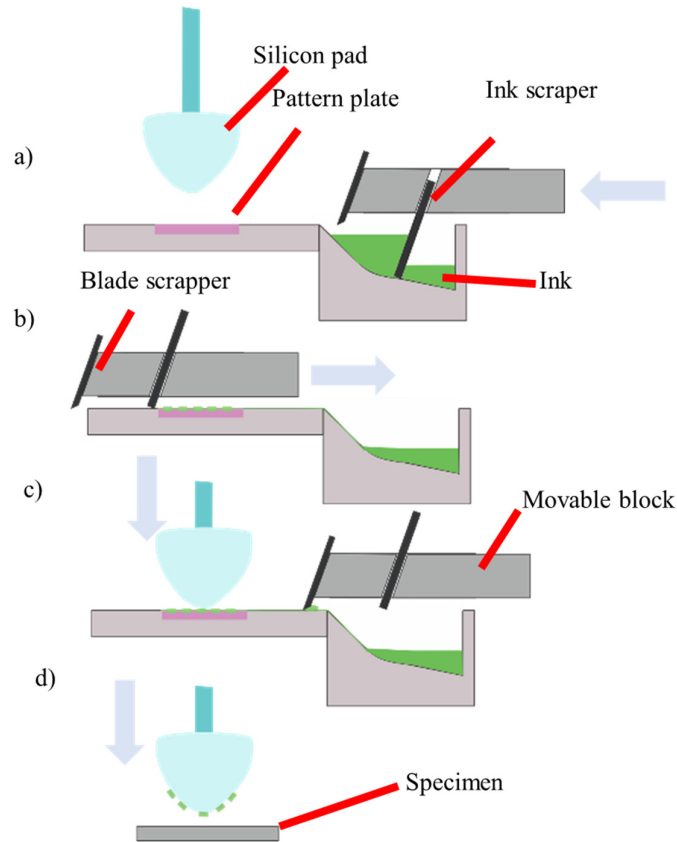


Figure 2.1. Mechanism of the pad printing method. (a) Ink updating process, (b) ink lamination on the pattern updater, (c) updating pattern on the silicone pad, and (d) pad printing process on the specimen.

In 2015, Poulin et al. fabricated the first stretchable electrode via pad printing.^[5] In this project, they claimed to fabricate a fully printed DEA. The DEA consisted of a silicone elastomer and stretchable electrodes made of a carbon black-elastomer composite. Briefly, their fabrication method started by stamping the carbon black elastomer composite onto the elastomer surface.^[5] By doing this, Poulin et al.^[5] achieved 1–2- μm -thick stretchable electrode membrane. This was combined with a 3- μm elastomer membrane. The lateral actuation of DEA was 7.5% at 245 V.^[5] Their pad printing process has some issues, including the requirement of a conductive liquid and an expensive, bulky pad printing machine.^[5] To achieve a high quality conductive liquid or composite silicone-carbon black pre-polymer, a long time mixing process is sometimes required.

2.2 Stretchable electrode fabrication based LS methods

In the 19th century, Pockels reported Langmuir films.^[14] These films consist of a monomolecular layer of amphiphiles floating on water. The monomolecular layer of amphiphiles is composed of molecules consisting of a non-polar nanoblock conjoined to a polar block with roughly the same size. When this type of monomolecular layer is spread on water, it tends to float at the air/water interface. Thus, they can easily be compressed using a movable barrier until the molecules are closely packed (**Figure 2.2b**).^[14] Slowly pulling a hydrophilic plate perpendicular to and through the floating monolayer from below can coat the plate with a packed monolayer.

This phenomenon was investigated by Blodgett, and later the method was named Langmuir-Blodgett.^[14] The Langmuir-Blodgett method is defined as a transfer of a monomolecular film onto a solid surface by vertically dipping in or out of a pool.^[14] In the LS method, the specimen or substrate is dipped into the floating monolayer (**Figure 2.2b**).^[14]

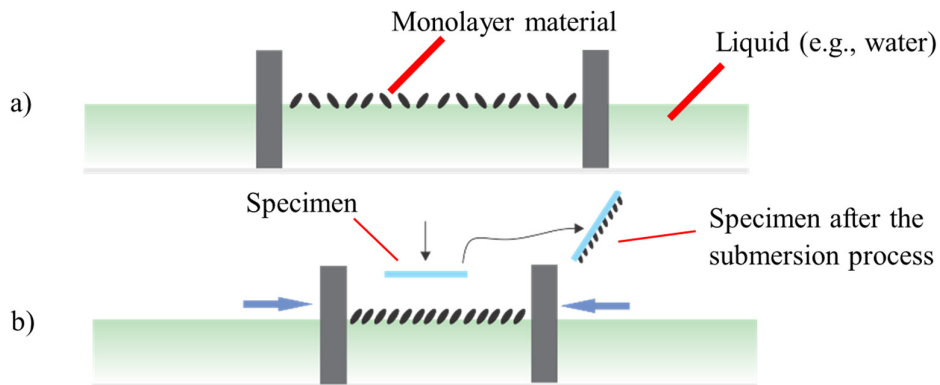


Figure 2.2. Basic concept of the Langmuir–Schaefer (LS) technique.

In 2018, Ji et al. used the LS method to fabricate a thin layer of stretchable electrodes.^[6] They applied this stretchable electrode to fabricate a DEA. Basically,

they prepared 0.4- μm -thick PDMS membranes. Then LS was used to deposit composite polythiophene-CNT monolayers onto 4- μm -thick PDMS membranes. Ji et al. reported that an average of 30-nm-thick electrodes were deposited on the 4- μm -thick PDMS membranes.^[6] They stated that the DEAs could achieve 4% linear strain with a driving voltage of 100 V. Ji et al. also used this fabrication method for different types of actuators, including a DEA Insect^[15] and a haptic feedback device.^[16] Their research also confirmed that fabrication methods of stretchable electrodes using the LS technique are reliable.

2.3 Stretchable electrode fabrication based on SCBI

SCBI is a popular gas-phase approach in nanofabrication. These implantation methods have attracted attention in both basic and applied research.^[17] In SCBI, aggregates of thousands of atoms are produced and carried in a supersonic regime. Researchers have reported that supersonic expansion in SCBI has several advantages for cluster manipulation compared to effusive beams.^[17] Hence, SCBI is a powerful approach for nanostructured film deposition. The supersonic cluster beam equipment consists of two chambers: an expansion chamber (**Figure 2.3**) and a deposition chamber. The expansion chamber contains a pulsed microplasma cluster source (PMCS). PMCS represents a combination of sputtering and laser vaporization cluster sources.

The implantation mechanism can be divided into three major processes: extraction of atoms from a solid sample, condensation of the atoms in clusters, and escape of clusters from the source due to the flow of inert gas. The inert gas carries clusters to the target surface.^[17] The vaporization process of metal in PMCS occurs simultaneously with the pulse injection of inert gas at approximately 40 bar.^[7] Then the metal atoms from the vaporization process are sputtered from the target and aggregate in the cluster source chamber to form a metal cluster (**Figure 2.3**). The mixture of metal cluster and inert gas expands through the expansion chamber. During the process, the expansion chamber is kept at 10^{-4} mbar.^[7] This difference in pressure accelerates the metal cluster to a supersonic speed. Then nanoparticles

accelerate through the aerodynamic focuser and finally reach the target surface in the second vacuum chamber (**Figure 2.3**).

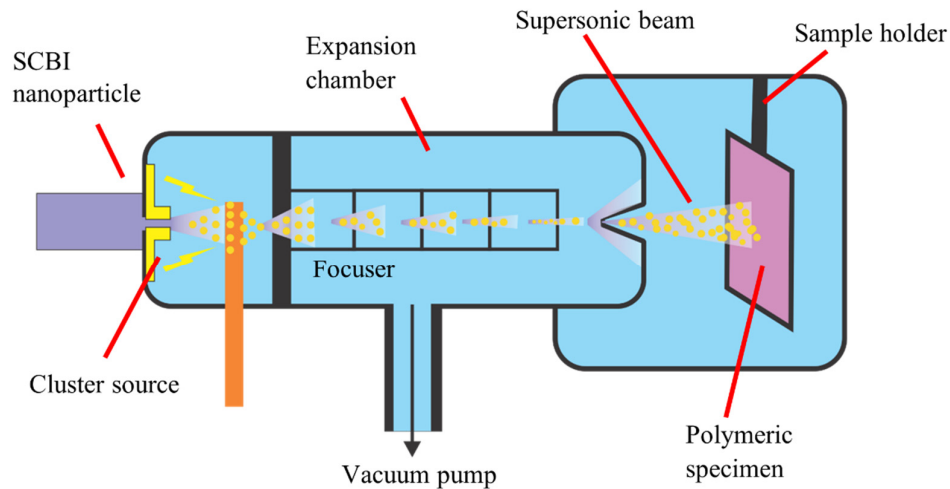


Figure 2.3. Supersonic cluster beam implantation (SCBI) technique.

Tacola et al.^[7] used SCBI to fabricate stretchable electrodes. They aimed to employ stretchable electrodes in low-voltage DEAs. In their research, the elastomer was PDMS. They used a spin casting method to fabricate an approximately 17- μm -thick PDMS membrane. The electrodes were Ag nanoparticles. The nanoparticles were directly patterned on the elastomer membrane. Tacola et al.^[7] reported that a 110-nm-thick Ag nanoparticle layer is achievable during the implantation process using SCBI. Based on DEA driving tests, they^[7] also reported that the DEAs can actuate up to 2.5% at 765 V.

2.4 Composite elastomer for stretchable electrodes

The name composite material comes from composition material.^[18] In principle, composite materials are produced from two or more essential materials. Normally, these essential materials have different mechanical and chemical characteristics. Mixing these materials creates a new material, which displays

different characteristics from the individual essential materials.^{[18][19]} Unlike a solid solution, the individual materials remain separate and are not fused in the final product.^[18] Composite materials allow researchers to design materials that meet their design requirements and applications.

Recently, researchers designed a stretchable conductive composite material. In 2018, Shintake et al. reported an ultra-stretchable strain sensor using carbon black (CB)-filled elastomer composites.^[2] Based on their report, the composite CB-based strain sensor can achieve a GF of 0.83–0.98 in the capacitive mode and a GF of 1.62–3.37 in the resistive mode. Since Ecoflex is the base material of this composite, the strain sensor has an ultrahigh stretchability of up to 500% strain at a strain rate of 50%/s. The strain sensor also has a high linearity and a lower hysteresis in the capacitive mode. In the case of the resistance mode, the sensor has a high hysteresis and nonlinearity.^[2]

2.5 Fabrications of CNT-based stretchable electrodes using manual brushing methods

Brushing is a simple method, which allows an uncertified user to complete the process. Powder-type electrodes (e.g., CNT, graphene nanoplatelets) are an excellent material for this method. CNT forms a cylinder with a micrometer length.^[20] This cylindrical form allows CNTs to create a strong network bonding during the brushing process. This strong network bonding between CNT particles can realize high-performance stretchable electrodes in terms of conductivity and stretchability.^[21]

A CNT powder and a high elastomer tackiness level are an excellent combination for brushing methods since the powder can easily adhere to the surface of the elastomer. A benefit of the brushing process is the ease of shaping and patterning. In this current research, a masking sheet was used to help define the shape of the CNT pattern on the elastomer (e.g., PDMS, Very High Bond (VHB) from 3MTM) membrane. The masking sheet was shaped and cut using a cutting plotter (Graphtec CE 6000-40).

The shaping process of the masking sheet is straightforward. The first step is designing the pattern using special software (e.g., Adobe Illustrator). The second step

is sending the design to the cutting plotter. In the final step, the cutting plotter cuts the design according to the design file. Once the masking sheet is ready, then it is adhered onto the surface of PDMS (**Figure 2.4(1)**) and the CNT powder is brushed onto a thin layer of the prestretched membrane made of Sylgard 184 to make a DEA or DE.

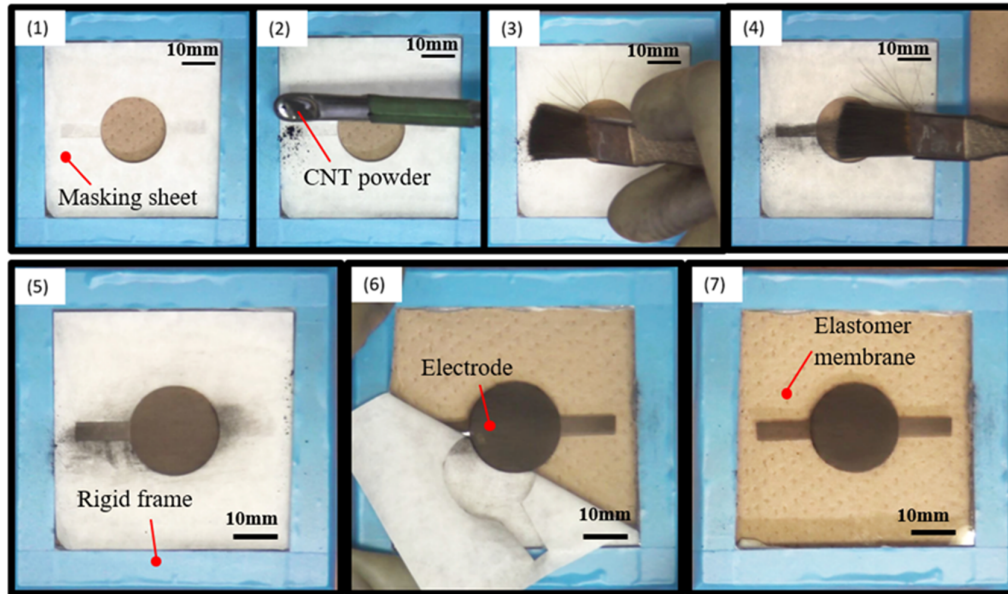


Figure 2.4. Brushing method for a stretchable electrode and fabrication method for a single-layer DEA.^[21] (Adapted from ref. ^[21] with free distribution permission under the CC-BY License.)

Figure 2.4 overviews the method to fabricate stretchable electrodes. The CNT powder used in this process was a multiwalled CNT (MWCNT724769-25G; Sigma-Aldrich). In the brushing method, the elastomer membrane was exposed to atmospheric pressure at room temperature. Then the multiple-brushing-method created a stretchable electrode layer on the PDMS membrane. The brushing cycle can be neglected since every elastomer sheet was fabricated using the same number of brushing times. To suppress the effect of the brushing direction, brushing of the MWCNT powder should be in the same direction.

2.6 Fabrications of CNT-based stretchable electrodes using an automatic brushing machine

To eliminate the human influence in the brushing process, improve the brushing consistency, and ease the burden of the brushing process, an automatic brushing machine is a breakthrough to automate the brushing process. In this current research, a commercially available automatic brushing machine (SainSmart Genmitsu CNC Router 3018-PRO) was customized as a DIY-Kit x-y-z machine tool. To ease the CNT powder handling in the brushing process, the x-y-z machine tool was placed inside a commercially available glove box (As One 3-116-01 SM-1). Additionally, the brush was a readily available commercial paintbrush with nylon hair (**Figure 2.5**).



Figure 2.5. Wooden brush with synthetic nylon hair.^[20] (Adapted from ref. ^[20] with free distribution permission under the CC-BY License.)

The brushing process began by placing the electrode powder on the elastomer surface (**Figure 2.6a**). The MWCNT powder was pre-poured (approximately 0.02 grams) from the top left corner to the bottom left of the PDMS-PEIE surface to form a line (**Figure 2.6a**). Then a series of bi-directional planar sweeps along the linearized rail brushings was performed at a speed of 1000 mm/min (**Figures 2.6c, d, and e**) until the entire elastomer surface was covered with the electrode powder (**Figure 2.6f**). The strategy ensured a uniform brushing by performing 20 brushing cycles at each position.

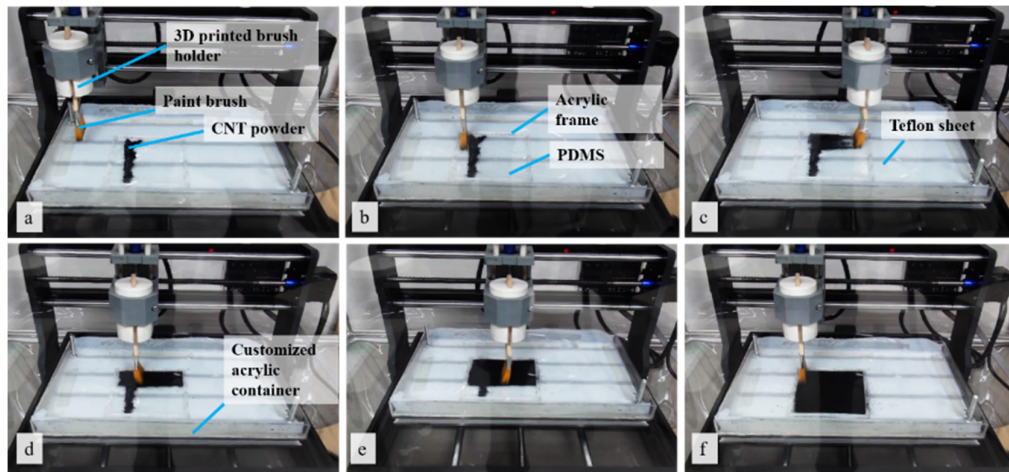


Figure 2.6. Equipment setup and brushing process using a brushing machine. (See Movie S1 to view the complete process). (Adapted from ref. ^[20] with free distribution permission under the CC-BY License.)

2.7 Conclusion

All fabrication methods have strengths and weaknesses. For example, the pad printing process is simple and straightforward, but it requires bulky and expensive equipment. This is similar to other methods such as SCBI and LS. These methods are simple methods. However, they require additional equipment, additional material, trained personnel, and complex processing.

Compared to other fabrication processes, the brushing process is relatively fast, simple, and cost-effective. The brushing process has some weaknesses such as the possibility of delamination of the powder electrodes and the need for a highly ventilated room. The self-delamination problem is due to the absence of bonding between agglomerates and surface of the elastomer, which can be easily overcome by optimizing the elastomer surface properties.^[21] Additionally, the requirement for a well-ventilated room can be solved by a glove box, as reported by Wiranta et al.^[20] The brushing method has more benefits for new researchers in soft robotics, especially in the field of DEAs and sensors since it is cost-effective, easy, and reliable.

Chapter 3

Simple Manual Brushing Methods to Fabricate PDMS Powdered-based DEAs

3.1 Introduction

DEAs are energy efficient,^[22] compact,^{[23][24]} and operate silently.^{[21][25]} Currently, electro-mechanical types of soft actuators include soft pneumatic actuators,^{[26]–[28]} stretchable pumps,^{[29][30]} and DEAs.^{[3][23][31]–[36]} Soft pneumatic actuators can generate high-pressure actuation, which may expand soft actuator applications to areas that require high-pressure actuators. However, soft pneumatic actuators require additional equipment such as air hoses and compressors, which may lead to complex designs.^{[26]–[28]}

Stretchable pumps utilize ElectroHydroDynamics (EHD) to generate pressure differences between the fluids inside the device. Recently, rapid fabrication methods for EHD pumps have been established using a DIY-like method.^{[37][38]} The fabrication process includes cutting a copper sheet and assembling the pump manually, which can produce five pumps per hour.^[37] Such rapid prototyping is essential to boost innovation in the soft actuator area. In contrast, DEAs are a newly developing technology, which are simpler than EHDs (that requires dielectric liquid), and pneumatic actuators (that require air compressors). However, further research is required to understand the performances and applications of DEAs. Typical strategies, which are similar to those in previously reported research on EHD pumps to achieve fast, reliable, and low-cost fabrication, are essential to accelerate DEA research.

DEAs convert electrical energy into mechanical energy. **Figure 1.1** depicts the DEA structure. In principle, a DEA consists of a DE membrane sandwiched between two stretchable electrodes.^{[39]–[42]} Applying a voltage at both electrodes realizes a Maxwell Pressure (P). As shown in **Figure 1.1b**, the Maxwell pressure squeezes the dielectric membrane in the z -direction. Assuming that the DE membrane is

incompressible, the DEA expands to the x-y direction due to compression in the z-direction (**Figure 1.1b**).

The performance of DEAs depends on the mechanical characteristics of the elastomer (**Equation 1.2**).^{[43]–[46]} A less stiff elastomer and highly stretchable electrodes can increase the actuation performance of DEAs. Currently, acrylate-based polymers such as VHB are popular for DEAs. Although VHB has a relatively high dielectric constant and large strain, it also shows high viscoelasticity properties. The high viscoelasticity properties affect the relaxation time during the stretching and relaxation cycle, which may reduce the responsivity of DEAs. Furthermore, VHB has high stickiness characteristics and is easily broken under highly prestrained conditions.^{[1][47]} Hence, careful treatment is necessary when using VHB to fabricate DEAs. On the other hand, PDMS has some benefits such as economical, biocompatible, and stretchable.^[48] The small viscoelastic characteristics of PDMS can realize highly responsive DEAs.^[49]

To maximize the actuation performance, DEAs require a highly stretchable electrode. Ideally, stretchable electrodes should preserve their electrical conductivity while sustaining large deformations and exhibit a durability for millions of cycles. **Chapter 1** elaborated about several methods to fabricate stretchable electrodes. Each method has its own strengths and weaknesses when fabricating electrodes for DEAs.

To accelerate the development of soft actuators, especially DEAs, simple and reliable methods should be established. This chapter aims to report a fast, reliable, and low-cost fabrication of DEAs. The strategies utilize a soft brush to directly pattern CNT powder on the elastomer membrane. The first step was to optimize PDMS-based DEAs by tuning up the mechanical and surface-adhesiveness characteristics of a PDMS membrane. This can be achieved by altering the mixing ratio of the curing agent and base polymer. A uniaxial tensile test was used to investigate the effect of the mixing ratio on the mechanical characteristics of the elastomer. A tackiness test was also performed to assess the surface adhesivity of the elastomer. The CNT network conditions after the brushing were examined using Field Emission Scanning Electron Microscopy (FE-SEM). The results show that the mechanical characteristics of PDMS are controllable and modifying the mixing ratio

adjusts the surface adhesivity of the elastomer. Additionally, the FE-SEM images indicate a strong network connection between CNT particles.

3.2 Investigation of elastomer mechanical characteristics

This subchapter investigates the influence of the mixing ratio on the PDMS mechanical characteristics. Commercial PDMS named Sylgard 184 (Dow Corning) was used. Sylgard 184 is available in the resin form with two liquid parts: the elastomer base (A) and the cross-linking curing agent (B). To produce solid silicone, these parts should be mixed using the recommended mixing ratio of 10-1 (10 for part A and 1 for part B) and cured at 60 °C to realize a short curing time. To ensure standardization and repeatability, parts A and B were mixed using a commercial mixer (Thinky mixer AR-100) for 3 minutes at a speed of 2000 rpm.

According to **Equation 1.2**, a softer material induces a higher actuation performance of DEAs. Here, the mixing ratio of part A and part B is optimized to achieve higher actuation performances of DEAs. Three different types of PDMS (Sylgard 184) samples (PDMS 10-1, PDMS 20-1, and PDMS 30-1) were prepared by a simple molding and curing process to form sheets with dimensions of 145 mm × 135 mm × 2 mm. Then strips were fabricated using a precision dumbbell blade according to JIS K6251. Single failure tensile tests were conducted using Shimadzu AGS-X with a loading speed of 500 mm/min. The elongation and applied force during the test were recorded automatically. The data from at least three tests under the same conditions were averaged.

Figure 3.1 describes the uniaxial engineering tensile test results for the three different PDMS samples, which were prepared with different mixing ratios. In the small strain region (below 50%), the stress–strain curve shows a linear behavior. However, the stress steeply increases in the large strain region above 100% strain for PDMS 10-1 and 175% for PDMS 20-1 and PDMS 30-1. These data indicate that reducing the curing agent produces a softer material and the mechanical properties of PDMS are controllable. In this research (for PDMS-based DEA), a softer PDMS with less curing agent is preferable to drive DEAs with a lower actuation voltage. A

softer PDMS also has a more stretchable structure and may produce a higher actuation performance.

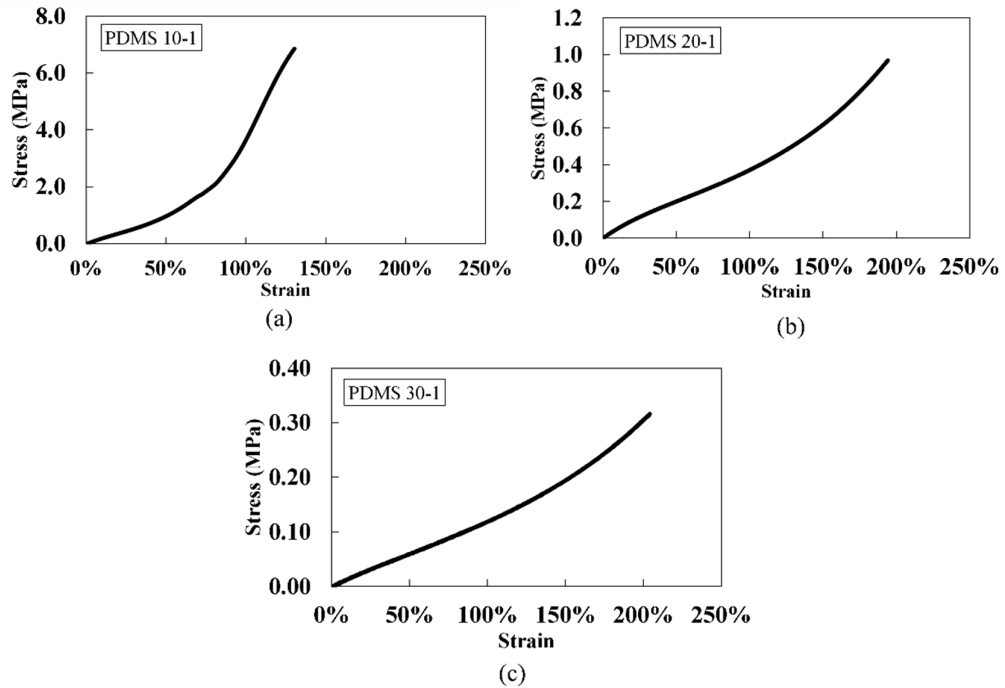


Figure 3.1. Engineering stress–strain curves of the PDMS samples made with various ratios of the base polymer and the curing agent. (Adapted from ref. ^[21] with free distribution permission under the CC-BY License.)

An additional engineering cyclic tensile test for PDMS 10-1, PDMS 20-1 and PDMS 30-1 were also performed. In the cyclic tensile test experiment (**Figure 3.2**), the shape of the test specimen was the same as that used in the uniaxial tensile test (JIS K6251). In this experiment, the sample was a sheet measuring 145 mm × 135 mm × 2 mm. Sample fabrication involved a simple molding and curing process. Then the coupon test strips were fabricated using a dumbbell blade according to JIS K6251. The equipment used in this experiment was a Shimadzu AGS-X tensile tester. The loading speed for the cyclic tensile test was 500 mm/min.

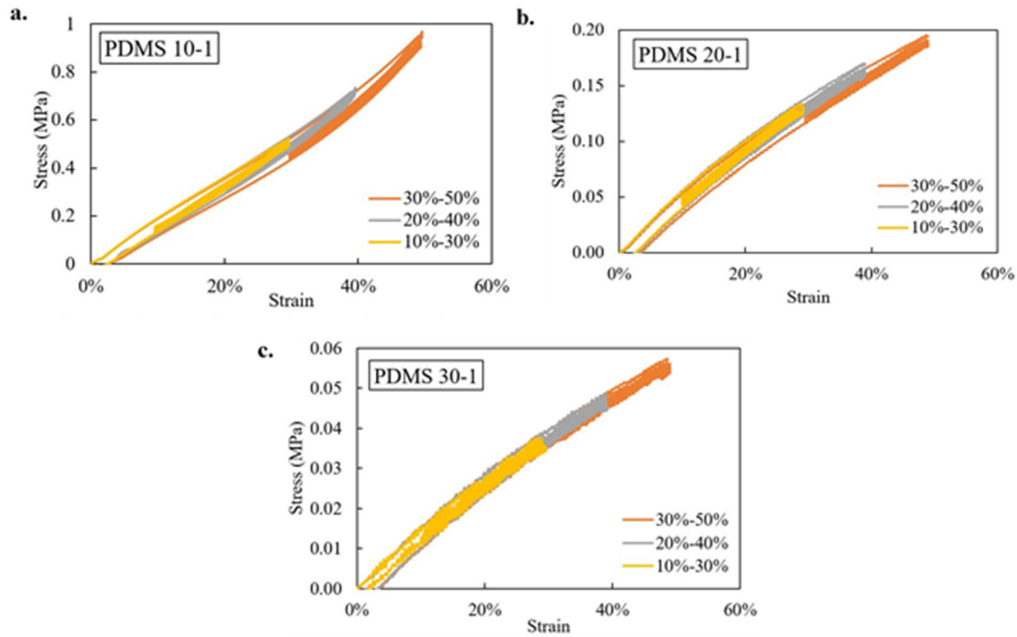


Figure 3.2. Cyclic tensile test results from three different specimens. (a) PDMS 10-1, (b) 20-1, and (c) 30-1. (Adapted from ref. ^[21] with free distribution permission under the CC-BY License.)

Three different cyclic tensile test conditions were made for each sample (PDMS 10-1, PDMS 20-1, and PDMS 30-1). First, the specimen was pulled to 10% strain, and the cyclic test was done between 10–30% strain. The specimen was relaxed to the initial condition (at 0% strain) at the end of the tenth cycle. In the second condition, the specimen was initially pulled to 20% strain and the cyclic test was done between 20–40% strain. In the third condition, the specimen was initially pulled to 30% strain and the cyclic test was done between 30–50% strain. These cyclic tensile tests evaluated the influence of prestretching on the reaction of PDMS 10-1, PDMS 20-1, and PDMS 30-1 in the cyclic tensile test.

Figures 3.2a, b and **c** indicate that there are gaps between the first pull and the last tenth load-unload-reload cycle test. These gaps are due to the stress softening effect of the elastomer in each cycle. This stress-softening leads to hysteresis in the engineering stress-strain curve. Furthermore, this stress softening in the elastomer

specimen may be affected by the viscoelastic characteristics of the elastomer as these characteristics affect the relaxation time of the elastomer, which realizes stress softening that is recorded in the engineering stress-strain curves. The relaxation time affects the dynamic characteristics of the DEAs. We found that the cyclic actuation of DEAs drifts from their equilibrium position (by 0.4% for PDMS 20-1 and 2.9% for PDMS 30-1).

3.3 Surface tackiness characteristics of PDMS membranes

This subchapter evaluates the influence of the mixing ratio on the stickiness of the PDMS sheet. There are several test methods to assess the stickiness based on the force direction measured experimentally with respect to the sample surface. These include normal adhesion tests (force and displacement measured parallel to the normal preload), shear tests (force and displacement measured perpendicular to the normal preload), and peel tests (sample is peeled from the substrate at a defined angle).^[50]

According to the American Society for Testing and Materials (ASTM D 6195 03), tackiness is the force required to separate an adherend and an adhesive at the interface shortly after they have been brought rapidly into contact under a light load with a short duration. To evaluate the tackiness level, ASTM D 6195 03 provides a detailed measurement procedure called the loop tack test.

For the loop tack test, the PDMS membrane was cut into a 25 mm × 175 mm specimen strip. Then the specimen was bent back upon itself to form a teardrop-shaped loop. The end of the loop was fastened together by masking tape before inserting it into the grips to prevent contaminating the tensile tester grips. Next the loop was brought into contact with the precleaned substrate (polished stainless-steel SUS 430 with a 25 mm × 25 mm contact area) by lowering the loop until it covered the substrate surface. **Figure 3.3** shows the experimental settings for the loop tack test. The area in contact was inspected visually for any imperfections in the contact (e.g., wrinkles). Finally, the tensile test machine pulled the test sample at a speed of 300 mm/min until the PDMS membrane detached from the substrate surface, and the pulling force and displacement of the loop were recorded.

Figure 3.4 shows the maximum tackiness of the PDMS membrane. As expected, increasing the curing agent (wt%) reduces the tackiness of the PDMS. The tackiness quality of the PDMS can affect the amount of MWCNT preserved on the elastomer during the brushing process. A stickier elastomer should preserve more MWCNT on the elastomer surface, which in turn should enhance the conductivity of the stretchable electrodes. The next chapter shows the effect of tackiness on the electrical properties of the MWCNT electrodes deposited on PDMS surfaces.

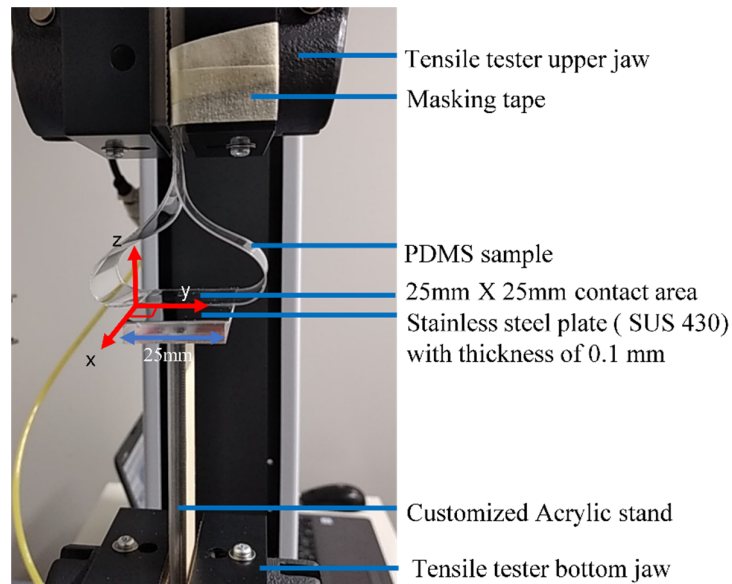


Figure 3.3. Tackiness evaluation of PDMS membranes. (Adapted from ref. ^[21]

with free distribution permission under the CC-BY License.)

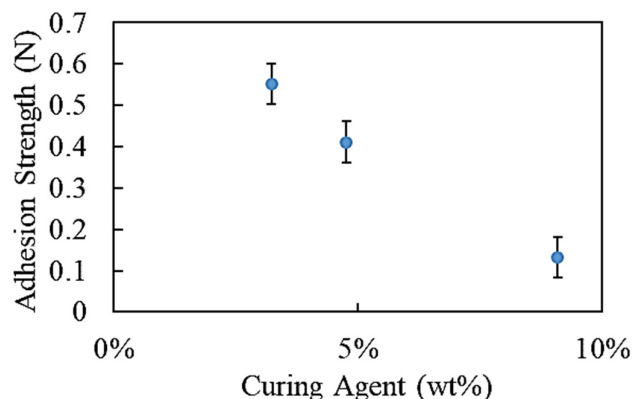


Figure 3.4. Maximum tackiness of the PDMS membranes. (Adapted from ref. ^[21] with free distribution permission under the CC-BY License.)

3.4 Electromechanical properties of CNT powder-based stretchable electrodes

The electromechanical properties of the stretchable MWCNT networks brushed on the elastomers were examined using the four-probe method, as recommended in a previous study.^[51] The mechanical and electrical coupling measurements were established to test the resistance–strain characteristics of the brushed MWCNT on PDMS membranes. In principle, a long and thin rectangular strip of the elastomer was prepared with the MWCNT powder brushed on the elastomer.

Figure 3.5 depicts the equipment arrangement for the electromechanical tests. The length (L_s) was 50 mm. The aspect ratio (L/w) was 10:1, which ensured a homogenous current flow.^[51] The strips were measured by the four-probe method to avoid measuring the contact resistance. For the measurements, the sample was connected to a magnetic probe to ensure a uniform contact force in every test specimen. In the test system, the elastomer was pulled at a constant speed of 1 mm/s using Shimadzu AGS-X, and an LCR meter (IM3536) measured the resistance signal of the sample during the tensile test. All three sheet groups (PDMS 10-1, PDMS 20-1, and PDMS 30-1) were measured using the above method in a zero-strain condition. Then the strips were stretched in the uniaxial direction until a strain of 0.3 was achieved. The shrinkage in the width direction was neglected because it was insignificant compared to the extension of PDMS.

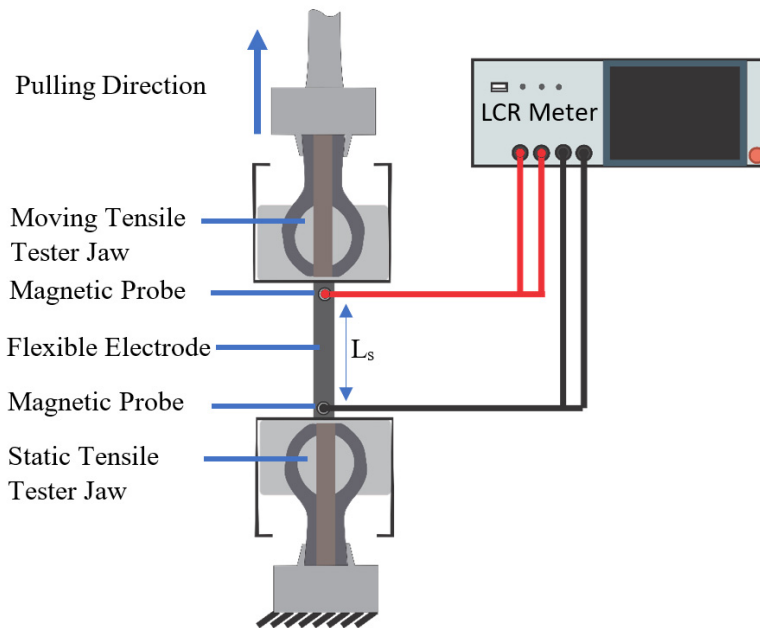


Figure 3.5. Electromechanical measurement of a stretchable electrode. (Adapted from ref. ^[21] with free distribution permission under the CC-BY License.)

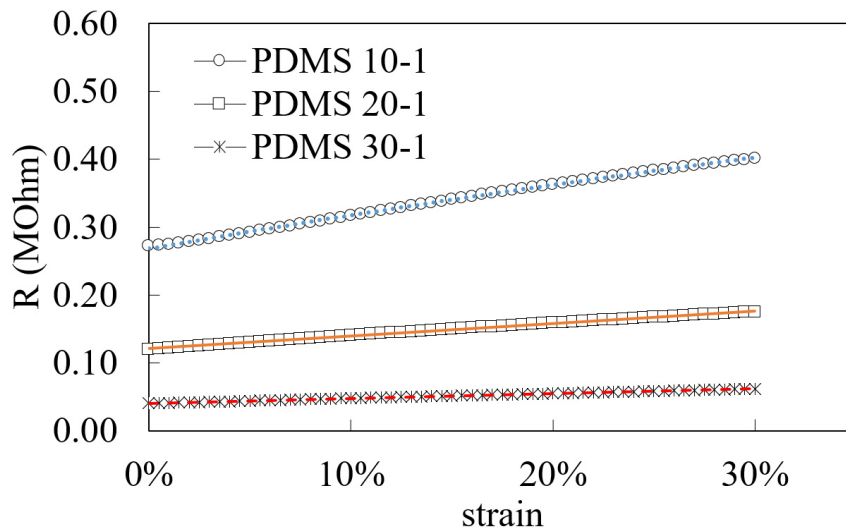


Figure 3.6. Change in the resistance value during tensile tests of the stretchable electrodes. (Adapted from ref. ^[21] with free distribution permission under the CC-BY License.)

Figure 3.6 shows the influence of the mixing ratio of PDMS on the resistance of the brushed MWCNT. Increasing the curing agent portion elevates the electrical resistance of the brushed MWCNT on PDMS. The electrical resistance is influenced by the amount of powder attached to the surface of the elastomer. This elevated electrode resistance leads to the low conductivity of a stretchable electrode. The resistance increases as the strain increases due to the increased spacing among the nanoparticles comprising the conductive network.^[52]

Figure 3.7 shows the stretchable electrode when subjected to DC of 5 V as the electric source while stretching. In the initial condition ($e=0$), the brightness of the light emitted by the LED increases linearly with the density of the base polymer ratio. The brightness for a higher ratio of the base polymer is attributed to the better electrode conductivity performance.

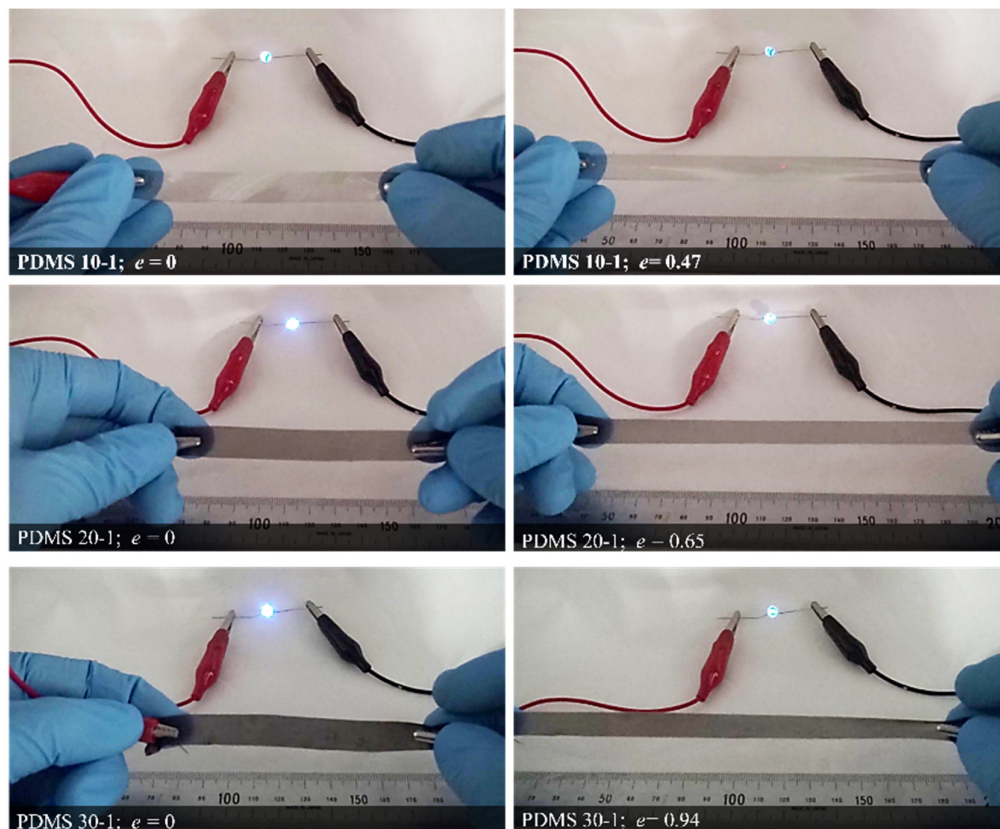


Figure 3.7. Demonstration of a stretchable electrode when subjected to an electric current under uniaxial strain. (Adapted from ref. ^[21] with free distribution permission under the CC-BY License.)

3.5 Surface conditions of brushed multiwalled CNTs on elastomer membranes

The surface conditions of the elastomer membranes were examined after the brushing process utilizing field emission scanning electron microscopy (FESEM JSM-7610F; JEOL). **Figure 3.8** describes the surface morphology of the brush-painted MWCNT electrodes on various PDMS samples by the color density. The MWCNT density increases as the sticky nature of the elastomer increases. Adjusting the mixing ratio of the base polymer and the curing agent controls the stickiness. The sticky nature of PDMS helps maintain the MWCNT powder on the elastomer surface. Because the brushing method also helps build a connection between the MWCNT network, it improves the conductivity of the stretchable material.^[53]

Compared to the first and second-brushed MWCNT electrodes (**Figures 3.8a and b**), the third electrode (**Figure 3.8c**) shows lower optical transmittances. **Figure 3.8d, e, and f** show SEM images with different amounts of the MWCNT powder deposited on PDMS surfaces using the same number of brushing cycles. The MWCNT powder deposited on the surface of the elastomer membrane increases as the base polymer ratio in the mixture increases. **Figure 3.8i** has more layers of MWCNT than the other MWCNTs brushed on the elastomer membranes.

Furthermore, to evaluate the effect of the cyclic tensile test on the surface morphology of brush-painted MWCNTs on PDMS, a rectangular-shaped test specimen similar to that tested in **Figure 3.5** was prepared. The specimen was 100-mm long and 10-mm wide. The specimen underwent a cyclic tensile test at a speed of 500 mm/min and a maximum strain of 40% using Shimadzu AGS-X. Then the material was also investigated using FESEM JSM-7610F (JEOL). **Figure 3.9** shows that the PDMS surface has dense MWCNTs. The cyclic tensile test does not have significant effect to the MWCNT deposited on PDMS (**Figures 3.9a, b, and c**), as indicated by the similarity between **Figure 3.9** and **Figures 3.8d, e, and f**. As expected, the strong bonding between MWCNT is maintained on the nanometer scale and PDMS 30-1 has more MWCNT attached to its surface because it has a higher tackiness than the other samples.

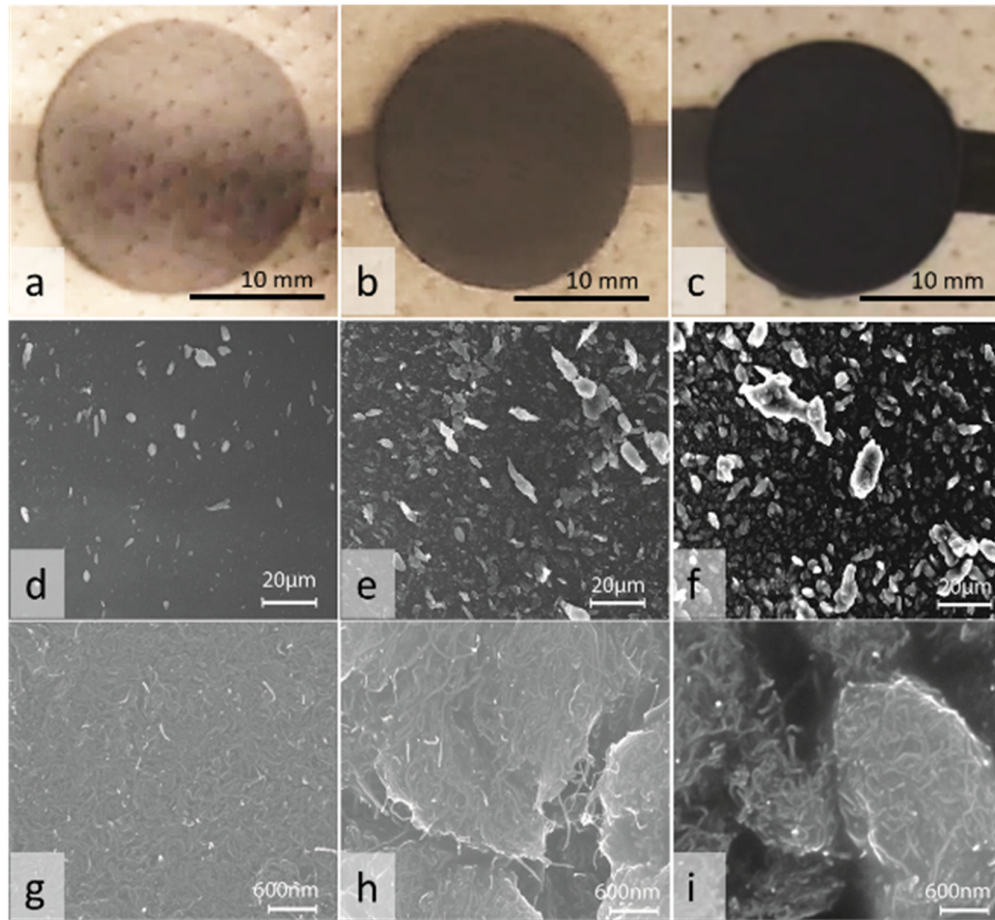


Figure 3.8. Surface morphology of brush painted MWCNT on the elastomer membrane. Brushed MWCNT on PDMS with a mixing ratio of (a) 10-1, (b) 20-1, and (c) 30-1. (d and g) SEM images of the brushed MWCNT on PDMS 10-1. (e and h) SEM images of the brushed MWCNT on PDMS 20-1. (f and i) SEM images of the brushed MWCNT on PDMS 30-1. (Adapted from ref. [21] with free distribution permission under the CC-BY License.)

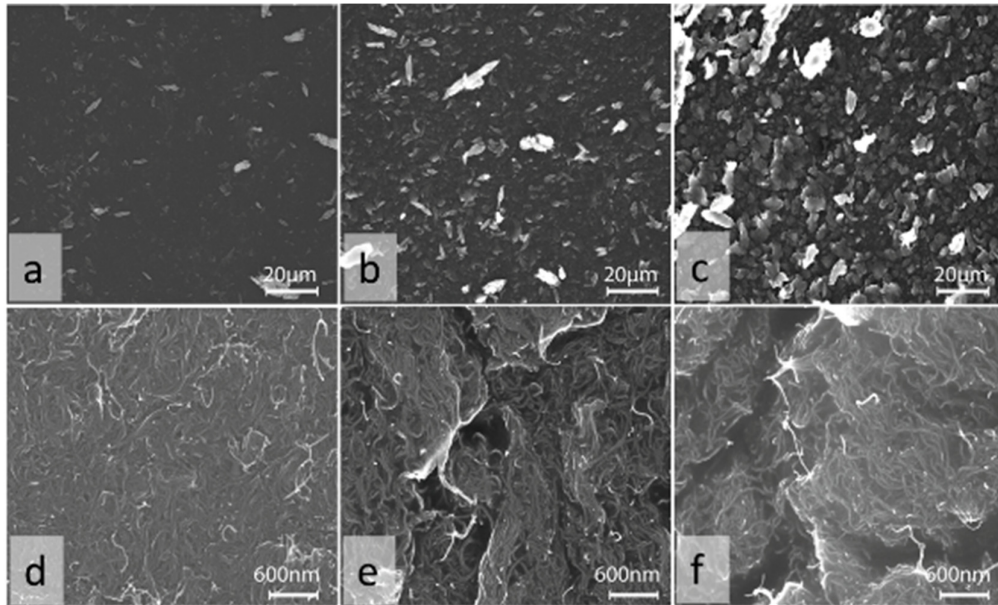


Figure 3.9. SEM images from brushed MWCNT on the PDMS membrane after 20-cyclic tensile tests for (a and d) PDMS 10-1, (b and e) PDMS 20-1, and (c and f) PDMS 30-1. (Adapted from ref. ^[21] with free distribution permission under the CC-BY License.)

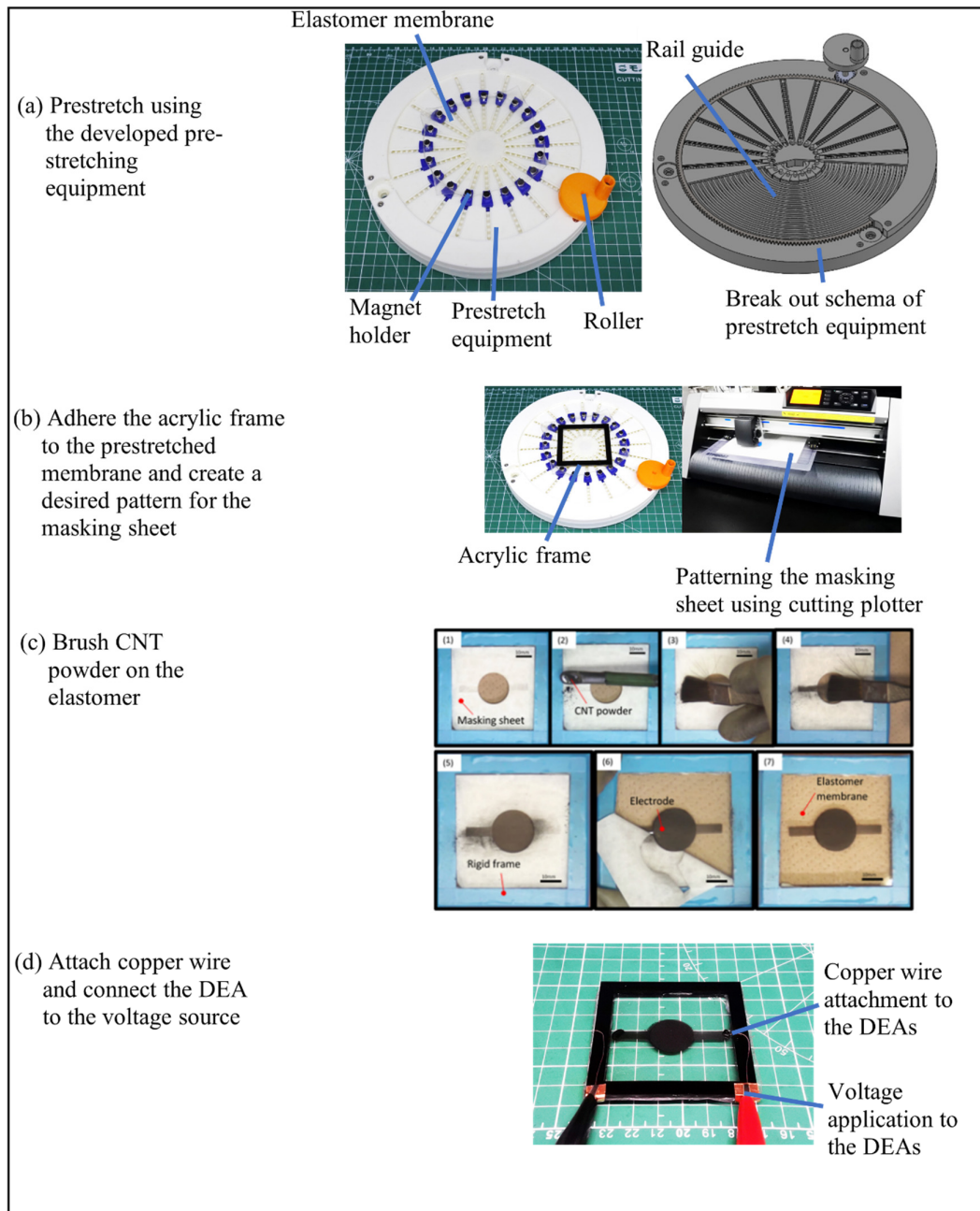


Figure 3.10. Complete fabrication process of single layer DEAs. (Adapted from ref. [21] with free distribution permission under the CC-BY License.)

3.6 Fabrication methods of DEAs

To further investigate the reliability of stretchable electrodes fabricated using brushing methods, the fabricated electrodes were applied on a single-layer DEA. The DEAs tests used elastomer PDMS 10-1, PDMS 20-1, and PDMS 30-1. A 0.5-mm-thick PDMS membrane was fabricated using a simple coating process on an acrylic plate. The mixing and curing processes were similar to those previously discussed.

Figure 3.10 shows the step-by-step process to fabricate a single-layer DEA. The first step was prestretching the elastomer using a prestretching machine (**Figure 3.10a**). Prestretching was either 10%, 20%, or 30%. Then to maintain the prestretch condition, an acrylic frame was adhered to the surface of the elastomer (**Figure 3.10b**). Next, the stretchable electrode patterning process began.

Prior to the brushing MWCNT on the elastomer, a pre-holed masking sheet was attached to the surface of the elastomer to shape the electrode (**Figure 3.10c (1)**). The hole size had a 20-mm diameter. To prevent the MWCNT from tarnishing another position, the masking sheet was designed to cover the whole surface of the membrane (the masking designing process used Adobe Illustrator). Then the masking sheet was cut according to the design by a cutting plotter (Graphtec CE 6000-40). Afterwards a small amount of the MWCNT powder was poured (**Figure 3.10c (2)**) and brushed on the entire surface (**Figure 3.10c (3)** and **c (4)**) until all layers were covered with MWCNT (**Figure 3.10c (5)**). After brushing both surfaces of the PDMS membrane, the masking sheet was removed and a copper wire was attached on both surfaces of the electrode. The final step was to apply a high voltage to the DEAs (**Figure 3.10c (7)**).

3.7 Static characteristics of DEAs

Applying a voltage to both electrodes induces DEA actuation. To understand the effect of stress softening on the DEA performance, PDMS membranes with various mixing ratios were investigated (PDMS 10-1, PDMS 20-1, and PDMS 30-1). All sheets had an initial thickness of approximately 0.5 mm and were prestretched by

10%, 20%, or 30%. MWCNT was coated by the brushing method on both surfaces with an overlapping circular region. This circular region was defined as the electroactive region. When a DEA actuates, the electroactive region expands against the passive region of the DEA (**Figure 3.11d**).

To easily capture DEA actuations, a single-layer DEA was placed on a light board LED and a high definition (HD) camera was used to record DEA actuation. The area expansion recorded by the HD camera was further analyzed using Image J to calculate the area strain. The area strain was determined by the change in the electroactive areas through geometric relations.^[1]

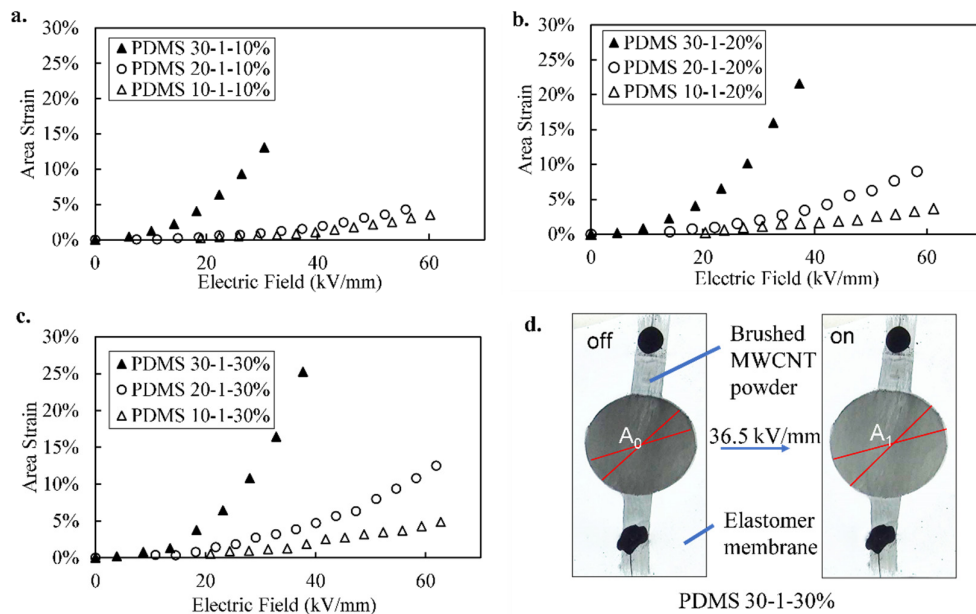


Figure 3.11. Area strain as a function of the electric field at various PDMS mixing ratio with the prestretching of (a) 10%, (b) 20%, and (c) 30%. (d)

Photos of the actuators constructed from PDMS 30-1 and 30% prestretching. (Adapted from ref. ^[21] with free distribution permission under the CC-BY License.)

Figures 3.11a, b, and c show various actuation characteristics of DEAs due to the variation in the mixture ratio between the curing agent and base elastomer. As the curing agent ratio in the mixture increases, the actuation performance decreases. For

all prestretched conditions, the device using PDMS 10-1 as the membrane does not show a significant increase in actuation compared to the others. Hence, stress hardening due to excessive curing agent affects the DEA performance. Because the PDMS 10-1 membrane has rigid characteristics, a higher driving voltage is required to achieve a higher area strain. Furthermore, the surface characteristic of PDMS 10-1 is less sticky than those of PDMS 20-1 and PDMS 30-1. The less sticky surface characteristic limits the ability of the membrane to preserve the MWCNT powder on its surface, lowering the electrode conductivity. In this case, the combination of a stiff membrane and a lower electrode conductivity reduces the DEA actuation performance.

Devices using PDMS 20-1 show almost the same actuation performance as PDMS 10-1 for the lower prestretched condition (10% prestretching). However, the performance is improved as the prestretched condition increases (**Figures 3.11b** and **c**). PDMS 30-1 shows the best performance, but devices using this membrane exhibit a lower electrical breakdown field. This is attributed to the DEA characteristic where PDMS is used as the elastomer membrane and MWCNT as the electrode. These results show that the stress-softening and surface characteristics affect the DEA area strain.

3.8 Dynamic characteristics of DEAs

The cyclic performance of DEAs was experimentally tested using a sine wave with a frequency of 4 Hz for 250 seconds. Similar to the static test, the cyclic test used an HD camera with a recording speed of 30 frames per second to record the cyclic motion. The recorded motion was further analyzed by Image J software.

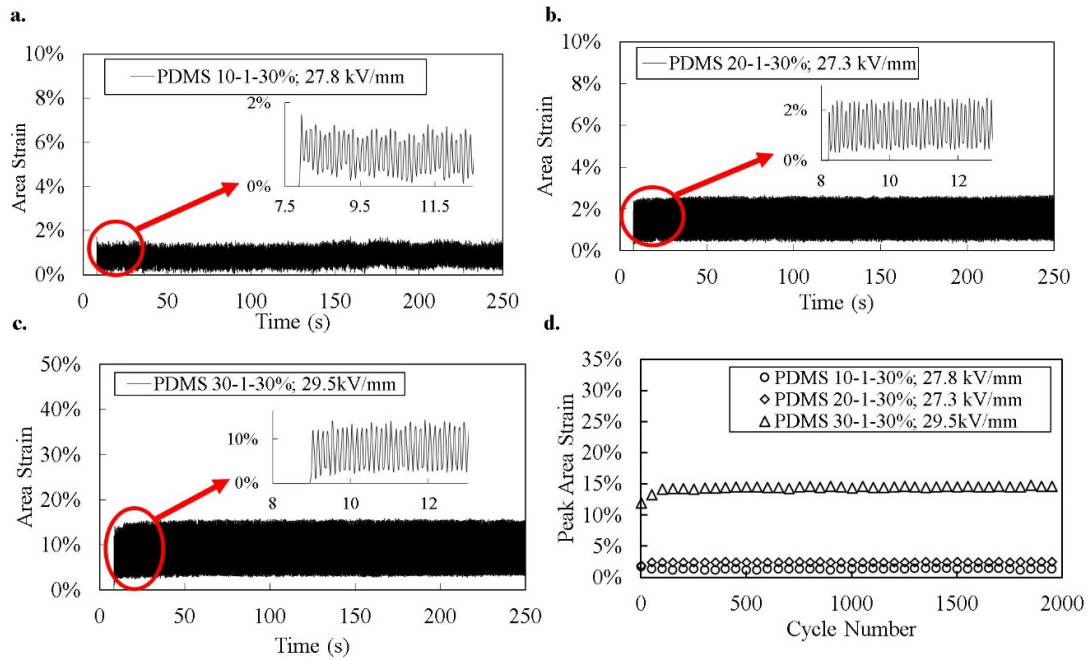


Figure 3.12. Dynamic performance of powdered-based DEAs. (a) PDMS 10-1 with 30% prestretching, (b) PDMS 20-1 with 30% prestretching, and (c) PDMS 30-1 with 30% prestretching. (d) Summary of the peak actuation of PDMS 10-1, PDMS 20-1, and PDMS 30-1 with 30% prestretching. (Adapted from ref. ^[21] with free distribution permission under the CC-BY License.)

Figure 3.12 shows the first 250-second cyclic actuation of a device constructed from PDMS 10-1, PDMS 20-1, and PDMS 30-1 with 30% prestretching. **Figure 3.12d** summarizes the peak area-strain from **Figures 3.12a, b, and c**. The area strain remains stable as the number of cycles increases. The stable actuation area is a satisfactory feature of DEAs using MWCNT powder as the electrodes. This result demonstrates that the brushing method can fabricate DEAs that can endure high actuation cycles. Consistent with previous research, which found that the binding between the MWCNT powder and the elastomer surface may affect the DEA performance,^[3] this research confirms that the binding force between the MWCNT

powder and the elastomer membrane affects the stability of cyclic actuation. The DEA elastomer membrane in **Figure 3.12c** is stickier and exhibits a more stable actuation performance in every cycle than the others (**Figures 3.12a** and **3.12b**).

Samples of PDMS 20-1 (**Figure 3.12b**) and PDMS 30-1 (**Figure 3.12c**) drift from their equilibrium position by 0.4% and 2.9%, respectively, in the stable state. Similar behaviors have been observed in elastomers with a high viscoelasticity such as VHB polymers.^[54] PDMS 10-1 (**Figure 3.12a**) shows a relatively small drift compared to the other two samples since PDMS 10-1 shows a smaller area actuation strain.

3.9 Conclusion

This chapter demonstrates a manual brushing process to fabricate stretchable electrodes. The straightforward fabrication process uses a commercially available soft brush and MWCNT (MWCNT724769-25G; Sigma-Aldrich). The elastomer used in this research was Sylgard 184. Several tests were used to verify the quality of the stretchable electrodes in the DEAs. Stretchable electrodes are suitable for DEAs.

Manual brushing methods are satisfactory for DEA applications. The mechanical and stickiness characteristics of PDMS can be controlled. Since the characteristics of the elastomer are controllable, the DEA performance can also be controlled. The stable dynamic performance of DEAs shows that the powder delamination risk is reduced.

Chapter 4

Automatic Brushing Method for Stretchable Electrodes and Integration of Powdered-based Stretchable Sensors for Wearable Devices

4.1 Introduction

Wearable devices and soft robotics are becoming a good combination for flexible devices for systems with human interactions. Examples include flexible devices for rehabilitation or assistance purposes,^{[55][56]} human health monitoring systems,^{[57][58]} human-machine interactions,^{[59]–[61]} and human motion monitoring.^{[62][63]} Many soft actuator devices have been developed such as soft pneumatic actuators,^{[26][64]–[67]} soft electroadhesion,^{[68]–[71]} stretchable pumps,^{[29][37][38][72][73]} DEAs,^{[15][21][34][74]–[80]} shape memory polymers,^{[81]–[85]} and gel actuators.^{[86]–[91]} To create an interaction between soft actuators and human activity, the actuator must be equipped with an appropriate sensing method such as a pneumatic exoskeleton.^[56] The exoskeleton amplifies the normal muscle work precisely when the sensor and actuator are fully calibrated with the human motion.

As human-soft robot interaction technologies advance, the interest in stretchable sensor devices has increased. In the context of human motion detection and soft robotics actuation monitoring, strain sensing is essential to detect deformations of the system. Although conventional strain sensors can convert the strain produced by an external stimulation into a signal response,^[92] they cannot detect the full range of human motions. The conventional strain sensor structure usually consists of a high stiffness material conductor or semiconductor, which limits the strain sensing range.^[93] Since the movement of human joints induces a large strain range (more than 30%), flexible strain sensors with a high stretchability are needed to detect the full range of human motions.^[20]

Currently, the development of stretchable strain sensors via rapid, easy, reliable, and cost-effective fabrication methods remains a challenge, although the demand for

stretchable strain sensor products is high.^[9] To achieve rapid, easy, and cost-effective fabrication methods, DIY-like methods need to be established. In principle, DIY is an activity where researchers create a product or a process through individual or a collective production practice for a specific purpose, and usually the methods are by researcher's own innovation.^{[94]–[96]} The DIY in soft robotics area can produce highly reliable actuators, including flexible EHD pump technology^[37] and basic DEA technology.^[21] DIY methods are popular because they offer users the freedom to modify and define the parameters during device fabrication. Many open sources and communities exist to support DIY methods. DIY methods have been implemented in other areas such as biotechnology,^[97] biochemistry,^[98] and other topics related to laboratory development.^{[99]–[101]} Reliable DIY for rapid prototyping is essential to accelerate the development and innovation in soft robotics.

The previous chapter discussed a simple method to reliably fabricate stretchable electrodes using the brushing method of CNT powder. The method is straightforward. Briefly, the method begins with the shaping process of the masking sheet. This shaping process determines the shape of the brushed electrodes on the elastomer. The shaping process is completed using a cutting plotter. The next process is to adhere the masking sheet to the surface of the elastomer (in this current research, the elastomer was Sylgard 184). Then the brushing process begins by pouring a small amount of MWCNT powder (MWCNT724769-25G; Sigma-Aldrich) as shown in **Figure 2.4**. The powder MWCNT is brushed manually using a soft brush until the entire surface is fully covered with MWCNT powder. Brushing is in the same direction.

Some researchers have also reported the reliability of these stretchable electrodes.^{[21][22][102]–[104]} Hand brushing CNT on the elastomer is a relatively easy and fast process. As previously discussed in **Chapter 2**, to eliminate the human influence, improve the brushing consistency, and reduce the burden, the brushing process was automated using a brushing machine. Details about the automatic brushing machine are presented in **Chapter 2**. In principle, a low-cost DIY-kit with three-axis machine tools was customized to realize the automatic brushing process. An automatic brushing machine is a convenient technology for future mass

production. Moreover, this type of DIY-kit is available in the marketplace, including Amazon and Monotaro (Japan). This commercial availability of the technology can make fabrication methods easier to reproduce by other researchers.

Besides the automation of the brushing process, this chapter discusses the improvement of the elastomer compatibility towards the fabrication of stretchable strain sensors using an automatic brushing method. The elastomer compatibility and quality were optimized by adding polyethyleneimine (PEIE) to the previously reported pre-polymer of PDMS 30-1.^[21] Adding a small amount of PEIE (approximately 0.11 wt%) increases the stickiness of the elastomer, enhancing the compatibility for the brushing process of the CNT powder.

To examine the effect of powder size on the stretchable strain sensor properties, three conductive powders were accessed: MWCNTs with outer diameters of 6–9 nm (MWCNT-1), MWCNTs with outer diameters of 10–20 nm (MWCNT-2), and MWCNTs with outer diameters of 50–90 nm (MWCNT-3). Then to enhance the compatibility of the sensor for wearable devices, a lamination process was implemented using a thin Ecoflex membrane for the stretchable strain sensor after the brushing process. The Ecoflex membrane can cover the sensor because both the Ecoflex membrane and the sensor display high stretchability mechanical characteristics. A high stretchability can ease material handling of micrometer layers since the Ecoflex membrane does not rip easily during the lamination process. The final stage integrated a stretchable strain sensor with a low-cost microcontroller (Arduino) as the signal processor to detect human hand movement. The hand movement was captured and displayed using virtual software. **Figure 4.1** depicts the overall fabrication sequence of the powder-based stretchable sensor and the wearable device prototype.

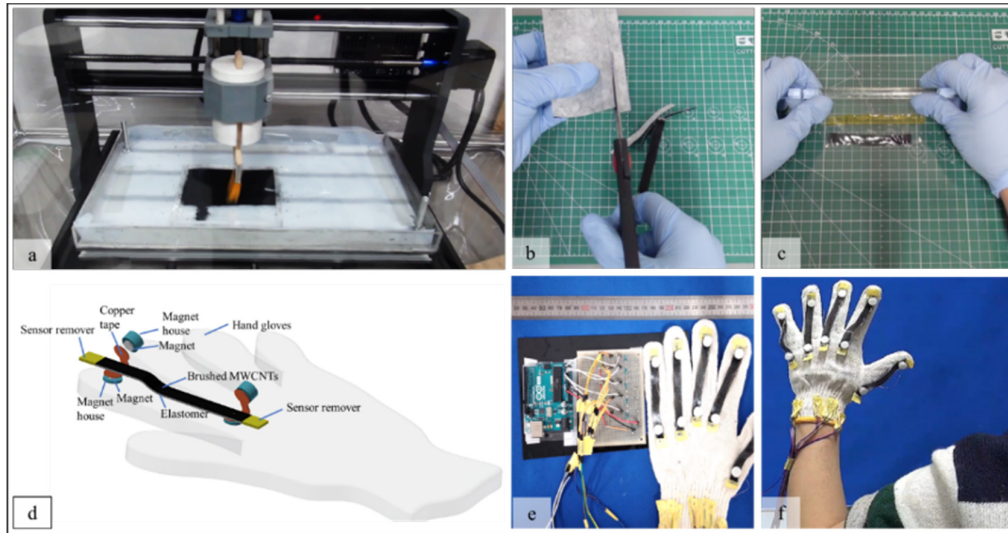


Figure 4.1. DIY-fabrication concept of a stretchable strain sensor and a wearable device prototype. (a) Brushing the CNT powder using a brushing machine, (b) manually shaping the stretchable sensor, and (c) laminating the stretchable strain sensor using a thin Ecoflex membrane. (d) Plug-and-play concept for ease of sensor mounting and maintenance, (e) sensor embedding on a cotton glove and integration system using an economical microcontroller (Arduino), and (f) demonstration of the strain sensor to detect human hand movement. (Adapted from ref. [20] with free distribution permission under the CC-BY License.)

4.2 Mechanical characteristics of the elastomers

A commercial elastomer, Sylgard 184 (Dow), was used to produce a stretchable strain sensor. The elastomer stickiness characteristics should be optimized to strengthen the physical bonding between the elastomer surface and the MWCNT powder. This strong bond reduces the risk of the MWCNT powder detaching from the elastomer surface. Reducing the curing agent part to 3.2 wt% realized a sticky PDMS surface.^[21] To further improve the stickiness characteristics, approximately of 0.11 wt% PEIE^[105] (80% ethoxylated solution by Sigma-Aldrich) was added to the PDMS prepolymer with the 3.2 wt% of the curing agent. Then the liquid solution was pre-mixed manually. The pre-mixed solution was placed into a commercial

mixer (Thinky mixer AR-100) for 3 minutes at a speed of 2000 rpm to ensure a uniform mixture. Finally, PDMS was cured at a temperature of 60 °C for 4 hours.

To evaluate the mechanical characteristics of the elastomer, the PDMS-PEIE was molded to create a sheet with a size of 145 mm × 135 mm × 2 mm. After fully curing the elastomer, a specimen was prepared for a tensile test using a precision dumbbell blade (the size of the dumbbell blade is in accordance with JIS K6251). Then the specimen was tested using Shimadzu AGS-X with a loading speed of 500 mm/min for the uniaxial tensile test. All tensile test data were recorded automatically. For each condition, at least three samples were investigated.

Figure 4.2 depicts the mechanical characteristics of PDMS-PEIE compared to previously reported elastomer, PDMS 30-1, and Ecoflex. Adding PEIE to the PDMS solution changes the mechanical characteristics of the elastomer. This change should be due to the crosslinking characteristics formed on the elastomer.^[106] The addition of the PEIE in the elastomer solution realizes an approximately 50% (PDMS-PEIE) more stretchable elastomer compared to the previously reported PDMS with a 3.2 wt% curing agent and without PEIE (PDMS 30-1). This strain improvement of the PDMS-PEIE is attributed to the heterogeneously crosslinked elastomer network.^[106]

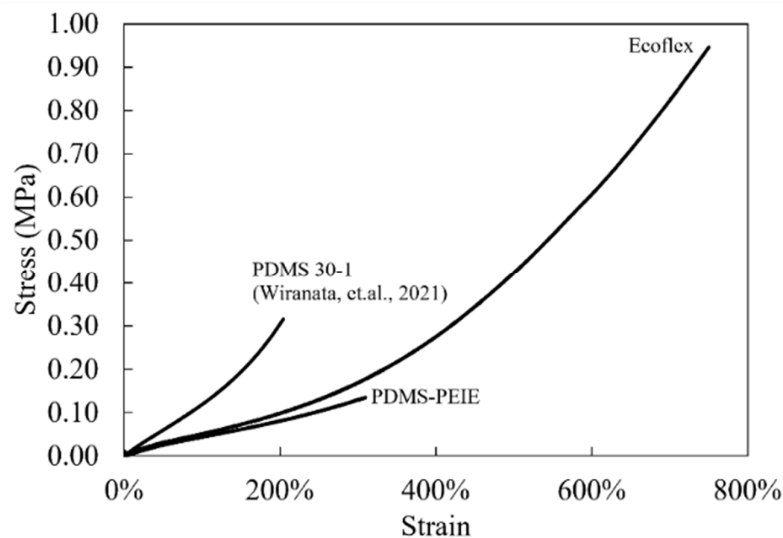


Figure 4.2. Mechanical characteristics (engineering stress-strain) of the elastomer. (Adapted from ref. ^[20] with free distribution permission under the CC-BY License.)

A tacky elastomer surface is necessary when using a powder-type electrode. Additionally, an adaptable and viscous surface increases the physical bonding between powder-type electrodes and the elastomer surface. In this research, the surface adhesivity was investigated using previously suggested methods of ASTM D 6195 03. All size and experimental conditions were similar to the previously described experimental condition in **Chapter 3**. Briefly, the fabrication of the test specimen started by creating a 0.5 mm × 25 mm × 175 mm PDMS strip using a simple molding method. **Figure 4.3** shows the molding shape for the loop tack test. The molding method required a 3-mm acrylic plate as a base and 0.5-mm acrylic as a mold shaper. Then a square hole with an area of 25 mm × 175 mm was created on the 0.5-mm acrylic. The final step of the molding fabrication process was to adhere this pre-holed 0.5-mm acrylic to the base 3-mm acrylic plate using acrylic adhesive. Then the molding method of elastomer began by pouring the elastomer solution onto the mold and putting it into an oven for 4 hours at 60 °C. After fully curing the material, the elastomer was peeled from the mold, and the specimen was ready for the loop tack test.

The loop tack test was similar to the method previously discussed in **Chapter 3**. Briefly, after peeling off the material, then the elastomer was bent upon itself to form a teardrop-shaped loop. Next, the ends of the loop were connected using masking or regular tape. The loop was gripped by a tensile tester. Then the teardrop shape was brought into contact with a polished stainless-steel surface to form a 25 mm × 25 mm contact area. Finally, the tensile tester pulled the test specimen with a speed of 300 mm/min until the elastomer fully detached from the stainless-steel surface. Details of the tackiness test are reported elsewhere by Wiranata et al.^[21]

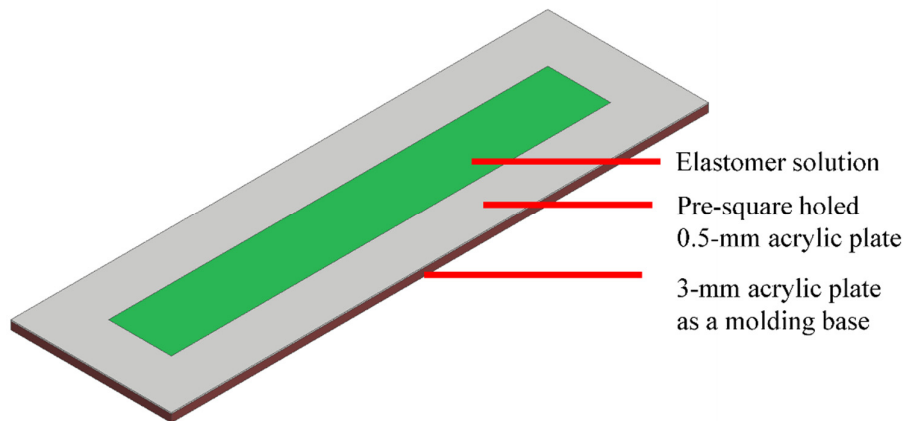


Figure 4.3. Molding shape for the loop tack test of the elastomer. (Adapted from ref. ^[20] with free distribution permission under the CC-BY License.)

Figure 4.4 shows that adding a small amount of PEIE into the mixing solution of PDMS improves the elastomer stickiness. For example, adding a small amount of PEIE (approximately 0.11 wt%) realizes PDMS with an approximately 63% higher tackiness than the previously developed PDMS30-1(**Figure 4.4**).^[21] The high stickiness characteristics of this elastomer may be due to the viscous surface adaptation of the PDMS, which allows van der Waals interactions with another substrate surface.^[106] Moreover, the surface adaptability of the elastomer enhances the surface contact area between the elastomer and substrate, which further strengthens the bonding between the elastomer surface and the substrate.

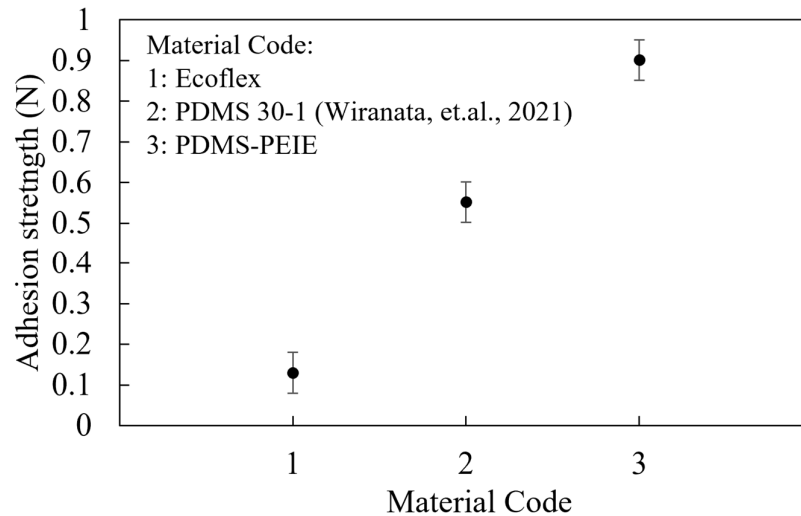


Figure 4.4. Tackiness of the elastomer surface. (Adapted from ref. ^[20] with free distribution permission under the CC-BY License.)

4.3 Stretchable sensor surface conditions

PDMS-PEIE was used as the main elastomer to create a stretchable sensor. The PDMS-PEIE sheet size was approximately 100 mm × 100 mm × 0.5 mm. A simple coating process was employed to create a 0.5-mm-thick PDMS-PEIE membrane. Then PDMS PEIE was attached to a 100 mm × 100 mm acrylic frame (**Figure 2.6**). An acrylic frame can ease material handling when a brushing method is applied (**Figure 2.6**). Afterward, the MWCNT powder was brushed onto the PDMS PEIE using the developed automatic brushing machine described in **Chapter 2 (Figure 2.6)**. To investigate the effect of CNT powder type on the stretchable strain sensor performance, three different sizes of MWCNTs were examined: MWCNTs 724769-25G from Sigma-Aldrich with an outer diameter of 6–9 nm and length of 5 μm (MWCNT-1), MWCNTs 0553CA from Sky Spring Nanomaterial with an outer diameter of 10–20 nm and length of 5–30 μm (MWCNT-2), and MWCNTs 901019-25G from Sigma-Aldrich with an outer diameter of 50–90 nm and length of 15 μm (MWCNT-3).

After the brushing process, the brushed PDMS-PEIE was shaped into a 10-mm-wide strip by manually cutting the sheet (**Figure 4.5**). To ease the sensor shaping

process, the brushed PDMS-PEIE with an acrylic frame was placed on the masking paper with the brushed surface facing upward prior to removing the acrylic frame (**Figure 4.5a**). Then PDMS-PEIE was cut using a scalpel (**Figure 4.5b**) to form a square brushed PDMS-PEIE sheet without a frame (**Figure 4.5c**). The sheet was subsequently flipped backward and placed on a soft surface (e.g., tissue paper) (**Figure 4.5d**). Afterward lines were drawn on the masking paper with a 10-mm gap between each line (**Figure 4.5e**). The final step was to cut the strip according to the pattern. **Figure 4.5g** shows the final product of the stretchable strain sensor. **Figure 4.5h** shows the stretchable strain sensor in the unstretched and stretched states.

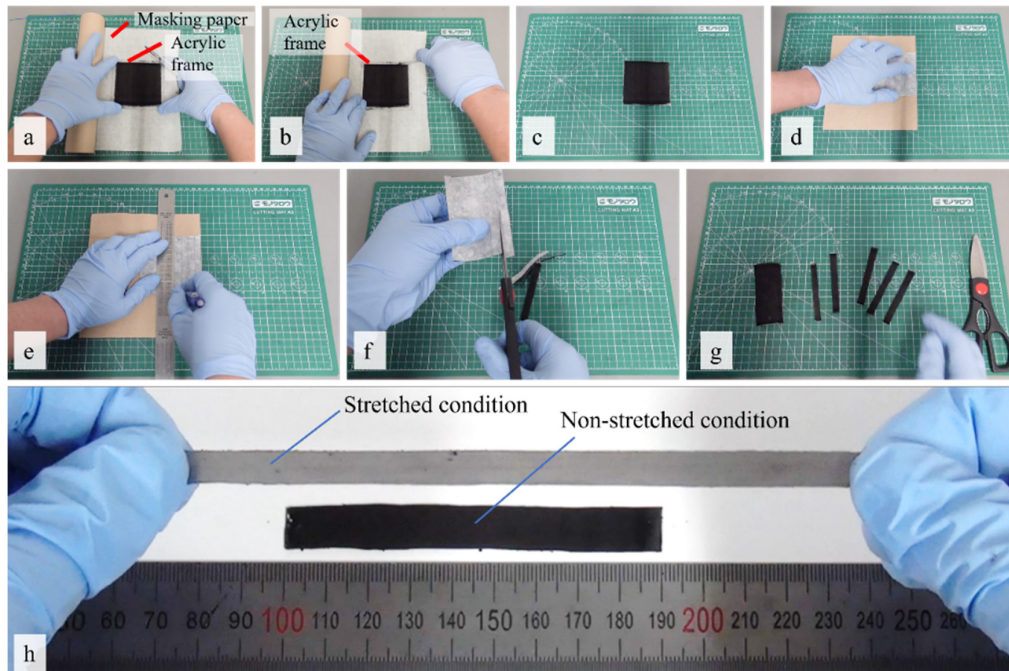


Figure 4.5. Shaping process of the stretchable strain sensor. (Adapted from ref. ^[20] with free distribution permission under the CC-BY License.)

Then the surface condition of the stretchable strain sensor was examined using FE-SEM. **Figures 4.6a–a2** show the surface condition of PDMS-PEIE/MWCNT-1. Agglomerates of several MWCNTs appear on the micrometer scale (**Figure 4.6a**). The agglomerates may affect the sensor quality. There is a high possibility that smaller agglomerates produce less noise in the sensor reading when the sensor is at

a higher strain (e.g., 100% strain). Magnified images on the nanometer scale show that the MWCNT-1 are spread uniformly on the surface of the PDMS-PEIE (**Figures 4.6a1 and a2**). This uniform dispersion pattern should enhance the network connection between MWCNT particles.

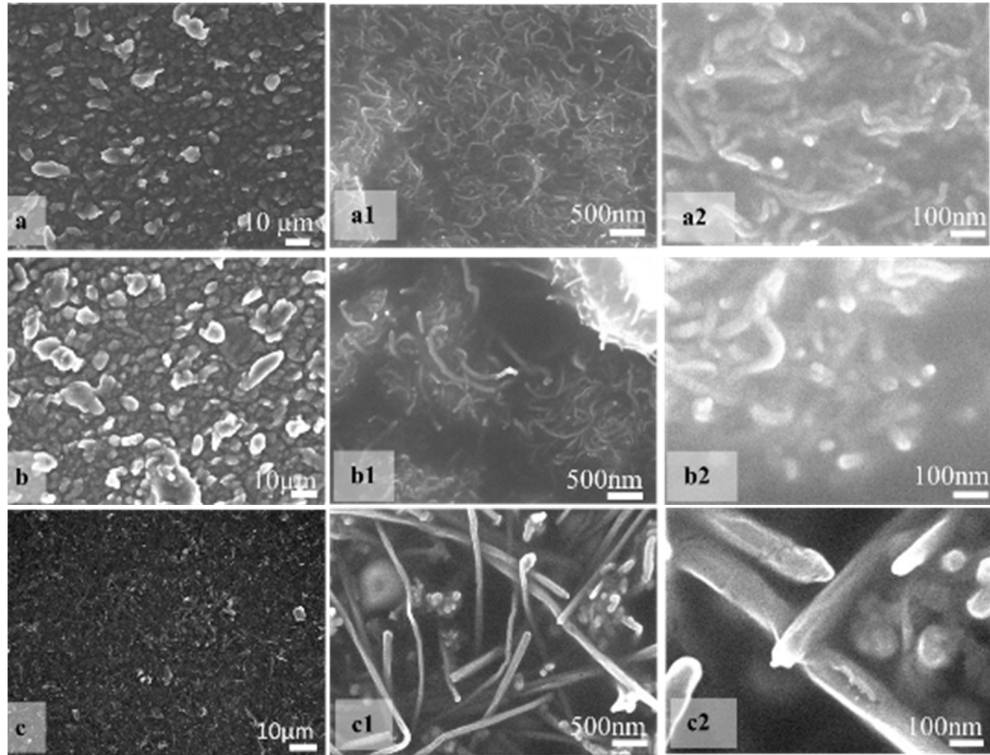


Figure 4.6. FE-SEM images show the surface morphology of (a–a2) PDMS-PEIE/MWCNT-1, (b–b2) PDMS-PEIE/MWCNT-2, and (c–c2) PDMS-PEIE/MWCNT-3 at different magnifications (micrometer to nanometer size). (Adapted from ref. ^[20] with free distribution permission under the CC-BY License.)

A similar pattern is also observed in MWCNT-3, which has a larger particle size (**Figures 4.6c1 and c2**). Additionally, it shows a uniform pattern (**Figures 4.6a1 and a2**). This uniform pattern on the nanometer and micrometer scales (**Figure 4.6c**) lowers the noise reading of the strain sensor. Furthermore, the structure of MWCNT-3 (**Figure 4.6c1**) looks stiffer than the other MWCNTs. **Figure 4.6c1** indicates a less dense MWCNT network structure, which causes a problem when the strain sensor is under high strain conditions (e.g., degradation of the sensor sensitivity). In the case

of PDMS-PEIE/MWCNT-2, **Figures 4.6b1 and b2** show black blank spaces and other areas full of the MWCNT network, which resemble the valleys and peaks on the surface of PDMS-PEIE/MWCNT-2 respectively. This surface pattern of PDMS-PEIE/MWCNT-2 makes the strain sensor more sensitive since the valleys and peaks can shift easily and collide with each other when the sensor size changes due to the strain effect. Compared to the PDMS-PEIE/MWCNT-1 surface (**Figure 4.6a**), the PDMS-PEIE/MWCNT-2 surface (**Figure 4.6b**) has larger agglomerates, which can stimulate noise in the reading when the sensor operates at a higher strain.

4.4 Electromechanical characteristics of stretchable electrodes

4.4.1 Electromechanical tensile test equipment for stretchable conductive materials

As discussed in the chapter above, soft robotics has received increased attention in different fields due to potential applications such as wearable devices,^{[16][107][108]} biomedical,^{[109]–[111]} healthcare,^{[105][112][113]} and other human soft machine interfaces. Fundamental research has been conducted to support advances in soft robotics. For example, studies on soft actuators (e.g., DEAs,^{[21][22][103][114]} soft electroadhesion,^{[68]–[71]} and stretchable pumps^{[29][37][72]}) have provided a basic understanding of their characteristics. The primary strategy for developing soft robotics involves innovation in soft materials engineering, including material synthesis, fabrication, and mechanical design.^[115] However, a major hurdle is that the whole body, including the electric circuit, must be bendable, twistable, and stretchable. Consequently, conductive and stretchable materials are crucial.

As the interest in soft robotics grows, the demand for flexible conductive materials has increased. Consequently, researchers strive to realize easy, fast, and cost-effective fabrication methods for flexible conductive materials. For example, stretchable sensors have been formed using carbon black (CB) mixed with Ecoflex,^[2] 3D printing,^[12] and ionic liquids for human motion monitoring.^[116] When fabricating stretchable sensors, multiple areas must be considered: mechanical compliance, mechanical characteristics, and electric conductivity of the materials. Conductive

materials that do not undergo physical changes or damage under cyclic tensile and high strain conditions should exhibit a high performance.

To investigate these characteristics, special equipment for stretchable sensor tests should be established. Several methods have been employed to assess the quality of stretchable conductive materials. These include mechanical testing, electrical properties testing, and physical inspection. Physical inspections elucidate how a stretchable material can be conductive. For example, DEAs can be fabricated by brushing CNT powders since the brushing process builds a strong CNT network connection.^[21] This strong network connection can be inspected via physical inspections. Researchers use commercially available field emission scanning electron microscopes to understand how brushing affects the DEA quality. This physical inspection is performed easily since the equipment is available commercially. In contrast, testing the mechanical and electrical properties of stretchable conductive materials is more challenging because combined equipment that simultaneously measures the mechanical and electrical properties (electromechanical test) is not widely available in the marketplace. This situation has hindered the development of soft and stretchable conductive materials.

Previous studies have implicitly used an electromechanical equipment test to check the quality and characteristics of stretchable sensors.^{[2] [21]} For example, a CB-Ecoflex conductive material was examined using a motorized stage combined with an LCR meter,^[2] where the equipment was controlled through LabView to evaluate the electromechanical properties of the stretchable sensor. Another example is the development of stretchable sensors using brushing methods for DEAs.^[21] A tensile tester machine synchronized with an LCR meter was used to assess the condition of stretchable conductive materials. Both studies focused on physical phenomena of soft sensors and actuators. However, neither provided details about the electromechanical equipment, equipment synchronization, or codes for device synchronization.

This subchapter develops a customized electromechanical tensile test for soft and stretchable materials. Three standalone devices were integrated using Python software. This subchapter also provides a graphic user interface (GUI) for easy

operation of the equipment. The priority was to provide clear steps and methods to setup electromechanical tensile test equipment for soft stretchable conductive materials. Python-based software was selected because all researchers can access the software and modify it to meet their research requirements. This study should assist in the development of laboratory equipment and research. This customized electromechanical tensile test is expected to contribute to advances in soft robotics, especially soft and stretchable sensors. Furthermore, this electromechanical setup can aid in the development of education about soft robotics and enhance the understanding of the electromechanical properties of stretchable conductive materials.

The described equipment in this subchapter integrates a mechanical tensile test with an electrical property test. The equipment is composed of three modules: a linear stage and controller, an LCR meter, and a customized weight scale. These modules are integrated using a Python GUI interface for operation ease. **Figure 4.7** depicts the overall electromechanical tensile test device integration. **Figure 4.7a** describes the controller and data acquisition part, while **Figure 4.7b** shows the testing condition part. In general, the device is composed of three modules (tensile tester module, electrical tester module, and GUI). Details of each module are described below.

4.4.1.1 Tensile tester module

The tensile tester module consisted of a linear stage controller by Optosigma HSC-103 (**Figure 4.7a1**), linear stage OSMS-26-300ZSGSP by Optosigma (**Figure 4.7b1**), manual adjustable X-Y jig by Optosigma (**Figure 4.7b7**), a loadcell with a maximum load of 5 kg by Uxcell (**Figure 4.7b3**) controlled by a HX711 module with Arduino-Nano (**Figure 4.7a3**), and 3D-printed material gripper (**Figures 4.7b4 and b6**). The linear stage and the controller part were used without any modifications. An X-Y adjustable jig by Optosigma was purchased separately and easily adjusted the bottom part of the gripper in the x- and y-direction. A

commercially available loadcell module with Arduino-Nano was employed to integrate all of the devices with the GUI since Arduino-Nano can be controlled using serial communication.

The trickiest part in this module was designing the gripper (**Figures 4.7b4 and b6**). The gripper part should accommodate the material gripper and the conductive probe to monitor the resistance change in the material. Herein the gripper was designed for resistance monitoring. **Figure 4.8** shows the material gripper part. The hole in **Figure 4.8a** was used to mount the HIOKI magnetic probe. A magnetic holder was used to secure the connection between the magnetic probe and the conductive material (**Figures 4.7b and 4.8b**). Compared to other commercialized tensile test machines, the price of this device is reasonable and supports fully customized device arrangements for a specific purpose.

4.4.1.2 Electrical tester module

The electrical tester module consisted of an LCR meter HIOKI 3536 (**Figure 4.7a4**) and a magnetic probe HIOKI 9804 (**Figure 4.7b5**). For an electromechanical test, the magnetic probe was inserted in the gripper mount (**Figure 4.8a**). The LCR meter had a universal serial bus (USB) serial support for communications between the LCR meter and a personal computer (PC), allowing the equipment to be controlled using simple Python code.

4.4.1.3 GUI of the tensile tester

In this study, the GUI helped researchers conduct the experiment by easily defining the appropriate variable. The GUI was created using a Python platform. **Figure 4.9** shows the overall GUI when a measurement is in progress. As this is open-source software, researchers can easily access and develop it according to their research objective. The chart monitoring side in this GUI shows information such as resistance, voltage, current, displacement of the linear stage, and tension. In this GUI,

the tension and the displacement are in grams and millimeters, respectively. The strain and tensile strength can be manually converted from the raw data using spreadsheet software.

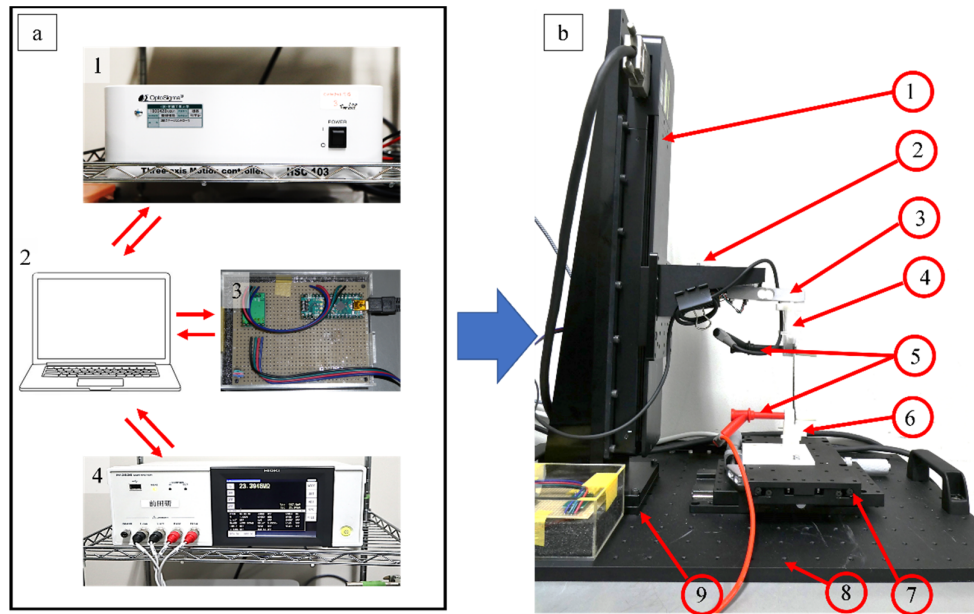


Figure 4.7. Electromechanical tensile test equipment. (a) Controller and data acquisition part, and (b) testing part. (Adapted from ref.^[117] with free distribution permission under the CC-BY License.)

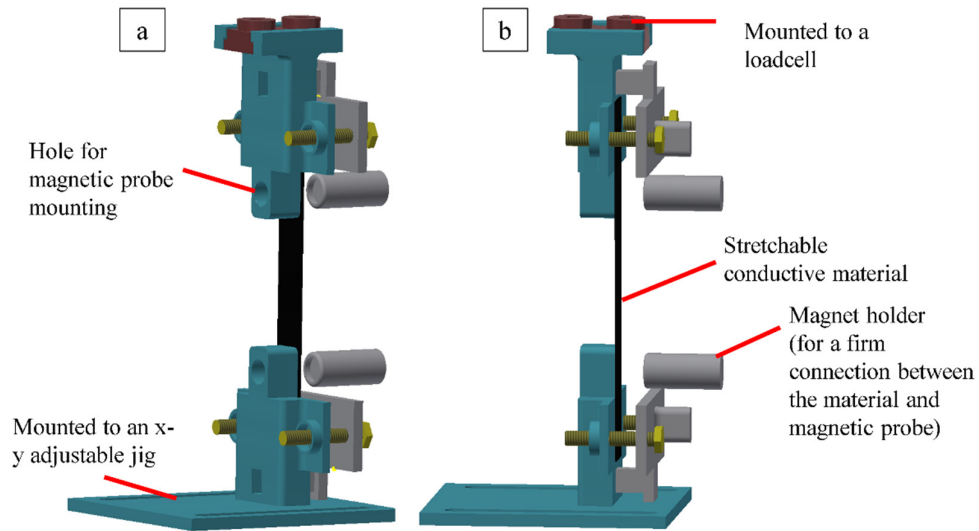


Figure 4.8. Material gripper for the electromechanical tensile test equipment. (Adapted from ref.^[117] with free distribution permission under the CC-BY License.)

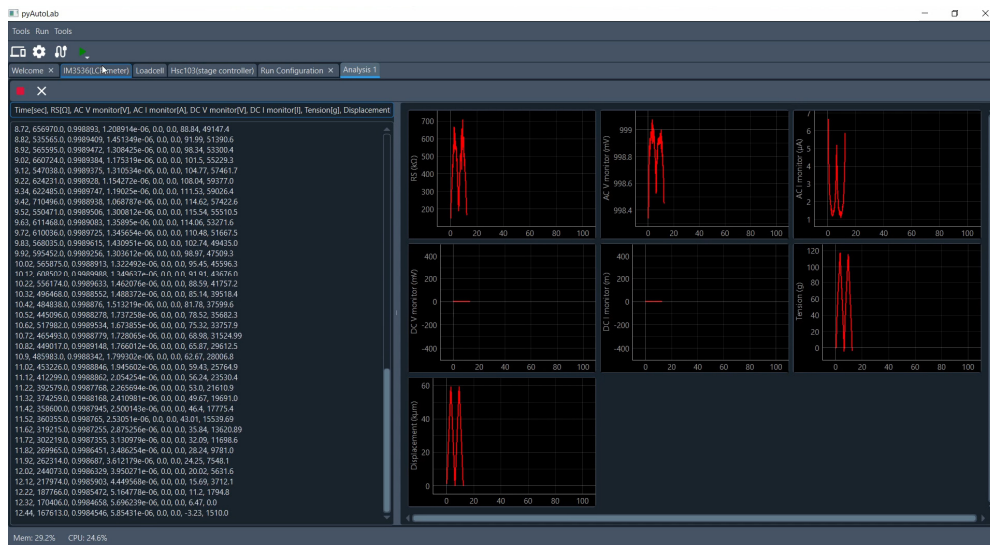


Figure 4.9. GUI of the tensile test equipment. (Adapted from ref.^[117] with free distribution permission under the CC-BY License.)

The goal of this system integration is to measure the mechanical and electrical properties simultaneously. This experimental setup may contribute to the development of soft and stretchable conductive materials for soft sensors, soft actuators, and soft electric circuits. Our device integration approach is useful for researchers interested in the following subjects:

- a. Flexible electronics: Electric circuits must be composed of flexible materials, which are conductive even under high strain conditions. This electromechanical tensile test can help elucidate the basic qualities of stretchable conductive materials under strained conditions.
- b. Soft robotics: High-performance stretchable sensors are necessary to provide an interface between human and soft robotics. In addition, this electromechanical testing device may help researchers understand the basic performance characteristics of stretchable sensors.
- c. Soft materials engineering: The tensile test equipment can perform electrical and mechanical tests simultaneously. This equipment is suitable for soft material tensile tests. This device can also help characterize polymers or rubbers (cyclic and one-time tensile tests).
- d. Customized laboratory experiments: The different components are available commercially and sold separately. Any researcher can setup this tensile testing equipment. The price is reasonable compared to other professional packs of tensile tester machines. Moreover, the equipment can be customized and arranged based on the user's requirements.

Table 4.1 and 4.2 list the design summary and the bill of materials, respectively. These detailed accounts should guide researchers who want to build or upgrade their experimental equipment for soft robotics research.

Table 4.1. Design file name and summary. (Adapted from ref.^[117] with free distribution permission under the CC-BY License.)

Design file name	File type	Location of the file
Gripper (magnetic holder, upper side, and bottom side)	CAD files	(Folder: Gripper 3D file) http://dx.doi.org/10.17632/rckgk7gz5m.1
Python GUI software interface	Python program files	(Folder: Software GUI (python software)) http://dx.doi.org/10.17632/rckgk7gz5m.1
Arduino Program for loadcell	Arduino program	(Folder: Loadcell-Arduino Software) http://dx.doi.org/10.17632/rckgk7gz5m.1
Equipment Installation process	Word file	(Folder: Driver list) http://dx.doi.org/10.17632/rckgk7gz5m.1
GUI software setting movie (Movie S1)		(Folder: Movie S1) http://dx.doi.org/10.17632/rckgk7gz5m.1

Table 4.2. Cost of the materials. (Adapted from ref.^[117] with free distribution permission under the CC-BY License.)

Designator	Component	Number	Cost per unit* - currency	Total cost - Currency	Source of materials	Material type
Linear stage (Fig. 1 B1)	OSMS-26-300(Z) SGSP	1	\$1,765	\$1,765	https://jp.optosigma.com/	Metal
Linear stage controller (Fig. 1 A1)	HSC-103	1	\$2,621	\$2,621	https://jp.optosigma.com/	Metal
Arduino-Nano (Fig. 1 A3)	Arduino-Nano	1	\$25	\$25	https://www.amazon.co.jp/	Electronics
LCR meter (Fig. 1 A4)	IM3536	1	\$4,194	\$4,194	https://www.hioki.com	Electronics
Z bracket (Fig. 1 B2)	ZBR-8060	1	\$34	\$34	https://jp.optosigma.com/	Metal
Loadcell 5kg and HX711 from Uxcell (Fig. 1 B3)	Loadcell & HX711	1	\$12	\$12	https://www.amazon.co.jp/	Metal and Electronics
Gripper (Figs. 1 B4 and B6)	magnetic holder, upper side, and bottom side	1	\$3	\$3	3Dprinted part	Polylactic acid (PLA) (3D printed material)
Magnetic probe (Fig. 1 B5)	HIOKI 9804	1	\$58	\$58	https://www.amazon.co.jp/	Metal and plastic
X-Y jig (Fig. 1 B7)	TSD-10162SR	1	\$1,310	\$1,310	https://jp.optosigma.com/	Metal
Breadboard (Fig. 1 B8)	OBC-4545	1	\$282	\$282	https://jp.optosigma.com/	Metal
Conversion spacer (Fig. 1 B9)	SP-102-2	1	\$9	\$9	https://jp.optosigma.com/	Metal

*Cost per unit of the equipment was checked in 2021

4.4.1.4 Build instructions

The assembly process of the tensile test equipment requires the following parts: linear stage, linear stage controller, Z bracket, breadboard, conversion spacer, X-Y jig, and 3D printed gripper. All parts were purchased and used without modifications.

The gripping part for soft material tensile testing was designed using an Autodesk Inventor for students and printed using a 3D printer (3D raise Pro 2).

Since all parts were used as received, the assembly process is straightforward with the following steps. First, bolt the conversion spacer onto the breadboard. Second, bolt the linear stage onto the conversion spacer. Third, bolt the X-Y jig onto the breadboard exactly in front of the linear stage (**Figure 4.7b**). Fourth, place the Z bracket onto the linear stage at the moving stage. At this point, our tensile tester is almost ready. To complete the equipment, bolt the loadcell to the Z bracket. Finally install the upper gripper on the loadcell and the lower gripper on the X-Y jig. Now the tensile tester part is complete.

To control the tensile tester part and acquire data for both tensile displacement and tensile strength, connect the linear stage to the linear stage controller (HSC-103). Then connect HSC-103 to a PC via a USB port. Now, the linear stage can be controlled using our Python GUI (**Figure 4.9**).

Next, activate the loadcell reading by connecting the loadcell with HX711 and HX711 with Arduino-Nano. This loadcell module is a DIY kit, which is already supported by the Arduino library. Hence, installation is straightforward. First, connect the loadcell wire to HX711 with the connection chart in **Table 4.3**. Then connect HX711 to Arduino-Nano according to **Table 4.3**. To acquire tensile strength data, connect Arduino-Nano to a personal computer, and read the data using our Python GUI. This completes the tensile tester assembly.

To acquire electrical data, insert the magnetic probe (HIOKI 9804) into the hole provided in the upper and bottom sides of the 3D-printed gripper. The magnetic probe should be aligned with the gripper surface. Next, connect the magnetic probe to the LCR meter. Connect the LCR meter to the computer. This completes the electromechanical tensile tester assembly. Finally, connect Arduino-Nano, LCR meter, and linear stage controller to the computer and launch the provided Python GUI to control and read the data. **Figure 4.7** shows the final equipment arrangement.

Table 4.3. Connection chart of the loadcell module. (Adapted from ref.^[117] with free distribution permission under the CC-BY License.)

Load cell to HX711	
Loadcell side (Cable color)	HX711 (Pin name)
Red	E+
Black	E-
White	A-
Green	A+
HX711 to Arduino-Nano	
HX711 (Pin name)	Arduino-Nano (Pin name)
GND	GND
DT	A1
SCK	A0
VCC	5V

4.4.1.5 Operation instructions

The provided Python GUI can control the above assembly. First, install the required drivers provided by the company of each part. The detailed process on the driver installation is available in the following repository as shown in **Table 4.1** (Driver List). Next, install the loadcell module. The loadcell module is an Arduino-based module, which makes installation straightforward. Briefly, installation of the loadcell module begins by installing the Arduino ide software and the HX711 library. Afterwards, upload the provided program to the Arduino board. Details about the software upload and installation of the Arduino program are available in the repository in **Table 4.1** (Driver List folder and the Arduino program for loadcell provided in the Loadcell-Arduino Software folder).

After the installation process is complete, control can be realized from our Python GUI. Our Python GUI sends the commands provided by the vendor of each part. In the LCR meter, the vendor provides command codes to acquire the data and for HSC-103. In the case of the loadcell module, the command was created using simple C programming language since the program to read the load cell is straightforward. In the loadcell module, command codes “a” and “b” are used for data reading and tare scaling, respectively. Then equipment control begins by installing the necessary Python libraries as mentioned in the repository in **Table 4.1** (folder name is Software GUI (python software)). After installing the essential Python library, the GUI is started by running the start.py file (all program instructions are in the repository in **Table 4.1** (folder name is Software GUI (python software))).

After opening the program, the connection ports must be set (**Figure 4.10**). Choose the port for the LCR meter, HSC 103, and loadcell module. Then click connect to each tab and close this step. The GUI provides control for two linear stage controllers: HSC 103 and SHOT 702. These two controllers are also compatible with OSMS 26 300(Z). Thus, SHOT 702 or HSC 103 can be used to control OSMS 26 300(Z).

Figure 4.11 shows the equipment setting tab, starting from the LCR meter (**Figure 4.11a**), loadcell (**Figure 4.11b**), and linear stage controller tab (**Figure 4.11c**). In the LCR meter tab, any variable can be selected. Start from resistance or any other variable such as capacitance or impedance. Four variables can be chosen simultaneously by selecting 4 in the dropdown menu. The loadcell tab is simple since it can include or exclude the equipment by checking or unchecking the appropriate box to enable or disable a device, respectively. The fix zero button is used to tare the scale (i.e., set the current weight as a reference). Then at the linear stage tab, set the zero position of the linear stage by clicking the red circled button, and a new window will appear (**Figure 4.11c**). The position can be adjusted. Then click zero to set the current position to zero, and decide whether the testing method is one step, many stepping modes of a one-time tensile test, or a cyclic tensile test. Next, determine the maximum displacement of the tensile test and the number of cycles (if it is a cyclic

test). If there is an interval between cycles, add this parameter. Furthermore, set the pulling speed of the tensile tester.

The next step is to navigate to the welcome tab again (without closing any of the tabs). Click the “open run configuration” (**Figure 4.12**). In the run configuration, define the location to save the raw data, the measuring interval, and whether to show the graphic in real-time. Once these settings are determined, navigate to the welcome tab again. Click final step number four (**Figure 4.10**) to start controlling the device or click the green triangle-shaped button at the menu bar. (**Movie S1** shows the detailed setup process. **Movie S1** link is available in the repository in **Table 1**.)

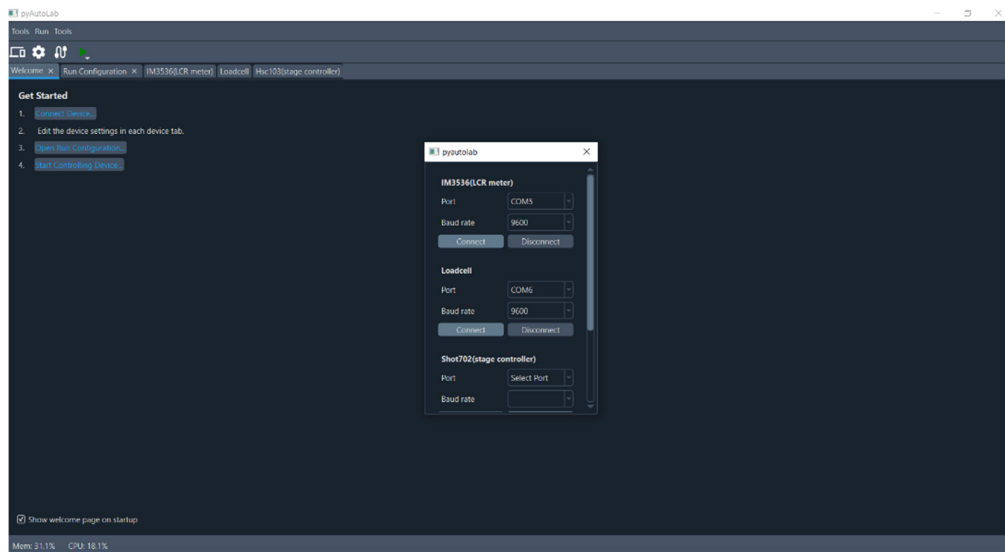


Figure 4.10. Home screen of the electromechanical device GUI control. (Adapted from ref.^[117] with free distribution permission under the CC-BY License.)

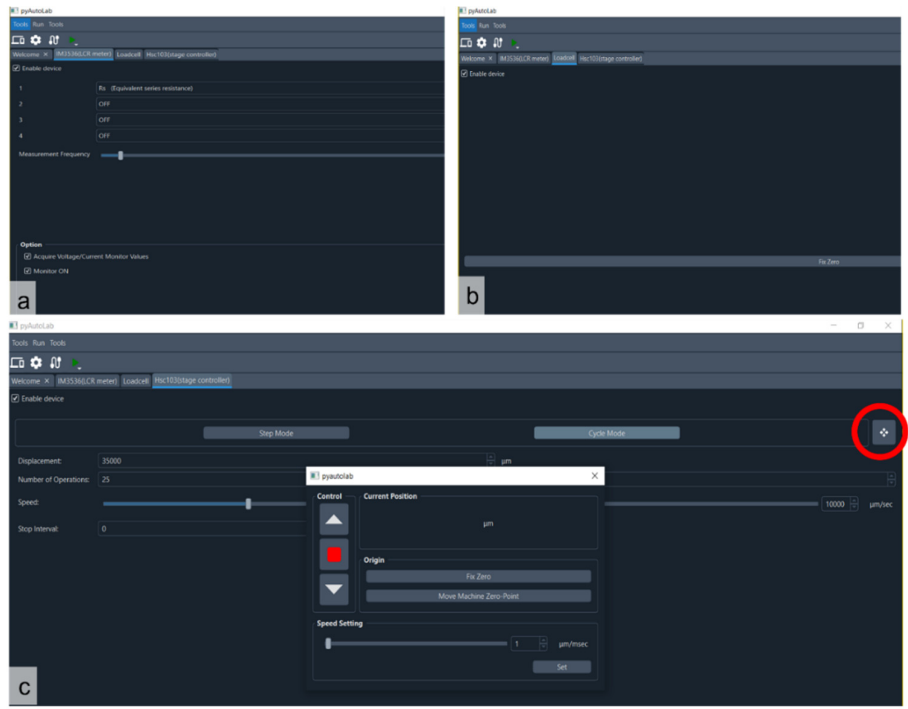


Figure 4.11. Variable setup for testing equipment. (a) LCR meter tab, (b) loadcell tab, and (c) linear stage control tab. (Adapted from ref.^[117] with free distribution permission under the CC-BY License.)

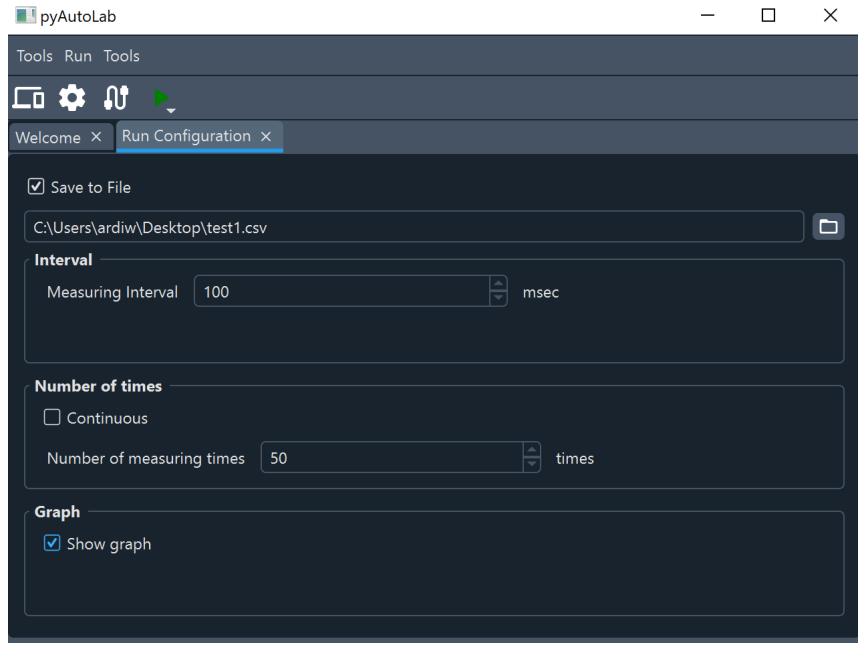


Figure 4.12. Run configuration option. (Adapted from ref.^[117] with free distribution permission under the CC-BY License.)

4.4.1.6 Remarks about the usage of the electromechanical tensile test

This equipment was tested using hundreds of cyclic tests of stretchable conductive elastomers. The most stable operation settings are achieved with a measuring interval of 100 ms (around 10 Hz of data transfer). The equipment was also tested at different tensile speeds, ranging from 10–30 mm/s. The measurement process is stable. In conclusion, this subchapter integrates equipment to test the electrical and mechanical properties. Simultaneously testing the mechanical and electrical properties should elucidate the essential characteristics of stretchable conductive materials. Although our equipment is designed specifically for soft materials, it could be used for hard materials such as PVC, carbon composites, or nylon by modifying the gripping part. Additionally, our equipment has the potential to measure the properties of touch and pressure sensors by modifying the gripping part. Changing the linear stage controller from HSC-103 to SHOT 702 should reduce the overall price since SHOT 702 is \$1000 cheaper than HSC103. We expect that our equipment will contribute to the development of soft robotics, especially soft and stretchable sensors.

4.4.2 Electromechanical tensile test results and discussion

The electrical properties of stretchable electrodes (e.g., resistance and capacitance) depend on the geometric change of the stretchable electrodes. In the previous **chapter 3**, a stretchable electrode was used to build DEAs. In the case of DEAs, the device works by converting electric energy into mechanical works. To use stretchable electrodes as dielectric sensors, the working principle is the opposite of that for DEAs. In the sensor case, an external force is exerted to the device. This external force leads to a change of geometry of the sensor, which also triggers a change in the electrical property of the sensors. The change in the electrical property in the stretchable electrodes facilitates the measurement of strain either through the capacitance or resistance change. For a capacitance type sensor (**Figure 4.13**), the device works when there is an external force toward the device. Due to the uniaxial

stress, as shown in **Figure 4.13a**, the stretchable electrode and the elastomer of the device are compressed.

Suppose that the elastomer and the stretchable electrodes are incompressible during the compressed state. Then the elastomer deforms in the thickness direction, and the surface of the elastomer becomes larger, leading to a change in the capacitance value of the device. The response of this capacitive-type dielectric elastomer sensor to vibrations has previously been investigated.^[118] The ratio between the change in the capacitance value to the deformation of the device is expressed as GF.

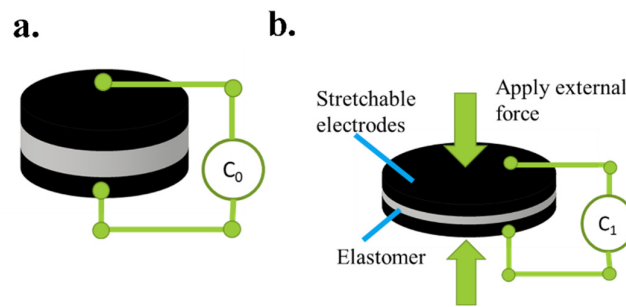


Figure 4.13. Capacitance-type sensor mechanism for the (a) initial condition and (b) deformed condition.

In the case of a resistance-type sensor, the working principle is almost the same as that of the capacitance-type sensor. The resistance-type sensor is commonly used to detect the elongation. Briefly, when the resistance-type sensor is under a uniaxial tensile stress, the electrodes and the elastomer are elongated (**Figure 4.14** shows the conditions of the resistance-type sensor under the initial and elongated states). This elongated state leads to a change in the resistance. To compare the quality between different sensors, researchers use GF. GF in resistance-type sensors is similar to that in capacitance-type sensors. In the resistance-type sensor, GF is also the ratio between the change in resistance to the strain of the materials. Ideally, a resistance-

type sensor should have a high linearity for GF. Hence, a high GF means that the sensor has a high sensitivity to the change in its geometry.

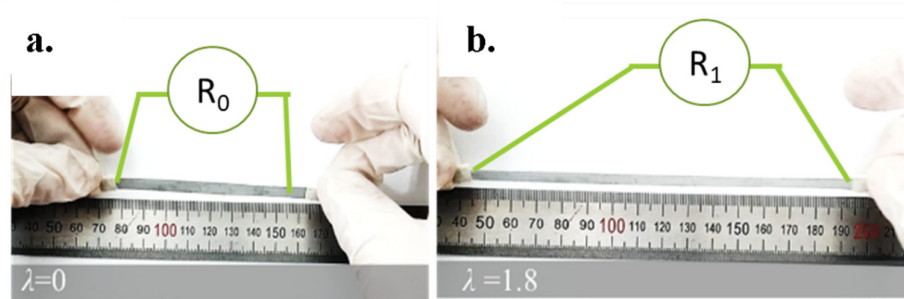


Figure 4.14. Resistance-type sensor mechanism for the (a) initial and (b) elongated conditions.

Based on the mechanism described above, resistance-type sensors can easily be fabricated using PDMS-PEIE/MWCNT-1, PDMS-PEIE/MWCNT-2, and PDMS-PEIE/MWCNT-3. These types of stretchable electrodes are suitable to test the change of resistance. The electromechanical tensile test equipment was used to check the electromechanical characteristics of the stretchable sensor of PDMS-PEIE/MWCNT-1, PDMS-PEIE/MWCNT-2, and PDMS-PEIE/MWCNT-3. **Figure 4.15** describes the characteristics of the stretchable strain sensors fabricated using PDMS-PEIE. The stretchable strain sensor reading converges from the 2nd cycle to the 50th cycle (**Figures 4.15a, b, and c**). PDMS-PEIE/MWCNT-1 has the most stable readings at different tensile speeds (**Figure 4.15a**). GF of the PDMS-PEIE/MWCNT-1 stretchable strain sensor remains nearly constant even when the pulling speed increases (**Figure 4.15d**). The PDMS-PEIE/MWCNT-1 stretchable sensor shows less noise than the PDMS-PEIE/MWCNT-2 stretchable strain sensor at a tensile speed of 7 mm/s (**Figure 4.15a**). (**Figure 4.16** provides more details about the PDMS-PEIE/MWCNT-2 stretchable sensor at a tensile speed of 7 mm/s). The PDMS-PEIE/MWCNT-1 stretchable sensor can be stretched up to 100% strain, and the reading result shows less noise (**Figure 4.17a**) than PDMS-PEIE/MWCNT-2.

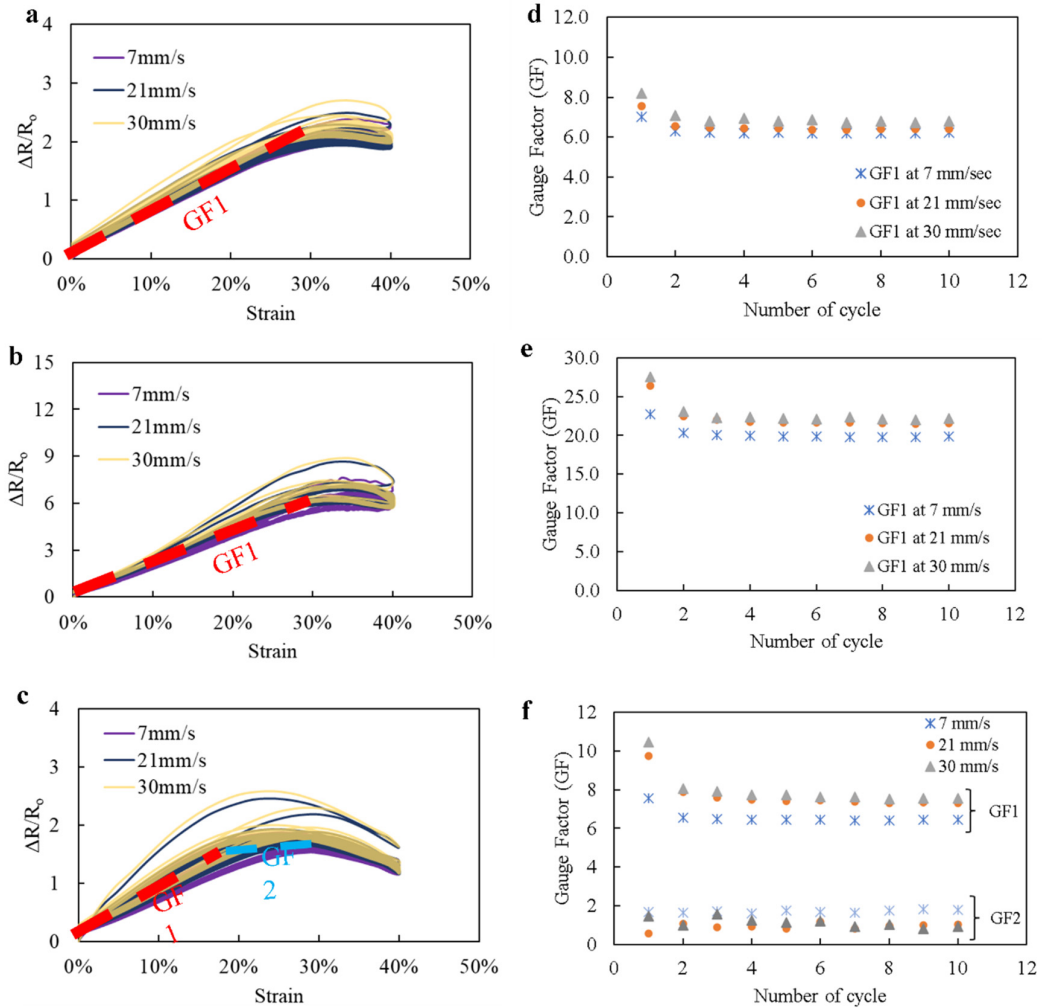


Figure 4.15. Electromechanical characteristics of the stretchable strain sensors: (a) PDMS-PEIE/MWCNT-1, (b) PDMS-PEIE/MWCNT-2 and (c) PDMS-PEIE/MWCNT-3. Gauge factors (GFs) of (d) PDMS-PEIE/MWCNT-1, (e) PDMS-PEIE/MWCNT-2, and (f) PDMS-PEIE/MWCNT-3. (Adapted from ref. [20] with free distribution permission under the CC-BY License.)

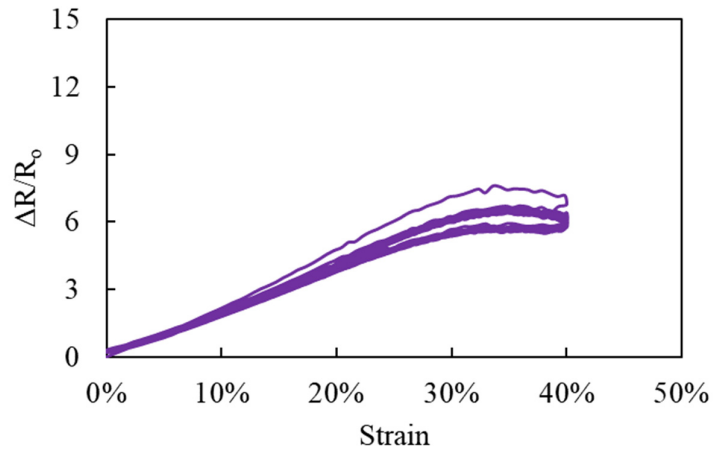


Figure 4.16. PDMS-PEIE-2/MWCNT-2 stretchable sensor characteristics at a tensile speed of 7 mm/s. (Adapted from ref. [20] with free distribution permission under the CC-BY License.)

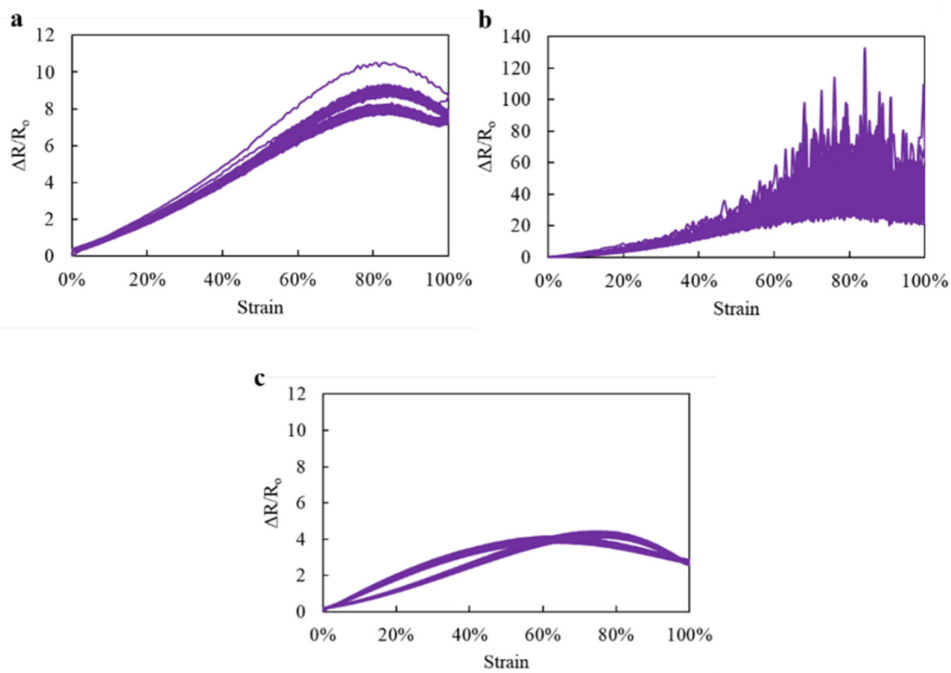


Figure 4.17. Sensor characteristics at a higher strain for (a) PDMS-PEIE-2/MWCNT-1, (b) PDMS-PEIE-2/MWCNT-2, and (c) PDMS-PEIE-2/MWCNT-3). (Adapted from ref. [20] with free distribution permission under the CC-BY License.)

PDMS-PEIE/MWCNT-2 (**Figure 4.15b**) shows a higher GF (**Figure 4.15e**) compared to the other stretchable strain sensors. GF is also sensitive to the tensile speed (**Figure 4.15e**). PDMS-PEIE/MWCNT-2 has a higher noise when it is stretched up to 100% strain (**Figure 4.17b**). For the PDMS-PEIE/MWCNT-3, GF changes as the strain increases (**Figure 4.15c**). A smaller GF value appears above 20% strain. Although the PDMS-PEIE/MWCNT-3 sensor can be stretched up to 100% strain, it has a lower linearity than the other two sensors. All of the fabricated sensors show a high repeatability since all readings have repeatable stretching and relaxing patterns during the cyclic tensile tests (**Figure 4.15**).

As reviewed above, since PDMS-PEIE/MWCNT-1 is better suited for detecting middle and high strain because it shows more linearity than the others, medium GF, non-sensitive GF toward different strain speeds and lower noise at high strain (100% strain). Hence, the PDMS-PEIE/MWCNT-1 is recommended for wearable devices, especially for those used in motion tracking.

To check the robustness of the stretchable sensor, additionally, a stretchable sensor of PDMS-PEIE/MWCNT-1 was also tested at several different tensile speeds. Each tensile test was a 1000 cyclic tensile test. In this additional investigation, a single PDMS-PEIE/MWCNT-1 went through 3000 cycles of stretch and relaxed testing. **Figure 4.18** shows the results at tensile speeds of 7 mm/s, 21 mm/s, and 30 mm/s. As expected, the sensor reading shows a lower noise. **Figure 4.18** also shows that the sensor reading converges from the second cycle to the end of the cycle. The converged curve shown in **Figure 4.18** indicates that the sensor is reliable. These thousands of cyclic tests also confirm the durability of the sensor in this strain range. This stable reading and the stretchable sensor robustness are expected to contribute to the development of future wearable devices.

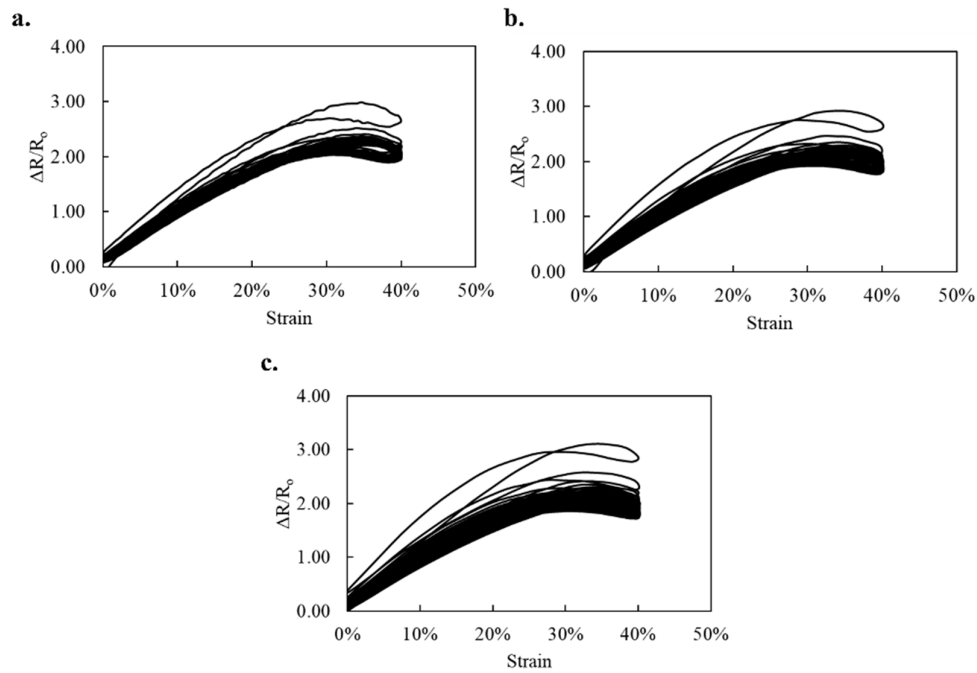


Figure 4.18. PDMS-PEIE/MWCNT-1 tested for 1000 cycle in each test and a tensile speed of (a) 7mm/s, (b) 21 mm/s, and (c) tensile speed of 30mm/s. (Adapted from ref. [20] with free distribution permission under the CC-BY License.)

In wearable devices, stretchable sensors often undergo a cyclic deformation at different strain rates. In this case, the stretchable sensor's maximum possibility of the strain speed that can be reached is an important aspect. The characteristics of the stretchable sensors are also an important aspect as they provide insight to determine potential applications other than wearable devices. The dynamic performance of PDMS-PEIE/MWCNT-1 was also evaluated on using ET139 by Labworks (see **Figure 4.19** for the experimental details). PDMS-PEIE/MWCNT-1 shows a stable performance when the sensor is subjected to a vibration frequency of 40 Hz (period of 25 ms) (**Figure 4.20**). The dynamic test indicates that PDMS-PEIE/MWCNTs-1 has a responsivity up to 25 ms.

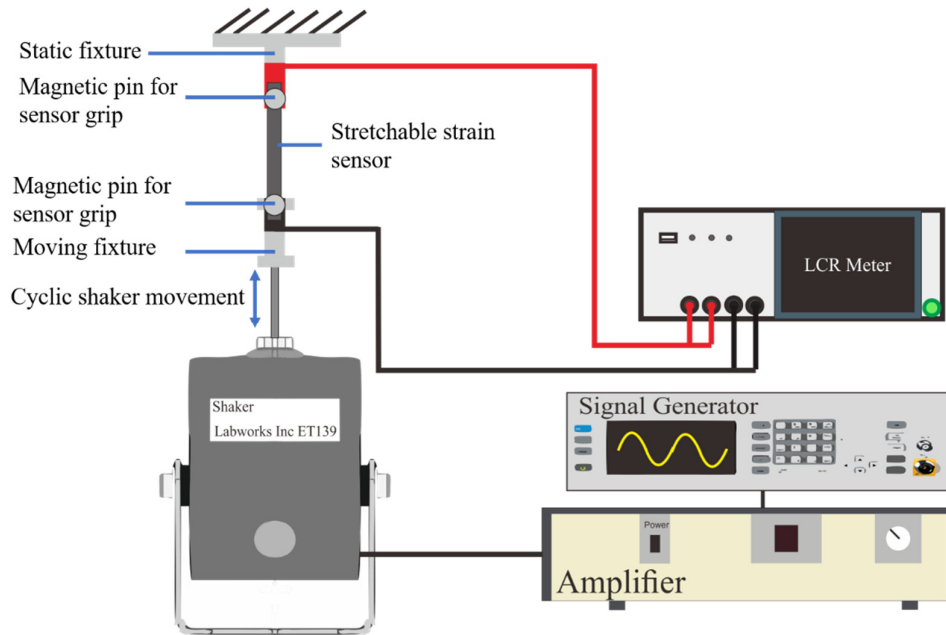


Figure 4.19. Sensor assessment for the vibration detection experimental setup. (Adapted from ref. ^[20] with free distribution permission under the CC-BY License.)

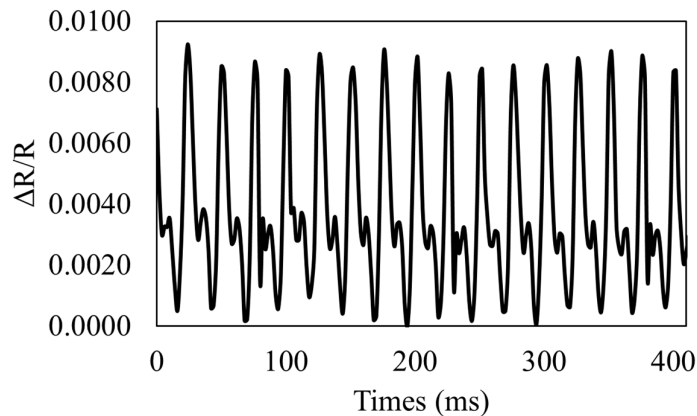


Figure 4.20. Response of a PDMS-PEIE/MWCNT-1 stretchable sensor to a vibration at 40 Hz. (Adapted from ref. ^[20] with free distribution permission under the CC-BY License.)

4.5 Stretchable sensor lamination process

To improve the compatibility of powdered-based stretchable sensors for wearable devices, lamination using a thin Ecoflex membrane was employed. The Ecoflex membrane was fabricated by spin-casting an Ecoflex solution at 2000 rpm for 30 seconds. Then the spin-casted Ecoflex was cured at 60 °C for 10 minutes. The thickness of the spin-casted Ecoflex membrane, which was evaluated after it was fully cured using a thickness screw gauge, was approximately 30–50- μm thick.

Figure 4.21 shows the lamination process. First, the sensor was peeled from the masking paper (**Figure 4.21a**). Then the stretchable sensor was fully covered with a thin Ecoflex membrane (**Figures 4.21b, c, and d**). Afterward, the unnecessary parts were removed using a cutter or scalpel (**Figure 4.21e**). The final step was to remove a small part of the Ecoflex membrane to create a contact surface (**Figure 4.21f**).

The lamination quality was tested by manually stretching (**Figure 4.21g**) and squeezing (**Figure 4.21i**) the sensor. **Figures 4.21h and j** demonstrate that squeezing and stretching do not induce a noticeable delamination of the Ecoflex thin membrane. Because PDMS-PEIE has a sticky nature, an adhesive was unnecessary to apply the thin membrane to the stretchable sensor. **Figure 4.22** shows the final structure of the stretchable sensor. As previously mentioned, the hole indicates the small Ecoflex membrane that was removed to create the contact point when the stretchable electrodes are applied in the wearable device and at the testing machine. The yellow part that was attached to the stretchable electrode was tape. This tape was for handling ease when attaching or removing the sensor from the wearable device. Lamination should not change the characteristics of the stretchable electrodes since the thickness of the Ecoflex used for lamination purposes was only 30–50- μm thick. The thickness of the elastomer used in this research was approximately 0.5 mm. This difference in thickness should not affect the mechanical properties of the stretchable sensor.

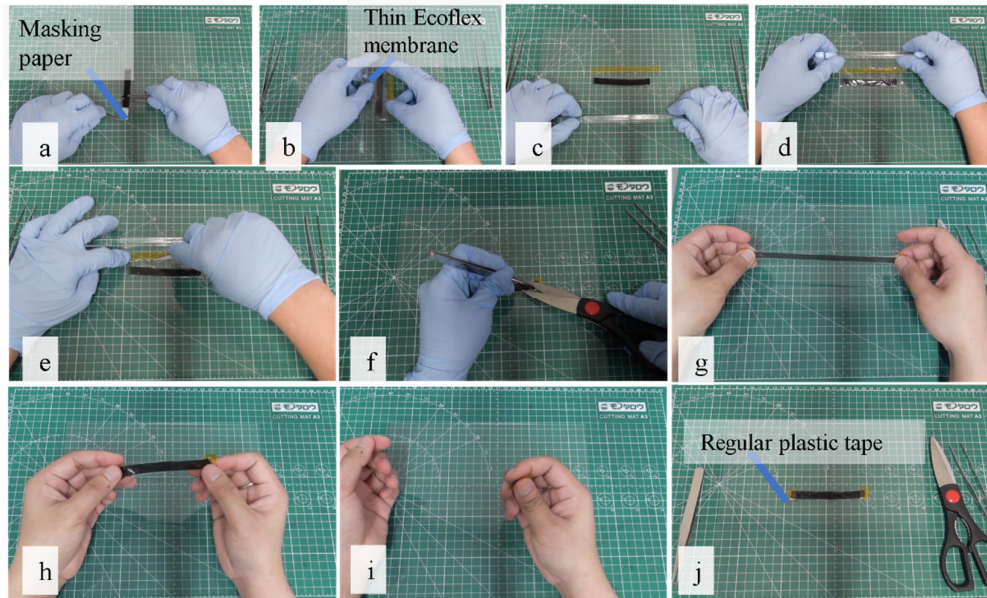


Figure 4.21. Sensor lamination process using a thin Ecoflex membrane. (Adapted from ref. [20] with free distribution permission under the CC-BY License.)

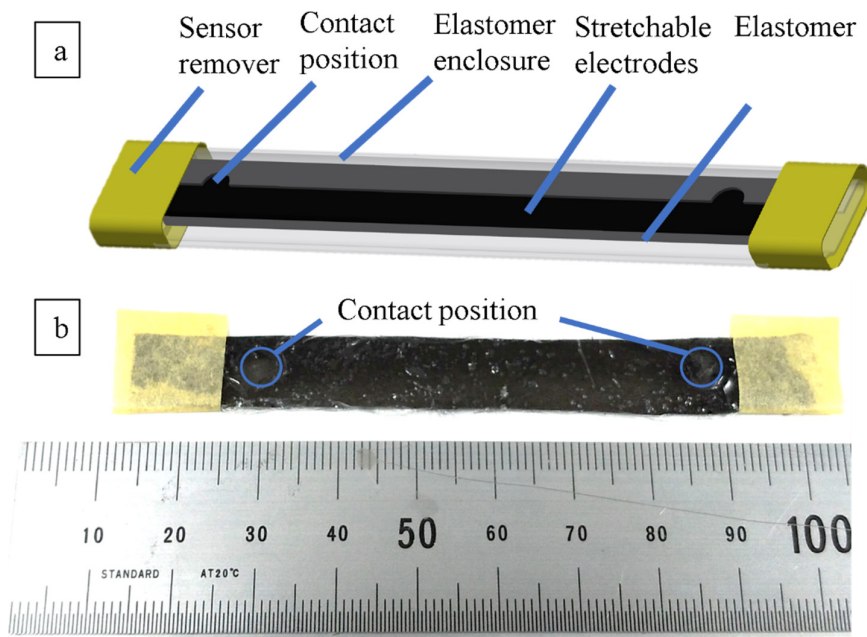


Figure 4.22. Final sensor structure after the lamination process. (Adapted from ref. [20] with free distribution permission under the CC-BY License.)

After the lamination process, the electromechanical characteristics of the laminated sensor were investigated. **Figure 4.23** shows the electromechanical characteristics of the carbon-based stretchable strain sensor after the lamination process. Comparing with the non-laminated stretchable strain sensor characteristics (**Figure 4.15a**), the lamination process does not affect the quality of the stretchable strain sensor (**Figure 4.23**).

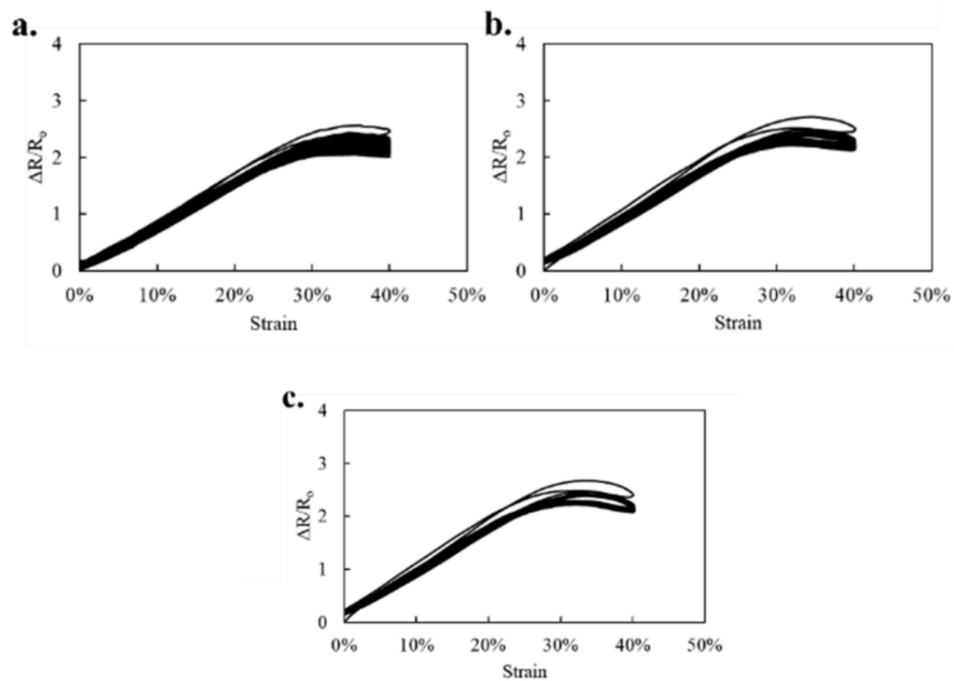


Figure 4.23. Stretchable strain sensor (PDMS-PEIE/MWCNT-1) characteristics after the lamination process using an Ecoflex membrane at a tensile test speed of (a) 7 mm/s, (b) 21 mm/s, and (c) 30 mm/s. (Adapted from ref. ^[20] with free distribution permission under the CC-BY License.)

4.6 Stretchable sensor for wearable devices

A plug-and-play concept is suitable for this stretchable strain sensor to simply attach it to any object, including the human body or wearable devices such as gloves or sleeves. This plug-and-play concept allows a stretchable sensor to be easily placed and adjusted. For long-term sensor operations, this concept can minimize regular maintenance. If the sensor is damaged, it can be easily removed and replaced with a new one. **Figure 4.24** shows an example where the device is attached to a glove.

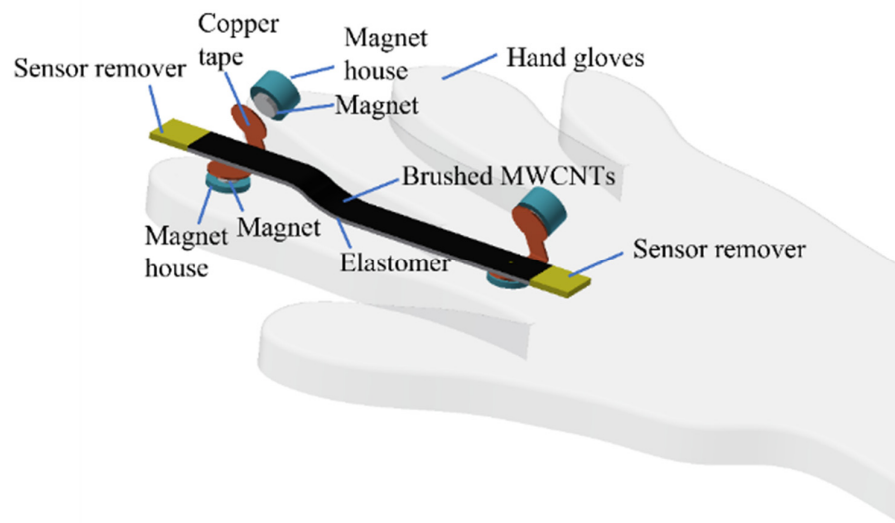


Figure 4.24. Plug-and-play concept of the stretchable strain sensor.
(Adapted from ref. ^[20] with free distribution permission under the CC-BY License.)

Figure 4.25 demonstrates the stretchable sensor as a wearable device. A hand movement is successfully detected using the resistance change of the sensor. The resistance is repeatedly changed according to the movement of the hand, demonstrating the potential of stretchable sensors to detect human movements.

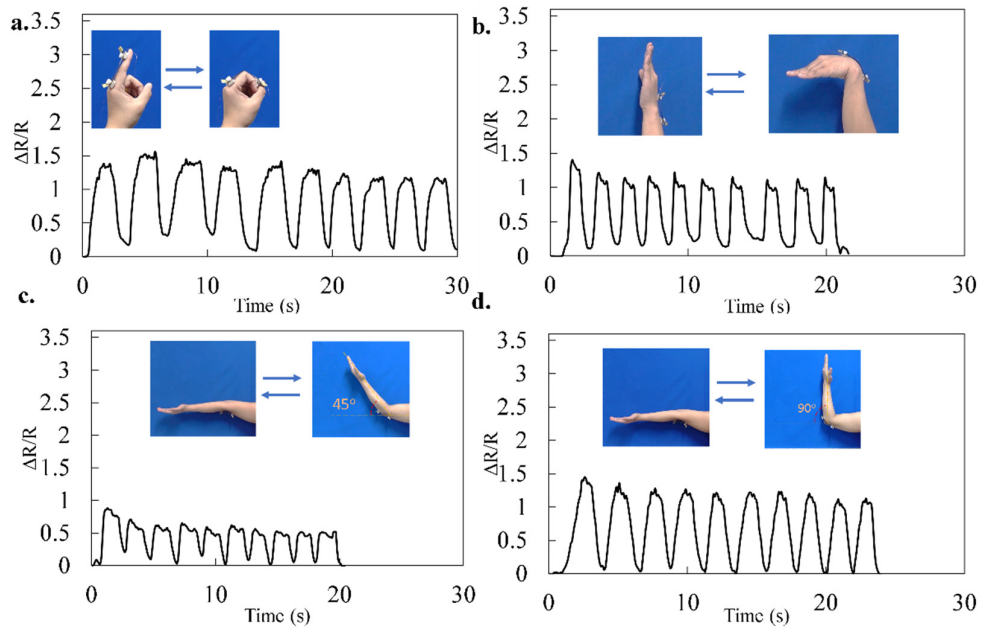


Figure 4.25. Response patterns of the PDMS-PEIE/MWCNT-1 sensor fixed on the (a) index finger, (b) wrist, (c) 45-degree movement of the elbow, and (d) 90-degree movement of the elbow. (Adapted from ref. ^[20] with free distribution permission under the CC-BY License.)

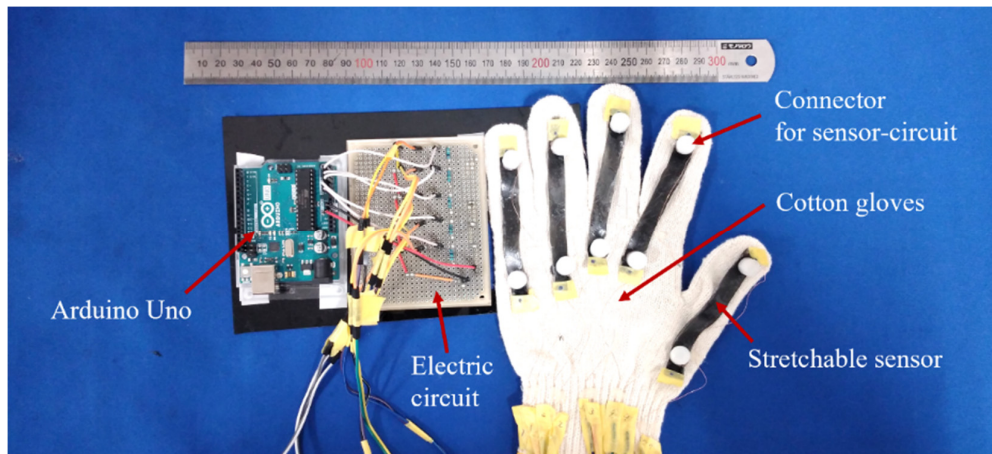


Figure 4.26. Wearable device arrangement to simulate and mimic human hand movements. (Adapted from ref. ^[20] with free distribution permission under the CC-BY License.)

For the next stage of wearable device prototyping, the stretchable strain sensor was integrated with a low-cost microcontroller (Arduino). **Figure 4.26** shows the device integration setup, and **Figure 4.27** shows details of the electric circuit for device integration. The electric circuit consisting of 1-M Ω resistors works as a simple voltage divider, allowing the analog signal to be read using Arduino Uno. Moving the glove induces a difference in the resistance of the system. This resistance change due to the hand-glove finger movement influences the voltage signal read by the analog pin in Arduino. Then the signal from the analog pin is further mapped and sent to a personal computer USB port. Finally, blender software captures the hand movement simulation. **Figure 4.28** shows a simulation of the hand gloves using blender software. A simple calibration algorithm was also used to improve the accuracy of hand motion detection. In principle, the maximum and minimum values of the sensor were recorded and mapped into vectors. Then the change in the vector values were used to simulate the hand movement in blender software. This simple calibration algorithm is necessary since the movement range of every finger depends on the person and a person's hand size affects the range of the sensor readings.

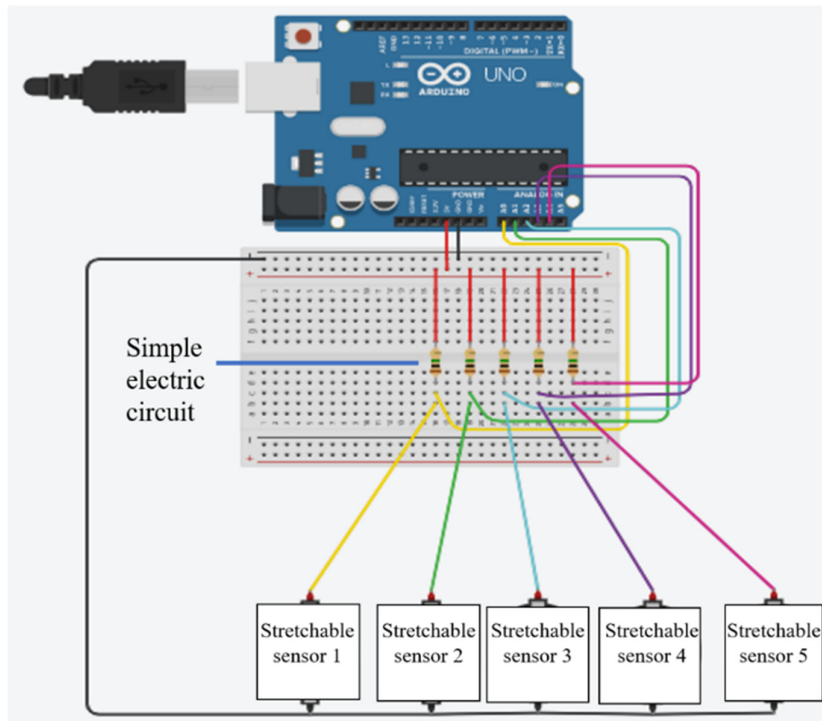


Figure 4.27. Detailed electric circuit for the stretchable strain sensor reader and signal processor. (Adapted from ref. [20] with free distribution permission under the CC-BY License.)

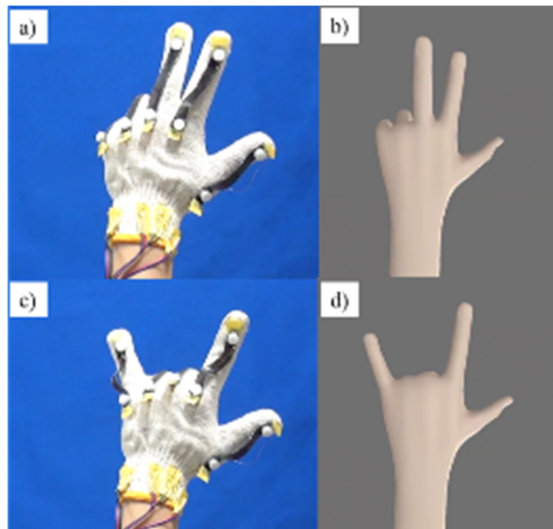


Figure 4.28. (b and d) Control simulation of a virtual hand using (a and c) a stretchable strain sensor attached to a cotton hand glove. (Adapted from ref. [20] with free distribution permission under the CC-BY License.)

4.7 Conclusion

This chapter demonstrates an automatic brushing process for stretchable electrodes to remove the human influence in the brushing process. The fabrication process utilizing an automatic brushing machine is straightforward. This chapter also reports an improvement of the elastomer compatibility in the brushing process.

The overall material optimization indicates that PDMS-PEIE with a composition of 3.2 wt% curing agent and 0.11 wt% PEIE is the most compatible for stretchable elastomers. This PDMS-PEIE is 50% more stretchable and 63% stickier than previously reported PDMS 30-1. This improved stretchability can enhance the sensing range of the stretchable strain sensors. The optimized stickiness characteristics also improve the physical bonding quality between the elastomer surface and the MWCNT powder. Strong physical binding between MWCNTs and the elastomer surface enhances the electrode conductivity while simultaneously reducing the risk of self-delamination of MWCNT powder from the elastomer surface.

This research also indicates that each carbon powder has its own strengths and weaknesses. MWCNT-1 shows a relatively better performance in terms of linearity and repeatability. The combination of MWCNT-1 and PDMS-PEIE has potential for higher strain sensing.

This chapter demonstrates that using a lamination process improves the compatibility of powdered-based stretchable electrodes for wearable devices. The lamination process involves the wrapping mechanism of the stretchable electrode using a thin layer of Ecoflex. The final stage demonstrates the integration of stretchable electrodes for a wearable device and simulates hand movement tracking in blender software.

This chapter describes the development of a customized electromechanical tensile test for soft and stretchable materials. Three standalone devices are integrated using Python software and a friendly GUI is introduced for easy operation of the equipment. This customized electromechanical tensile test should contribute to

advances in soft robotics, especially soft and stretchable sensors. This electromechanical setup should also aid in the development of laboratory equipment and the understanding of the electromechanical properties of stretchable conductive materials.

Chapter 5

Potential fabrication of Ultra-Low-Voltage DEAs

5.1 Introduction

DEAs are a promising technology for soft actuators since they have high energy density^{[44][119]} and fast response.^{[6][35]} DEAs have a simple structure, which can be used to create bioinspired robots (e.g., a DEA insect-scale,^{[15][120][121]} DEAs for under water robots,^{[122]–[124]} and DEAs for artificial muscles^{[125]–[130]}). DEAs are a promising soft actuator technology due to their high energy density^{[44][119]} and fast response.^{[6][35]} As previously discussed in **chapter 1** and **chapter 3**, DEAs depend on the elastomer, stretchable electrodes, and the driving voltage. **Figure 3.11** shows the effect of a voltage increase on the actuation of DEAs. The higher the driving voltage, the higher the actuation strain of the DEA. Typically, a kV range is required to drive DEAs with a thickness of hundreds of micrometers. A practical advantage of DEAs can be obtained when they can operate at low voltage. One possible application of low-voltage DEAs is a haptic feedback device (HFD).^[16] HFD usually has direct contact with a human body. In this case, low-voltage operations should ensure safe conditions for humans and open new applications for DEAs.

In HFD, DEAs should operate over a wide range of frequencies to provide a multi-sensational-feedback feeling when the device is utilized for a specific purpose. A current challenge of DEAs for HFD is the high driving voltage limits the application of DEAs in the device. In addition, cost, bulkiness, and electronics safety are concerns.^[5] Electricity safety for human is mandatory when designing an electromechanical actuator system. Our nanosheet-DEAs use DC voltage sources, which show superior safety compared to that of an AC voltage source. The DC voltage does not have a definite shake-off threshold, which causes muscle pain and a spasm-like contractions.^[131] Typically, DC electricity has a smaller electric shock accident risk than that of AC because shake off from the DC conductor is easier. Moreover, when the electric shock duration is higher than the cardiac cycle (around 800 ms), the ventricular fibrillation threshold of DC greatly exceeds that of AC.^[131]

There are three variables that affect the human body response to electrical shock: the electrical resistance of the body, the amplitude of the applied voltage, and the amplitude of the current flowing through the body.^[132] Considering these variables, the latest study on DC voltage to human health found that a DC voltage less than 72 V will not cause skin scars, organ damage, or more dangerous injuries,^[131] and when operated in a dry environment, it will not cause an unconscious cardiac muscle response. This value of DC voltage has been confirmed as safe in medical treatments.^[133]

Much effort has been devoted to reducing the driving voltage of DEAs. For example, studies have decreased the film thickness, reduced the elastic modulus,^{[21][134]} and increased the dielectric permittivity^[5] of DE membranes. To design low-voltage DEAs, researchers must also consider the electrical breakdown (E_b) of DEAs. E_b depends on both the thickness and the stretching ratio of the DE membrane. Reducing the membrane thickness is a reasonable approach to improve the E_b field. Previously, Gatti et al.^[135] developed an empirical formula to model E_b of PDMS-based DEAs, as shown in **Equation 5.1**.

$$E_B = 147 t^{-0.23 \pm 0.02} \lambda^{1.77 \pm 0.03} \quad (5.1)$$

where t is the initial elastomer thickness in μm , E_B is the electrical breakdown field strength in $\text{V}/\mu\text{m}$, and λ is the stretching ratio. Based on **Equation 5.1**, minimizing the elastomer thickness can simultaneously optimize E_B of the DE and reduce the DEA driving voltage.

Theoretically, fabricating ultrathin DEs and stretchable electrodes should reduce the driving voltage of DEAs. To achieve a driving voltage below 100 V, the elastomer and stretchable electrodes for DEAs should also be in the nanometer range. This chapter fabricates nanometer-sized elastomer and stretchable electrodes using the roll-to-roll (R2R) method. The final stage is to assemble nanometer-sized stretchable electrodes and elastomers to realize ultra-low-voltage DEAs.

5.2 Nanosheet fabrication method

PDMS nanosheets were fabricated with three layers: a PET (polyethylene terephthalate) film as a temporary supporting substrate, PVA (polyvinyl alcohol) membrane as a sacrificial layer, and PDMS as a nanosheet. Stretchable electrodes were composed of a poly(3,4-ethylenedioxythiophene): poly(4-styrenesulfonate) (PEDOT:PSS) (PEDOT:PSS aqueous dispersion, Clevios PH1000 from H.C. Starck GmbH, Leverkusen, Germany)^[136] ultrathin layer coated on a poly(styrene-*b*-butadiene-*b*-styrene) (SBS) nanosheet.

Both stretchable electrodes and the PDMS nanosheet were fabricated using the R2R process under the same conditions reported by Yamagishi et al.^[137] First, a polymer solution was deposited on the desired substrate using a gravure roll (**Figure 5.1a**). As the gravure roll rotated, a polymer solution was continuously coated onto a flexible substrate while a blade scraped the roll to remove the excess polymer solution. Second, the substrate moved along with the roll, and the sheets were dried using a hot air flow drier along the R2R line. Finally, the flexible substrate coated with the cured polymer was collected on the output roll. **Figures 5.1b** and **5.1c** respectively show a schematic image of the multilayered structure and the morphological feature of the final product, including the nanosheet fabricated by the R2R method.

The thin-film structure consisted of three layers (**Figure 5.1b**): a PET film, a PVA layer, and a 600-nm-thick PDMS nanosheet. The PVA layer worked as a sacrificial layer for facile detachment of the PDMS nanosheet. According to a previous report,^[137] a bilayer structure of a nanosheet consisting of poly(3,4-ethylenedioxythiophene):poly(4-styrenesulfonate) (PEDOT:PSS) and poly(styrene-*b*-butadiene-*b*-styrene) (SBS) (referred to as “PEDOT:PSS-SBS nanosheet”) with a total thickness of ~200 nm was also prepared.

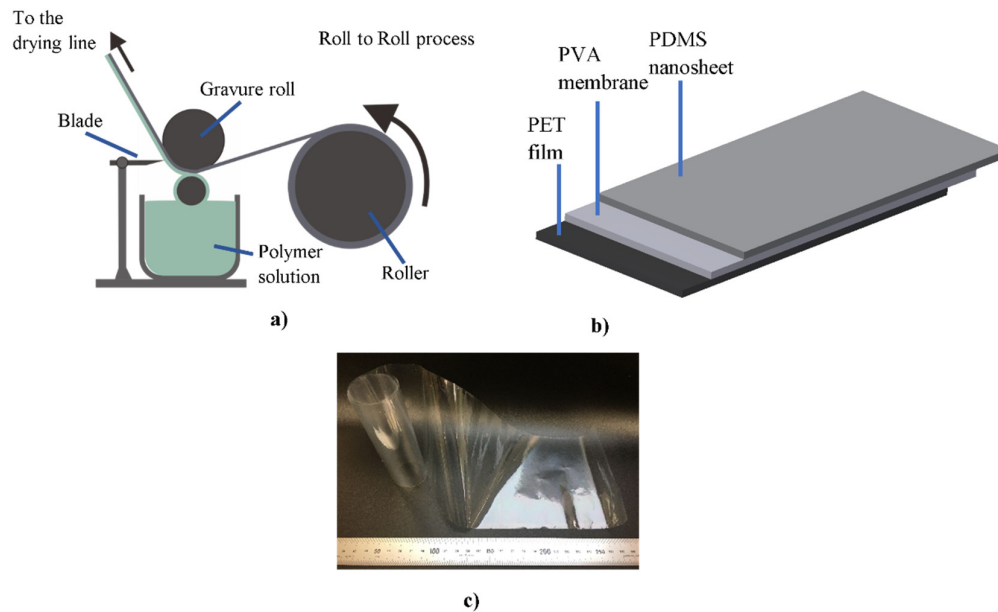


Figure 5.1. Roll-to-roll (R2R) process for fabricating nanosheets. (a) Schematic of the R2R process, (b) multilayered structure, and (c) actual image of the final product. (Adapted from ref. ^[138] with free distribution permission under the CC-BY License.)

5.3 Ultra-low voltage DEAs fabrication

To assemble the nanosheet PDMS and stretchable electrodes, the first step was to manually remove the nanosheet PDMS-PVA membrane from the hard PET membrane (**Figure 5.2a**). The removal technique also works for a PEDOT:PSS-SBS (stretchable electrode) membrane since both nanosheet PDMS and PEDOT:PSS-SBS are formed on a PVA coating with a PET roll substrate.

To remove the PVA layer from both nanosheets, the PDMS nanosheets were submerged in a NaCl–water solution (15 wt% of NaCl) with the PVA layer facing the liquid solution (**Figures 5.2b and d**). Next a rigid frame was applied to the PDMS nanosheet (**Figure 5.2c**). Then the electrodes (PEDOT:PSS-SBS) were applied to the PDMS nanosheet (**Figure 5.2e**). After the nanosheet PDMS was sandwiched between PEDOT:PSS-SBS, the nanosheet DEA was kept at room temperature until the nanosheet was fully dried (approximately 24 hours). The next process connected low-voltage DEAs with a wire using carbon ink (**Figure 5.2f**). The final process was

to operate the DEAs at room temperature conditions (20 °C and relative humidity of 50%).

5.4 Actuation demonstration of ultra-low-voltage DEAs at high-frequency operations

To demonstrate the operation of low-voltage DEAs at high-frequency operations, the DEA (**Figure 5.2f**) was connected to DC voltage sources of 20, 50, and 90 V, which had calculated electrical fields of 33.3, 83.3, and 150 mV/nm, respectively. To change the frequency operations of the nanosheet DEAs, a signal generator was used. This signal generator produced a sine wave by repeatedly switching the DC voltage electric source on–off with a frequency of 1–30 kHz. A laser Doppler vibrometer (Polytec OFV-505) was used to investigate the actuation performance of the DEAs (**Figure 5.3**).

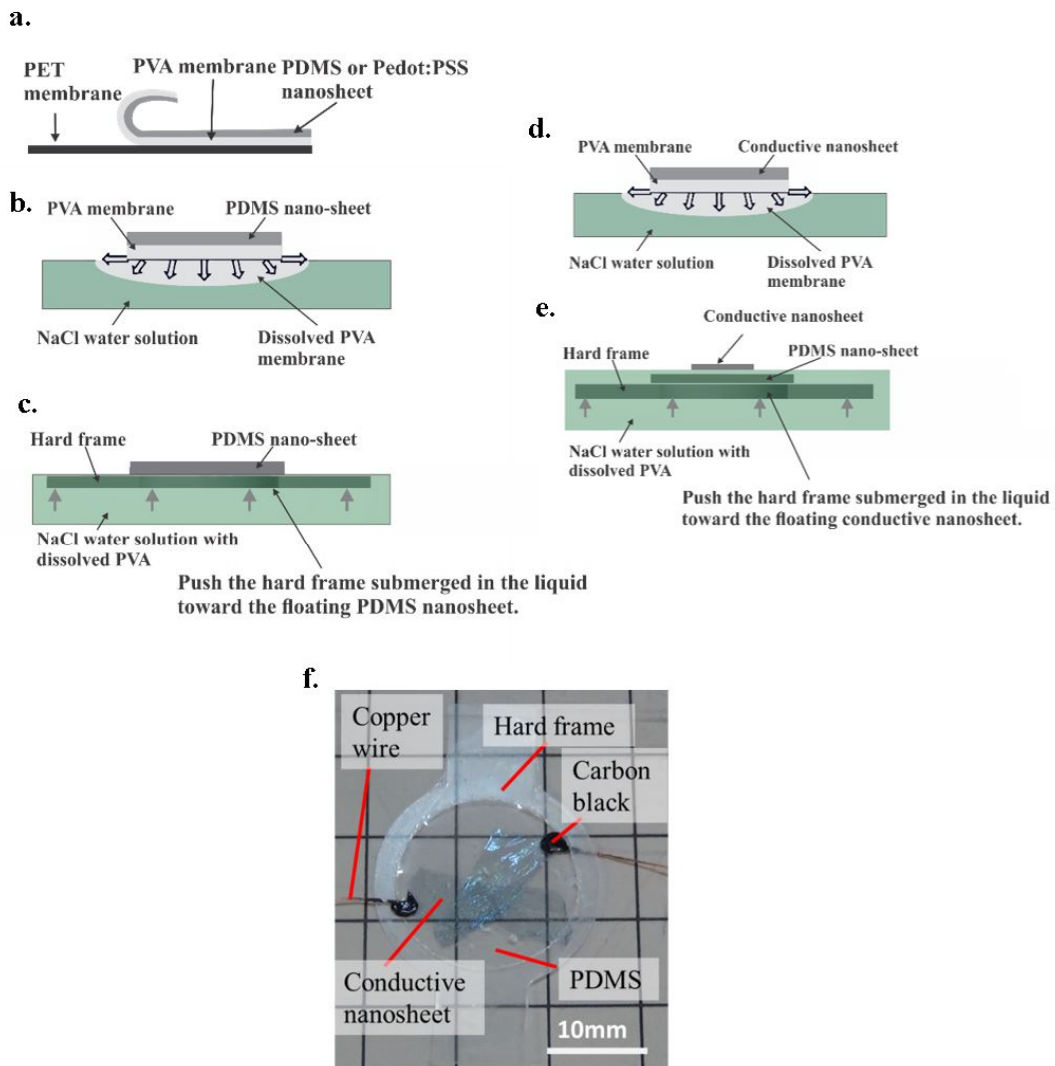


Figure 5.2. Nanosheet DEA fabrication process. (a) Detachment process of the nanosheet membrane from the supporting material. (b and d) PVA removal process from the nanosheet membrane. (c) Frame application to the nanosheet PDMS membrane. (e) Application of the conductive nanosheet on the PDMS nanosheet surface. It should be noted that this process is repeated twice to attach the electrodes on both sides of nanosheet PDMS. (f) Low-voltage DEAs. (Adapted from ref. ^[138] with free distribution permission under the CC-BY License).

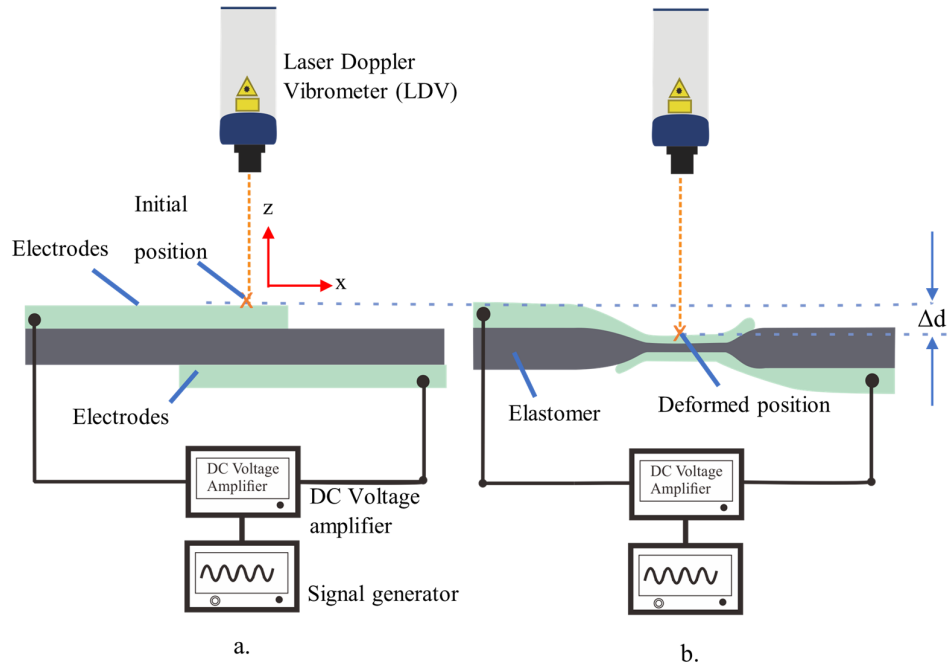


Figure 5.3. Actuation velocity measurements of DEAs in the (a) undeformed and (b) deformed (actuated) states. (Adapted from ref. ^[138] with free distribution permission under the CC-BY License.)

Figure 5.4 shows the time history of the waveforms in the DE actuation. **Figures 5.4a, b, and c** depict the first 10 DEA actuation cycles. In this experiment, the DEA velocity response was defined as the time needed by the DEA surface to deform and relax cyclically. Surprisingly, the nanosheet DEA actuates at 50 V and covers a high frequency, including the ultrasonic frequency. The low-voltage DEAs can respond with similar actuation characteristics when they are driven with a high-frequency DC voltage. The waveforms of the nanosheet-DEAs have identical sinusoidal shapes as those operated at lower actuation frequencies (**Figures 5.4a and b**). Higher-frequency operations of 30 kHz also show actuation close to a sinusoidal shape (**Figure 5.4c**). This indicates that low-voltage DEAs can handle operations over a wide range of frequency actuations. Moreover, **Figure 5.4** also indicates a repeatable high-frequency response of the nanosheet DEAs.

Furthermore, the response of the nanosheet DEAs in the thickness direction at high-frequency operations was confirmed by integrating the velocity response over time using a numerical integration Matlab toolbox (cumulative trapezoidal rule). **Figure 5.5** shows the displacement of the nanosheet DEA membrane in the z-direction. The estimated displacement of the nanosheet DEA is several nanometers.

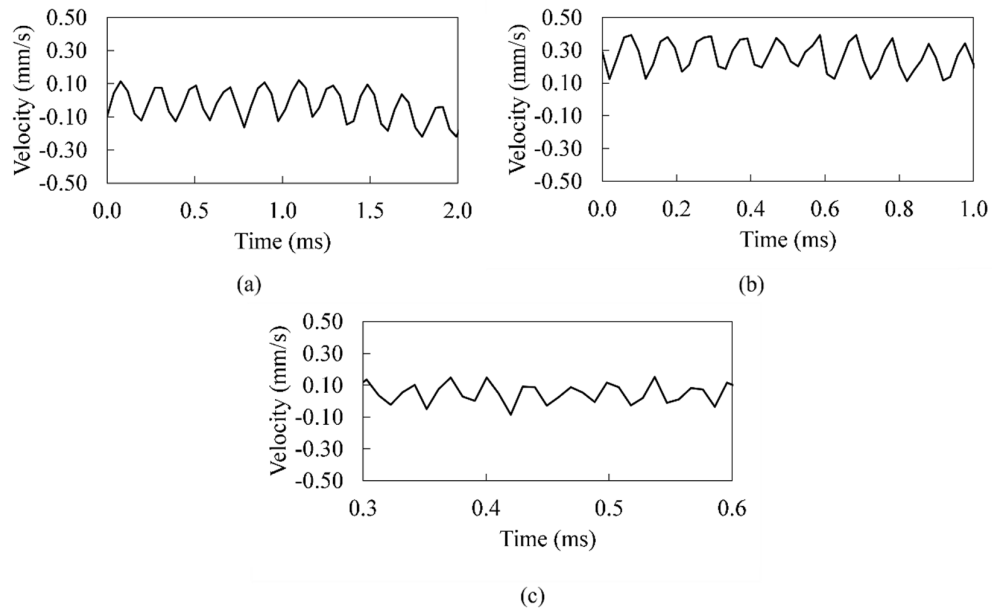


Figure 5.4. Velocity responses on the nanosheet DEA surface at a voltage of 50 V and (a) 5 kHz, (b) 10 kHz, and (c) 30 kHz. (Adapted from ref. ^[138] with free distribution permission under the CC-BY License.)

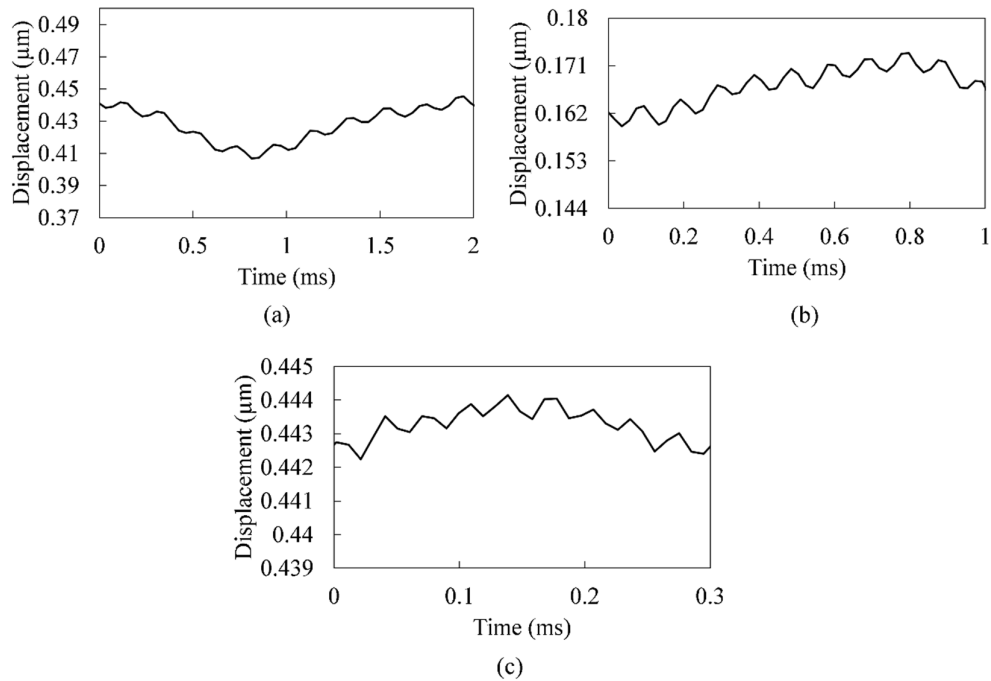


Figure 5.5. Displacement in the thickness direction (z-axis direction) of nanosheet DEAs at a voltage of 50 V and (a) 5 kHz, (b) 10 kHz, and (c) 30 kHz. (Adapted from ref. ^[138] with free distribution permission under the CC-BY License.)

5.5 Conclusion

This chapter investigates a simple and novel method to fabricate low-voltage DEAs. A R2R method is used to fabricate nanosheet-type elastomers and stretchable electrodes. Based on the research, the R2R method can effectively realize ultrathin stretchable electrodes and DE membranes. For ease of material handling, PVA and PET can be used as a sacrificial layer and supporting material, respectively.

To fabricate low-voltage DEAs, the optimized condition to remove the PVA on the nanosheet PDMS and the stretchable electrode is achieved using 15 wt% NaCl–water solution. Furthermore, a total of approximately 1- μm -thick DEA enables operations at a low voltage below 70 V. As presented in **subchapter 5.4**, DEAs work at voltages below 70 V and at high-frequencies (1–30 kHz) without any problems.

Chapter 6 Summary

This work presents a novel, simple, and reliable fabrication process of DE sensors and actuators for soft robotics and wearable devices.

Chapter 1 mainly introduces stretchable electrodes in DEAs and DEs. In particular, the simple mechanism of DEAs, the principle of a stretchable strain sensor, several fabrication methods of stretchable electrodes, and a simple strategy to implement stretchable electrodes as wearable devices are presented.

Chapter 2 provides a general review of the fabrication methods for stretchable electrodes. Detailed information on the simple manual brushing mechanism and automatic brushing method for stretchable electrodes are included. This chapter also mentions the equipment needed to build an automatic brushing machine for stretchable electrodes.

Chapter 3 mainly discusses a simple and reliable fabrication method for PDMS DEAs using CNT powder electrodes. First, the relationship between the mechanical characteristics of Sylgard 184 and the mixing ratio between the elastomer base and its curing agent are investigated using a single-pull-to-failure tension test. Then the relationship between the elastomer stress-softening, stickiness surface characteristic of the elastomer due to the different mixing ratios of the PDMS solution, and the actuation performance of DEAs are evaluated in static and dynamic actuations.

Altering the mixing ratio of the base elastomer and the curing agent helps to change the mechanical characteristics of PDMS. Reducing the curing agent in the mixing ratio results in materials with softer characteristics and stickier surface characteristics. Reducing the curing agent (from PDMS 10-1 to PDMS 30-1) also improves the actuation strain of the DEAs in static operations. The stickier surface characteristic strengthens the binding force between the MWCNT powder and the elastomer membrane. This strong binding force also strengthens the network connection between the MWCNT powder and helps realize a better conductivity of the electrodes, allowing the electricity to be transmitted uniformly over the electrode

network. This better electrode conductivity realizes DEAs with more stable dynamic performances.

Chapter 4 provides a DIY approach to incorporate stretchable sensors using CNT powder for wearable devices. The elastomer compatibility with the brushing method is optimized using PEIE. Then the best mixing ratio of PDMS and PEIE is selected to increase the stickiness characteristics of the elastomer. Afterward, stretchable strain sensors are created using an automatic brushing machine. Next, the sensor characteristics fabricated using different types of MWCNTs are investigated. Finally, the stretchable sensor is integrated with a low-cost microcontroller for a wearable device.

Chapter 5 shows the potential of DEAs in low-voltage and high-frequency operations. The strategy to realize ultra-low voltage operations consists of reducing the DE membrane thickness. First, a PDMS nanosheet is fabricated with three layers (a PET film as the temporary supporting substrate, a PVA membrane as the sacrificial layer, and PDMS as the nanosheet). The PDMS nanosheet can be released from the temporary substrate and easily transferred to any target surface. Then an approximately 600-nm-thick DE membrane and 200-nm-thick stretchable electrodes are integrated to realize ultra-low-voltage DEAs. Finally, dynamic actuation of DEAs is demonstrated at high frequencies (5 – 30 kHz).

Acknowledgement

I would like to express my sincere gratitude to Professor Shingo Maeda, who guided me during my Doctoral course and taught me many things about the future and bright world of research in smart material.

I would like to express my sincere appreciation to Professor Naoki Hosoya, who taught me how to do research and set up proper experimental things.

I sincerely appreciate Professor Yasuyuki Ishii for his technical advice and valuable discussion during my studies.

I sincerely appreciate Professor Shinji Hashimura for the valuable advice on designing experimental equipment during my study.

I sincerely appreciate Professor Sumito Nagasawa for the valuable advice and comment during the manuscript writing process and the examination process.

I sincerely appreciate Professor Itsuro Kajiwara from Hokaido University for the insightful comment and advice during the manuscript preparation process and examination.

I would like to express my sincere thanks to Associate Professor Hiroki Shigemune for the supportive discussion and advice during my study in Japan.

I would like to thank Dr. Zebing Mao for the wonderful discussion and support during my study.

I would like to thank Dr. Yuhei Yamada for the warm discussion and much advice about the theoretical study.

I would like to thank Professor Toshinori Fujie and Dr. Tatsuhiko Horii from School of Life Science and Technology, Tokyo Institute of Technology, for the wonderful collaboration during my study

I would like to thank all Maeda lab members for the discussion and support during my study.

I would like to thank and express my gratitude to the head of the Mechanical and Industrial Engineering Department, University of Gadjah Mada for the endless support during my doctoral program in Japan.

I would like to express my gratitude to my previous supervisor at the University of Gadjah Mada: Dr Indro Pranoto, Professor Deendarlianto, Dr Adhika Widyaparaga, Dr I Made Miasa, Dr Indraswari Kusumaningtyas, Dr Teguh Pudji Purwanto, Dr Rachmat Sriwijaya and Professor Noer Ilman for the support and insightful discussion during my study in Japan.

I would like to thank all of the Mechanical and Industrial Engineering Department staff, University of Gadjah Mada for always taking care of my administrative work in the University of Gadjah Mada during my absence.

Finally, I would like to express my greatest gratitude and appreciation to my parents, elder sister, and my wife Titi Sari for supporting, praying, and watching over my study.

Reference

- [1] M.W.M. Tan, G. Thangavel, P.S. Lee, *NPG Asia Mater.* **2019**, *11*, 62.
- [2] J. Shintake, E. Piskarev, S.H. Jeong, D. Floreano, *Adv. Mater. Technol.* **2018**, *3*, 1.
- [3] S. Rosset, H.R. Shea, *Appl. Phys. A Mater. Sci. Process.* **2013**, *110*, 281.
- [4] C. Keplinger, J. Sun, C.C. Foo, P. Rothmund, G.M. Whitesides, Z. Suo, *Science (80-)*. **2013**, *341*, 984.
- [5] A. Poulin, S. Rosset, H.R. Shea, *Appl. Phys. Lett.* **2015**, *107*, 244104.
- [6] X. Ji, A. El Haitami, F. Sorba, S. Rosset, G.T.M. Nguyen, C. Plesse, F. Vidal, H.R. Shea, S. Cantin, *Sensors Actuators, B Chem.* **2018**, *261*, 135.
- [7] S. Taccola, A. Bellacicca, P. Milani, L. Beccai, F. Greco, *J. Appl. Phys.* **2018**, *124*, 064901.
- [8] T. Dong, Y. Gu, T. Liu, M. Pecht, *Sensors Actuators, A Phys.* **2021**, 326.
- [9] P. Song, G. Wang, Y. Zhang, *Sensors Actuators, A Phys.* **2021**, 323, 112659.
- [10] C. Jin, D. Liu, M. Li, Y. Wang, *J. Mater. Sci. Mater. Electron.* **2020**, *31*, 4788.
- [11] J. Teixeira, L. Horta-Romarís, M.J. Abad, P. Costa, S. Lanceros-Méndez, *Mater. Des.* **2018**, *141*, 1.
- [12] J.T. Muth, D.M. Vogt, R.L. Truby, Y. Mengüç, D.B. Kolesky, R.J. Wood, J.A. Lewis, *Adv. Mater.* **2014**, *26*, 6307.
- [13] R. Urbas, U.S. Elesini, T. Cigula, S.M. Poljacek, in *Annu. Rev. Mater. Sci.*, **2016**, 263.
- [14] jeremy J. Ramsden, *Nanotechnology An Introduction*, **2011**.
- [15] X. Ji, X. Liu, V. Cacucciolo, M. Imboden, Y. Civet, A. El Haitami, S. Cantin, Y. Perriard, H. Shea, *Sci. Robot.* **2019**, *4*, 1.
- [16] X. Ji, X. Liu, V. Cacucciolo, Y. Civet, A. El Haitami, S. Cantin, Y. Perriard, H. Shea, *Adv. Funct. Mater.* **2020**, 2006639, 1.
- [17] A.V. Singh, *J. Biomed. Mater. Res. - Part A* **2013**, *101*, 2994.
- [18] R. Elhajjar, V. La Saponara, A. Muliana, *Smart Composites Mechanics and Design*, **2014**.
- [19] M. Fazeli, J.P. Florez, R.A. Simão, *Compos. Part B Eng.* **2019**, *163*, 207.
- [20] A. Wiranata, Y. Ohsugi, A. Minaminosono, Z. Mao, H. Kurata, N. Hosoya, S.

- Maeda, *Front. Robot. AI* **2021**, 8, 1.
- [21] A. Wiranata, Y. Ishii, N. Hosoya, S. Maeda, *Adv. Eng. Mater.* **2021**, 23, 1.
- [22] A. Minaminosono, H. Shigemune, T. Murakami, S. Maeda, *Smart Mater. Struct.* **2021**, 30, 065007.
- [23] P. Chakraborti, H.A.K. Toprakci, P. Yang, N. Di Spigna, P. Franzon, T. Ghosh, *Sensors Actuators, A Phys.* **2012**, 179, 151.
- [24] H. Zhao, A.M. Hussain, M. Duduta, D.M. Vogt, R.J. Wood, D.R. Clarke, *Adv. Funct. Mater.* **2018**, 1804328, 1.
- [25] A. Wiranata, S. Maeda, O. Keiya, *SEATUC J. Sci. Eng.* **2020**, 1, 14.
- [26] M. Tschiersky, E.E.G. Hekman, D.M. Brouwer, J.L. Herder, K. Suzumori, *IEEE Robot. Autom. Lett.* **2020**, 5, 3042.
- [27] S. Koizumi, S. Kurumaya, H. Nabae, G. Endo, K. Suzumori, *Soft Robot.* **2020**, 7, 1.
- [28] H. Nabae, A. Kodaira, T. Horiuchi, K. Asaka, G. Endo, K. Suzumori, *IEEE/RSJ Int. Conf. Intell. Robot. Syst.* **2019**, 8287.
- [29] V. Cacucciolo, J. Shintake, Y. Kuwajima, S. Maeda, D. Floreano, H. Shea, *Nature* **2019**, 572, 516.
- [30] V. Cacucciolo, H. Nabae, K. Suzumori, H. Shea, *Front. Robot. AI* **2020**, 6, 1.
- [31] T. Hiruta, N. Hosoya, S. Maeda, I. Kajiwara, *Int. J. Mech. Sci.* **2021**, 191, 106049.
- [32] D. Mccoul, S. Rosset, N. Besse, H. Shea, *Smart Mater. Struct.* **2016**, 26, 1.
- [33] H. Shigemune, S. Sugano, J. Nishitani, M. Yamauchi, N. Hosoya, S. Hashimoto, S. Maeda, *Actuators.* **2018**, 7, 1.
- [34] A. Minaminosono, H. Shigemune, Y. Okuno, T. Katsumata, N. Hosoya, S. Maeda, *Front. Robot. AI* **2019**, 6, 1.
- [35] N. Hosoya, H. Masuda, S. Maeda, *Appl. Acoust.* **2019**, 148, 238.
- [36] N. Hosoya, S. Baba, S. Maeda, *J. Acoust. Soc. Am.* **2015**, 138, EL424.
- [37] Y. Seki, Y. Kuwajima, H. Shigemune, Y. Yamada, S. Maeda, *J. Robot. Mechatronics* **2020**, 32, 939.
- [38] Y. Kuwajima, Y. Seki, Y. Yamada, S. Awaki, S. Kamiyauchi, A. Wiranata, Y. Okuno, H. Shigemune, S. Maeda, *ACS Appl. Mater. Interfaces* **2022**.

- [39] J. Mehta, Y. Chandra, R.P. Tewari, *Procedia Comput. Sci.* **2018**, *133*, 569.
- [40] M. Wissler, E. Mazza, *Smart Mater. Struct.* **2005**, *14*, 1396.
- [41] N.F. Wang, C.Y. Cui, H. Guo, B.C. Chen, X.M. Zhang, *Sci. China Technol. Sci.* **2018**, *61*, 1512.
- [42] X. Zhao, Z. Suo, *Phys. Rev. Lett.* **2010**, *104*, 1.
- [43] D. Sangian, *Smart Mater. Struct.* **2020**, *29*, 1.
- [44] R. Pelrine, R. Kornbluh, J. Joseph, R. Heydt, Q. Pei, S. Chiba, *Mater. Sci. Eng. C* **2000**, *11*, 89.
- [45] S. Michel, X.Q. Zhang, M. Wissler, C. Löwe, G. Kovacs, *Polym. Int.* **2010**, *59*, 391.
- [46] X. Zhang, M. Wissler, B. Jaehne, R. Breonnimann, G. Kovacs, in *Smart Struct. Mater. 2004 Electroact. Polym. Actuators Devices*, **2004**, 78.
- [47] I.J. Kim, K. Min, H. Park, S.M. Hong, W.N. Kim, S.H. Kang, C.M. Koo, *J. Appl. Polym. Sci.* **2014**, *131*, 24.
- [48] T.K. Kim, J.K. Kim, O.C. Jeong, *Microelectron. Eng.* **2011**, *88*, 1982.
- [49] S. Akbari, S. Rosset, H.R. Shea, *Appl. Phys. Lett.* **2013**, *102*, 071906.
- [50] M. Kamperman, E. Kroner, A. Del Campo, R.M. McMeeking, E. Arzt, *Adv. Eng. Mater.* **2010**, *12*, 335.
- [51] F. Carpi, I. Anderson, S. Bauer, G. Frediani, G. Gallone, M. Gei, C. Graaf, C. Jean-mistral, W. Kaal, G. Kofod, M. Kollosche, R. Kornbluh, B. Lassen, M. Matysek, S. Michael, S. Nowak, B. O'Brien, Q. Pei, R. Peirine, B. Rechenbach, S. Rosset, H. Shea, *Smart Mater. Struct.* **2015**, *24*, 105025.
- [52] H. Yang, X. Yao, L. Yuan, L. Gong, Y. Liu, *Nanoscale* **2019**, *11*, 578.
- [53] D.Y. Cho, K. Eun, S.H. Choa, H.K. Kim, *Carbon N. Y.* **2014**, *66*, 530.
- [54] L. Liu, H. Chen, J. Sheng, J. Zhang, Y. Wang, S. Jia, *Smart Mater. Struct.* **2014**, *23*, 025037.
- [55] M. Wehner, B. Quinlivan, P.M. Aubin, E. Martinez-villalpando, L. Stirling, K. Holt, R. Wood, C. Walsh, *IEEE Int. Conf. Robot. Autom.* **2013**, 3347.
- [56] P. Polygerinos, Z. Wang, K.C. Galloway, R.J. Wood, C.J. Walsh, *Rob. Auton. Syst.* **2015**, *73*, 135.
- [57] Y. He, D. Wu, M. Zhou, Y. Zheng, T. Wang, C. Lu, L. Zhang, H. Liu, C. Liu,

- Appl. Mater. Interface* **2021**, *13*, 15572.
- [58] S. Ramasamy, A. Balan, *Sens. Rev.* **2018**, *38*, 412.
- [59] S.K. Banala, S.H. Kim, S.K. Agrawal, J.P. Scholz, *Proc. 2nd Bienn. IEEE/RAS-EMBS Int. Conf. Biomed. Robot. Biomechatronics, BioRob 2008* **2008**, *17*, 653.
- [60] A.B. Zoss, H. Kazerooni, A. Chu, *IEEE/ASME Trans. Mechatronics* **2006**, *11*, 128.
- [61] E. Roh, B.U. Hwang, D. Kim, B.Y. Kim, N.E. Lee, *ACS Nano* **2015**, *9*, 6252.
- [62] Z. Yang, Y. Pang, X.L. Han, Y. Yang, Y. Yang, J. Ling, M. Jian, Y. Zhang, T.L. Ren, *ACS Nano* **2018**, *12*, 9134.
- [63] A. Razei, A. Ejupi, M. Gholami, A. Ferrone, C. Menon, in *Int. Conf. Biomed. Robot. Biomechatronics*, **2018**, 563.
- [64] A.A.M. Faudzi, J. Ooga, T. Goto, M. Takeichi, K. Suzumori, *IEEE Robot. Autom. Lett.* **2018**, *3*, 92.
- [65] M.F. Mohamed, A.S.M. Hanif, A.A. Faudzi, *Int. J. Automot. Mech. Eng.* **2020**, *17*, 7533.
- [66] S.Z. Ying, N.K. Al-Shammari, A.A. Faudzi, Y. Sabzehmeidani, *Eng. Technol. Appl. Sci. Res.* **2020**, *10*, 5276.
- [67] M. Luo, L. Liu, C. Liu, B. Li, C. Cao, X. Gao, D. Li, *IEEE Trans. Ind. Electron.* **2021**, *68*, 8455.
- [68] J. Shintake, S. Rosset, B. Schubert, D. Floreano, H. Shea, *Adv. Mater.* **2016**, *28*, 231.
- [69] J. Guo, K. Elgeneidy, C. Xiang, N. Lohse, L. Justham, J. Rossiter, *Smart Mater. Struct.* **2018**, *27*, 2019.
- [70] Y. Okuno, H. Shigemune, Y. Kuwajima, S. Maeda, *Adv. Mater. Technol.* **2019**, *4*, 1.
- [71] B.N.J. Persson, J. Guo, *Soft Matter* **2019**, *15*, 8032.
- [72] H. Shigemune, K. Pradidarcheep, Y. Kuwajima, Y. Seki, S. Maeda, V. Cacucciolo, *Adv. Intell. Syst.* **2021**, *2100004*, 2100004.
- [73] Z. Mao, T. Iizuka, S. Maeda, *Sensors Actuators A Phys.* **2021**, *332*, 113168.
- [74] J. Wang, S. Li, D. Gao, J. Xiong, P.S. Lee, *NPG Asia Mater.* **2019**, *11*.

- [75] K. Takagi, Y. Kitazaki, K. Kondo, *Actuators* **2021**, 10.
- [76] T. Hiruta, N. Hosoya, S. Maeda, I. Kajiwara, *Sensors Actuators A. Phys.* **2021**, 330, 112830.
- [77] I. Kajiwara, S. Kitabatake, N. Hosoya, S. Maeda, *Int. J. Mech. Sci.* **2019**, 157–158, 849.
- [78] P. Zhao, Y. Cai, C. Liu, D. Ge, B. Li, H. Chen, *Opt. Mater. (Amst)*. **2021**, 111.
- [79] W. Thongking, A. Wiranata, A. Minaminosono, Z. Mao, S. Maeda, *J. Robot. Mechatronics* **2021**, 33, 968.
- [80] J. Huang, T. Li, C.C. Foo, J. Zhu, D.R. Clarke, J. Huang, T. Li, C.C. Foo, J. Zhu, D.R. Clarke, *Appl. Phys. Lett.* **2012**, 100, 0441911.
- [81] N. Besse, S. Rosset, J.J. Zarate, H. Shea, *Adv. Mater. Technol.* **2017**, 2, 1.
- [82] C. Zeng, L. Liu, W. Bian, Y. Liu, J. Leng, *Compos. Part B Eng.* **2020**, 194, 108034.
- [83] G. Scalet, *Actuators* **2020**, 9, 1.
- [84] W. Miao, W. Zou, B. Jin, C. Ni, N. Zheng, Q. Zhao, T. Xie, *Nat. Commun.* **2020**, 11, 1.
- [85] H. Li, J. Yao, P. Zhou, X. Chen, Y. Xu, Y. Zhao, *Sensors Actuators, A Phys.* **2020**, 306, 111957.
- [86] Z. Mao, G. Shimamoto, S. Maeda, *Colloids Surfaces A Physicochem. Eng. Asp.* **2020**, 125561.
- [87] S. Maeda, Y. Hara, R. Yoshida, S. Hashimoto, *Int. J. Mol. Sci.* **2010**, 11, 52.
- [88] T. Hwang, Z. Frank, J. Neubauer, K.J. Kim, *Sci. Rep.* **2019**, 9, 2.
- [89] Z. Mao, M. Kuroki, Y. Otsuka, S. Maeda, *Extrem. Mech. Lett.* **2020**, 39, 100830.
- [90] S. Maeda, Y. Hara, T. Sakai, R. Yoshida, S. Hashimoto, *Adv. Mater.* **2007**, 19, 3480.
- [91] X. Zhang, X. Xu, L. Chen, C. Zhang, L. Liao, *Dye. Pigment.* **2020**, 174, 108042.
- [92] S.T. Han, H. Peng, Q. Sun, S. Venkatesh, K.S. Chung, S.C. Lau, Y. Zhou, V.A.L. Roy, *Adv. Mater.* **2017**, 29, 1.
- [93] A.A. Barlian, W.T. Park, J.R. Mallon, A.J. Rastegar, B.L. Pruitt, *Proc. IEEE*

2009, 97, 513.

- [94] B. Camburn, K. Wood, *Des. Stud.* **2018**, 58, 63.
- [95] V. Rognoli, C.A. Garcia, S. Parisi, *Mak. Futur. J.* **2016**, 4, 1.
- [96] M. Wolf, S. Mcquitty, *Acad. Mark. Sci. Rev.* **2011**, 1, 154.
- [97] B.G. Wong, C.P. Mancuso, S. Kiriakov, C.J. Bashor, A.S. Khalil, *Nat. Biotechnol.* **2018**, 36, 614.
- [98] K.P. Szymula, M.S. Magaraci, M. Patterson, A. Clark, S.G. Mannickarottu, B.Y. Chow, *Biochemistry* **2019**, 58, 468.
- [99] W. Vallejo, C. Diaz-Uribe, C. Fajardo, *Heliyon* **2020**, 6, e03591.
- [100] J.P. Grinias, J.T. Whitfield, E.D. Guetschow, R.T. Kennedy, *J. Chem. Educ.* **2016**, 93, 1316.
- [101] Š. Kubínová, J. Šlégr, *J. Chem. Educ.* **2015**, 92, 1751.
- [102] T. Murakami, Y. Kuwajima, A. Wiranata, A. Minaminosono, H. Shigemune, Z. Mao, S. Maeda, *Micromachines* **2021**, 12, 1.
- [103] A. Wiranata, S. Maeda, *Key Eng. Mater.* **2021**, 884, 430.
- [104] T. Murakami, A. Minaminosono, A. Wianata, H. Okabe, H. Shigemune, in *IEEE 4th Int. Conf. Soft Robot.*, IEEE**2021**, 5.
- [105] Y. Yamamoto, D. Yamamoto, M. Takada, H. Naito, T. Arie, S. Akita, K. Takei, *Adv. Healthc. Mater.* **2017**, 6, 1.
- [106] S.H. Jeong, S. Zhang, K. Hjort, J. Hilborn, Z.G. Wu, *Adv. Mater.* **2016**, 28, 5830.
- [107] M. Han, J. Lee, J.K. Kim, H.K. An, S.W. Kang, D. Jung, *Sensors Actuators, A Phys.* **2020**, 305, 111941.
- [108] A. Tonazzini, J. Shintake, C. Rognon, V. Ramachandran, S. Mintchev, D. Floreano, *2018 IEEE Int. Conf. Soft Robot. RoboSoft 2018* **2018**, 485.
- [109] X. Qu, S. Wang, Y. Zhao, H. Huang, Q. Wang, J. Shao, W. Wang, X. Dong, *Chem. Eng. J.* **2021**, 425, 131523.
- [110] D.P. Allen, R. Little, J. Laube, J. Warren, W. Voit, R.D. Gregg, *Mechatronics* **2021**, 76, 102551.
- [111] M. Chakraborty, M.S.J. Hashmi, M. Ramadan, *Ref. Modul. Mater. Sci. Mater. Eng.* **2021**, 1.

- [112] Z. Liu, Z. Li, H. Zhai, L. Jin, K. Chen, Y. Yi, Y. Gao, L. Xu, Y. Zheng, S. Yao, Z. Liu, G. Li, Q. Song, P. Yue, S. Xie, Y. Li, Z. Zheng, *Chem. Eng. J.* **2021**, *426*, 130869.
- [113] J.N. Kim, J. Lee, H. Lee, I.K. Oh, *Nano Energy* **2021**, *82*, 105705.
- [114] D.M. Opris, M. Molberg, C. Walder, Y.S. Ko, B. Fischer, F.A. Nüesch, *Adv. Funct. Mater.* **2011**, *21*, 3531.
- [115] W. Wu, *Sci. Technol. Adv. Mater.* **2019**, *20*, 187.
- [116] D.Y. Choi, M.H. Kim, Y.S. Oh, S.H. Jung, J.H. Jung, H.J. Sung, H.W. Lee, H.M. Lee, *ACS Appl. Mater. Interfaces* **2017**, *9*, 1770.
- [117] A. Wiranata, Y. Ohsugi, A. Minaminosono, Y. Kuwajima, S. Maeda, *HardwareX* **2022**, *11*, e00287.
- [118] H. Kurata, A. Wiranata, S. Maeda, N. Hosoya, in *Proc. Dyn. Des. Conf.*, **2021**, 366.
- [119] J.P.L. Bigué, J.S. Plante, *IEEE/ASME Trans. Mechatronics* **2013**, *18*, 169.
- [120] Z. Ren, S. Kim, X. Ji, W. Zhu, F. Niroui, J. Kong, Y. Chen, N. Farnaz, J. Kong, Y. Chen, *Adv. Mater.* **2021**, *34*, 2106757.
- [121] Y. Chen, H. Zhao, J. Mao, P. Chirarattananon, E.F. Helbling, N.P. Hyun, D.R. Clarke, R.J. Wood, *Nature* **2019**, *575*, 324.
- [122] J. Shintake, H. Shea, D. Floreano, *IEEE Int. Conf. Intell. Robot. Syst.* **2016**, *2016-Novem*, 4957.
- [123] J. Shintake, V. Cacucciolo, H. Shea, D. Floreano, *Soft Robot.* **2018**, *5*, 466.
- [124] H. Godaba, J. Li, Y. Wang, J. Zhu, *IEEE Robot. Autom. Lett.* **2016**, *1*, 624.
- [125] Y. Qiu, E. Zhang, R. Plamthottam, Q. Pei, *Acc. Chem. Res.* **2019**, *52*, 316.
- [126] A. Bruschi, D.M. Donati, P. Choong, E. Lucarelli, G. Wallace, *Adv. Healthc. Mater.* **2021**, *10*, 1.
- [127] M. Duduta, E. Hajiesmaili, H. Zhao, R.J. Wood, D.R. Clarke, *Proc. Natl. Acad. Sci.* **2019**, *116*, 2476.
- [128] I.A. Anderson, T.A. Gisby, T.G. McKay, B.M. O'Brien, E.P. Calius, *J. Appl. Phys.* **2012**, *112*.
- [129] J. Xu, Y. Dong, Z. Jiang, L. Tang, X. Chen, Z. Yao, K. Cao, *Compos. Part A Appl. Sci. Manuf.* **2021**, *149*, 106519.

- [130] U. Gupta, L. Qin, Y. Wang, H. Godaba, J. Zhu, *Smart Mater. Struct.* **2019**, *28*, 1.
- [131] Z. Wang, K. Yu, G. Xie, J. Zou, *IOP Conf. Ser. Earth Environ. Sci.* **2018**, *108*, 052094.
- [132] W.H. Butterfield, *Behav. Ther.* **1975**, *6*, 98.
- [133] L. Zhang, D.P. Rabussay, *Bioelectrochemistry* **2002**, *56*, 233.
- [134] I.D. Johnston, D.K. McCluskey, C.K.L. Tan, M.C. Tracey, *J. Micromechanics Microengineering* **2014**, *24*, 1.
- [135] D. Gatti, H. Haus, M. Matysek, B. Frohnapfel, C. Tropea, H.F. Schlaak, *Appl. Phys. Lett.* **2014**, *104*, 1.
- [136] A. Zucca, K. Yamagishi, T. Fujie, S. Takeoka, V. Mattoli, F. Greco, *J. Mater. Chem. C* **2015**, *3*, 6539.
- [137] K. Yamagishi, T. Nakanishi, S. Mihara, M. Azuma, S. Takeoka, K. Kanosue, T. Nagami, T. Fujie, *NPG Asia Mater.* **2019**, *11*, 1.
- [138] A. Wiranata, M. Kanno, N. Chiya, H. Okabe, T. Horii, T. Fujie, N. Hosoya, S. Maeda, *Appl. Phys. Express* **2021**, *15*, 011002.

List of Publications

[Journal]

1. **Ardi Wiranata**, Yunosuke Ohsugi, Ayato Minaminosono, Yu Kuwajima, Shingo Maeda, "Electromechanical Tensile Test Equipment for Stretchable Conductive Materials", HardwareX (Vol 11, Pages e00287-1- e00287-12, 2022)
2. Yu Kuwajima, Yumeta Seki, Yuhei Yamada, Satoshi Awaki, Shota Kamiyauchi, **Ardi Wiranata**, Yuto Okuno, Hiroki Shigemune, and Shingo Maeda, "Electrochemical Dual Transducer for Fluidic Self-Sensing Actuation", ACS Applied Materials and Interfaces (Vol 14, Pages 3496–3503, 2022)
3. Taichi Murakami, Yu Kuwajima, **Ardi Wiranata**, Ayato Minaminosono, Hiroki Shigemune, Zebing Mao and Shingo Maeda," A DIY Fabrication Approach for Ultra-Thin Focus-Tunable Liquid Lens Using Electrohydrodynamic Pump", Micromachines (Volume 12, Pages 1452, 2021).
4. **Ardi Wiranata**, Makoto Kanno, Naoki Chiya, Hozuma Okabe, Tatsuhiro Horii, Toshinori Fujie, Naoki Hosoya, and Shingo Maeda, "High-Frequency, low-voltage oscillations of dielectric elastomer actuators" Applied Physics Express (Volume 15, Pages 011002-1 - 011002-6, 2021).
5. **Ardi Wiranata**, Yunosuke Ohsugi, Ayato Minaminosono, Zebing Mao, Haruyuki Kurata, Naoki Hosoya and Shingo Maeda, "A DIY Fabrication Approach of Stretchable Sensors Using Carbon Nano Tube Powder for Wearable Device", Frontiers in Robotics and AI (Volumes 8, Pages 1-15,2021).
6. **Ardi Wiranata**, Ayato Minaminosono, Shingo Maeda, "Automatic Brushing Machine for Stretchable Electrodes", SEATUC journal of science and engineering (Volume 2 Pages 1-7, 2021).
7. Witchuda Thongking, **Ardi Wiranata**, Ayato Minaminosono, Zebing Mao, and Shingo Maeda, "Soft Robotic Gripper Based on Multi-Layers of

Dielectric Elastomer Actuators”, Journal of Robotics and Mechatronics (Vol.33, Pages. 968-974,2021).

8. **Ardi Wiranata**, Yasuyuki Ishii, Naoki Hosoya, Shingo Maeda, “Simple and Reliable Fabrication Method for Polydimethylsiloxane Dielectric Elastomer Actuators Using Carbon Nanotube Powder Electrodes”, Advanced Engineering Materials (Volumes 23, Pages 2001181 (1 of 11),2021).
9. **Ardi Wiranata**, Shingo Maeda, “Implementation of Sylgard 184 For Powder-Based Dielectric Elastomer Actuators”, SEATUC journal of science and engineering (Volume 1, Pages 14-19,2020).

[Refereed Paper of International conference]

1. **Ardi Wiranata**, Abdulsalam Mohammed Abdullah Haidar, Taichi Murakami, Ayato Minaminosono, Zebing Mao, Shingo Maeda, “Dynamic characteristics of a dielectric elastomer actuator fabricated using a stretchable CNT powder electrode”, 32nd 2021 International Symposium on Micro-NanoMechatronics and Human Science (From Micro & Nano Scale Systems to Robotics & Mechatronics Systems).
2. Taichi Murakami, Ayato Minaminosono, **Ardi Wiranata**, Hozuma Okabe, Hiroki Shigemune, Shingo Maeda, “Characteristic Evaluation of Dielectric Elastomer Actuator Based on The Stretchable Electrode Density”, 2021 IEEE 4th International Conference on Soft Robotics (RoboSoft).
3. **Ardi Wiranata**, Shingo Maeda, “A Deformable Linear Dielectric Elastomer Actuator”, Key Engineering Materials (Volume 884, Pages 430-436, 2021)

[Paper of Domestic conference]

1. Haruyuki Kurata, **Ardi Wiranata**, Shingo Maeda, and Naoki Hosoya, “フレキシブルセンサによる振動応答計測 Vibration response measurement via a flexible sensor”, 日本機械学会 Dynamics and Design Conference, 2021.

2. Ayato Minaminosono, Taichi Murakami, **Ardi Wiranata**, Yunosuke Ohsugi, Hiroki Shigemune, Shingo Maeda, “液体金属のソフトアクチュエータへの適用と性能評価 Application of liquid metal to soft actuators and its performance evaluation”, Robomech 2021.

[Presentation of international conference]

1. Taichi Murakami, **Ardi Wiranata**, Hiroki Shigemune and Shingo Maeda, “Failure Prediction in Dielectric Elastomer Actuators by Temperature Monitoring System”, Poster Presentation in the 16th South East Asian Technical University Consortium (SEATUC), 2022.
2. Taichi Murakami, Yu Kuwajima, **Ardi Wiranata**, Ayato Minaminosono, Hiroki Shigemune, Zebing Mao, Shingo Maeda, “Controllable liquid lenses driven by EHD pump”, 32nd 2021 International Symposium on Micro-NanoMechatronics and Human Science (From Micro & Nano Scale Systems to Robotics & Mechatronics Systems) (poster session)

[Presentation of Domestic conference]

1. Yunosuke Ohsugi, Ayato Minaminosono, **Ardi Wiranata**, Zebing Mao, Taichi Murakami, Shingo Maeda, “DEA モーターの制御を行うストレッチセンサの開発 Development of stretch sensors for controlling DEA motor”, Robomech 2021.

[Achievement]

1. Invited as a keynote lecture speaker at D&D 2022 (organized by JSME).
Lecture title: The Application of powdered-based electrodes fabricated using brushing methods for DEA and Des.